H24/3246

MONASH UNIVERSITY
THESIS ACCEPTED IN SATISFACTION OF THE
REQUIREMENTS FOR THE DEGREE OF
DOCTOR OF PHILOSOPHY
ON.....6 September 2002.....
.....[redacted].....
Sec, Research Graduate School Committee

PREDICTION OF THE PROCESSING WINDOW AND AUSTEMPERABILITY FOR AUSTEMPERED DUCTILE IRON

A thesis submitted in fulfilment of the requirements
for the degree of Doctor of Philosophy

Saden H. Zahiri

B.Eng. (Hons.), M.Eng. (Hons)

School of Physics and Materials Engineering
Monash University
Clayton, Victoria 3800
Australia

January 2002

ABSTRACT

The aim of this work was to predict the processing window and austemperability of austempered ductile iron (ADI). Austempering of ductile iron within the processing window (austempering window), which is a window of austempering time and austempering temperature, leads to fulfillment of the minimum requirements for mechanical properties of ADI defined by ASTM A897:1990 standard. Austemperability is the maximum section size that can be austempered without formation of pearlite in ADI matrix.

The processing window boundaries were estimated using a model for prediction of time for isothermal transformation of austenite to bainite in high Si steels and experimental data available from the literature. The predicted processing window boundaries were evaluated for a ductile iron of composition (wt. %) Fe-3.41C-2.46Si-0.36Mn-0.18Mo-0.25Cu-0.036Mg. The validation results showed that the model successfully estimates the austempering window for the iron of this study.

The predicted processing window was associated with some errors which were due to limitations in experimental techniques and experimental data available in the literature. However, the difference between the model and expected results were reasonably small, confirming that the model results were acceptable for the validation alloy of this study.

The austemperability was predicted according to the point at which the cooling curve within a large section size ductile iron test bar touches the tip of the pearlite curve of the TTT diagram. The cooling curve in a ductile iron test bar was predicted according to a model for conduction of heat in an infinite solid cylinder. The model for estimation of the austemperability was validated according to a ductile iron of composition (wt. %) Fe-3.63C-2.4Si-0.39Mn-0.24Mo-0.25Cu-0.04Ni-0.04Mg. The validation results were in good agreement with the estimated austemperability for ductile iron of this study.

A three-dimensional diagram of processing-austemperability window was introduced. The processing-austemperability window presents the austempering time and corresponding austempering temperature that lead to ADI to satisfy the ASTM standard A897M:1990 as well as the maximum section size of the material that can be successfully austempered without formation of pearlite in the matrix.

The processing-austemperability window was predicted for an iron of composition (wt. %) Fe-3.41C-2.46Si-0.36Mn-0.18Mo-0.25Cu-0.036Mg. Mechanical properties of the material were investigated within the predicted processing-austemperability window. The results showed that for the chosen austempering times the mechanical properties successfully satisfy the minimum requirements for ASTM A897:1990 without formation of pearlite in the matrix of the material.

DECLARATION

This thesis contains no material that has been accepted previously for the award of any other degree or diploma in any university or other institution. To the best of my knowledge and belief, it contains no material published previously or written by any other person, except where due reference is made in the text.

Saden H. Zahiri

[redacted]

January 2002

ACKNOWLEDGEMENTS

I would like to express my sincere appreciation to my thesis supervisor Dr. Elena Pereloma for her guidance, encouragement and support throughout the whole course of this study. I am also grateful to Dr. Chris Davies for his stimulating discussions and supervision during the course of this research work.

My sincere thanks are due to my mother, father and sister for their motivation and encouragement over the years. A special thanks to Shane Brunning, Sonia Barthelmebs and Nazanin Namdar for their support during the course of this study.

Last, but not least, I would like to gratefully acknowledge the Australian Research Council (ARC) and Mr. Ross Williams (Metal Treatment Services Ltd.) who provided financial support without which this work could not have been completed.

This thesis is dedicated to those whose lives have had a positive impact on others

TABLE OF CONTENTS

LIST OF SYMBOLS AND ABBREVIATIONS

$\bar{L}$	Mean linear intercept
β	Autocatalysis factor
θ	Maximum volume fraction of bainitic ferrite (at the T_o line)
ξ	Normalised volume fraction of bainitic (ausferritic) ferrite (v/θ)
v	Actual volume fraction of bainitic ferrite
$\bar{x}$	Mole fraction of carbon in the matrix
α	Thermal diffusivity (m^2s^{-1})
ρ	Density ($kg.m^{-3}$)
λ_1, λ_2	Empirical constants
ΔG°_m	Initial value of maximum possible free energy change on nucleation ($J.mol^{-1}$)
α_M	Volume fraction of martensite
AF	Ausferritic ferrite
B	Contact coefficient
BF	Bainitic ferrite
C_γ	Austenite percentage
C_α	Ausferritic ferrite percentage
c_p	Specific heat of the material ($m^2.s^{-2}.K$)
D_k	Critical diameter of ductile iron (maximum diameter that can be successfully austempered without formation of pearlite in the ductile iron microstructure) (mm)
F	Volume fraction of ADI matrix without graphite nodules
G_A	Prior austenite grain size (μm)
G_N	Universal nucleation function
HCA	High carbon austenite
I_γ	Integrated intensity per unit length of diffraction line ($J.s^{-1}.m^{-1}$) for austenite
I_α	Integrated intensity per unit length of diffraction line ($J.s^{-1}.m^{-1}$) for (ausferritic) ferrite

K_1	Function of austenite grain size
K_2	Empirical constant
k_t	Thermal conductivity ($W.m^{-1}.K^{-1}$)
LCA	Low carbon austenite
N	Constant (=60)
R	Constant (=2540 $J.mol^{-1}$)
R	Gas constant
R_γ	Constant (depends on the crystal structure and lattice parameter of austenite)
R_α	Constant (depends on the crystal structure and lattice parameter of ferrite)
R_c	Radius of an infinite solid cylinder (mm)
R_{cmax}	Austemperability (hardenability) of ADI (mm)
T	Time (s)
T	Temperature (°C)
T_γ	Austenitising temperature (°C)
t_1	Austempering time for the beginning of the processing window (s)
t_2	Austempering time for the end of the processing window (s)
T_A	Austempering temperature (°C)
T_f	Test bar final temperature (°C)
T_i	Test bar initial temperature (°C)
T_o	Line representing carbon concentrations above which the austenite to ferrite reaction cannot take place without diffusion
T_p	Temperature corresponding to the tip of pearlite curve (°C)
t_p	Time corresponding to tip of the pearlite curve (s)
U	Volume of bainite sub-unit (m^3)
URA	Un-reacted austenite
V_{HCA}	Volume fraction of high carbon austenite
ξ_α	Equilibrium mole fraction of carbon in ferrite
ξ_α	Equilibrium mole fraction of carbon in ferrite
x_c	Distance from surface of an infinite solid cylinder
X_C	Carbon concentration in austenite at T_γ

X_{To} Mole fraction of carbon at T_o

CHAPTER 1

Introduction

Austempered ductile iron (ADI) is a development of the metallurgy of ductile cast iron with excellent properties and cost competitiveness, better than those obtained with more common cast irons, forged steels and weldments (Keough, 1995; Chatterley & Murrell, 1998). ADI wear resistance, strength, damping and machinability are greater than competitive products (Keogh, 1995; Ductile Iron Society, 1999). A high strength to weight ratio makes the material a suitable substitute for aluminium products (Hayrynen, 1995; Keough, 1995). For instance, a truck hub made from ADI permits considerable weight reduction compared to aluminium (Hayrynen, 1995; Keough, 1995).

These explicit properties are due to the microstructure of ADI produced by austempering heat treatment of ductile cast iron. Austempering is a three-stage heat treatment process (Rouns & Rundman, 1987). At the first stage,

'austenitising', ductile iron is heated and held at a temperature range of 850-950°C for 1-2 hours to achieve a fully austenitic matrix. This is followed by the second stage, which is rapid quenching to the 'austempering' temperature. The final stage is an isothermal hold (austempering) in the temperature range 250-400°C followed by cooling to room temperature.

ADI microstructure consists of spheroidal graphite embedded in a matrix that is in general a mixture of ausferrite, martensite and carbide (Elliott, 1997). Ausferrite is a combination of high carbon austenite and carbide free acicular (plate like) ferrite (Kovacs, 1994). Microstructural engineering of ADI involves the correct proportion of the microstructural constituents that result in superior mechanical properties for the material. For instance, it is important to maximise the amount of ausferrite in the matrix to achieve high strength and high ductility for ADI. The as-cast microstructure, alloy composition and austempering process variables such as time and temperature have direct influence on the proportions of phases present in ADI matrix (Rouns & Rundman, 1987).

The know-how of ADI microstructural design has been the subject of many research works and is very well known (Elliott, 1997; Trudel & Gagne; 1997; Rouns & Rundman; 1987). For instance, processing window and austemperability are defined to set the limits for undesired microstructural constituents such as martensite, carbide and pearlite in ADI matrix.

Processing window is a window of time and temperature in which ADI satisfies the minimum requirements for mechanical properties defined by ASTM A897M:1990 standard (Elliott, 1997). The processing window consists of two boundaries. At the lower boundary of the processing window a maximum of 3% martensite is present in the ADI matrix (Elliott, 1997). The upper boundary of the processing window is associated with the time at which the maximum value for high carbon austenite in ADI matrix decreases by 10% (Elliott, 1997).

Austemperability of the ADI is the ability of the material to permit quenching to austempering temperature without formation of pearlite (Voigt, Lee & Tu, 1991). Pearlite generally forms in ADI of large section size due to slow cooling rate from austenitising to austempering temperature and is detrimental for mechanical properties of the material.

Austempering time, austempering temperature and section size for ADI must be selected carefully to achieve minimum requirements for mechanical properties defined by ASTM A897M:1990 standard. This is time consuming and involved with considerable amount of experimental work. For this reason, there have been attempts to develop models for the processing window (Yescas, Bhadeshia & Mackay, 2001) and austemperability for ADI (Dorazil et al., 1989).

Yescas, Bhadeshia and Mackay (2001) developed a neural network model that estimates the processing window boundaries using the volume

fraction of HCA. However, this model outcome shows a large discrepancy and has not been evaluated with experimental observations. Dorazil et al. (1989) developed an empirical model that takes alloying elements (Cu, Ni, Mn and Mo) and austempering temperature for prediction of the austemperability. However, the model does not take into account Si content and austenitising temperature for prediction of the austemperability, whereas, the Si content and austenitising temperature are known to change austenite carbon content and, therefore, the stability of austenite (Lee & Voigt, 1989).

The aim of this study is to estimate the processing window and austemperability of ADI for industrial applications. To achieve the aim, a model for the processing window is presented using a combination of numerical and kinetic models. In this model, the austempering time is estimated using a model for prediction of the time for isothermal transformation of austenite in high Si (>1.5%) steels and experimental data (for processing window) available from literature. Austemperability of ADI is estimated utilising a model for prediction of the cooling curve in a solid cylinder of ductile iron and predicted curve of the TTT diagram.

An outline of the numerical and experimental work done to test the above hypothesis is presented below.

Chapter 2 contains a review of the literature relevant to this study. Austempering process and microstructure of the ADI are explained. After demonstrating the effect of alloy composition and processing variables on the

microstructure of ADI, the processing window and the models developed for prediction of the volume fraction of ADI microstructural constituents are described. Finally the austemperability and the models for estimation of the maximum section size of ADI for a successful austempering heat treatment are outlined.

Chapter 3 focuses on experimental materials and methods. Optical microscopy, image processing and X-ray diffractometry were used to characterise the microstructural variations in ADI matrix. Tensile and impact tests were conducted on the specimens to establish basic mechanical properties. An experimental set up was used for simulation of the quenching curves from austenitising to austempering temperature.

Chapter 4 describes the models for estimation of the processing window boundaries and austemperability of ADI.

Chapter 5 deals with evaluation of the models for processing window and austemperability. The predicted models were examined utilising microstructural investigations. In this chapter, the processing-austemperability window corresponding to the ductile iron of this study is predicted and mechanical properties of the material are compared with the minimum requirements defined by ASTM A897M:1990 standard.

Chapter 6 discusses on the results associated with processing window and austemperability. The difference between the predicted and experimental results is investigated in this chapter.

Chapter 7 contains conclusions and recommendations for future work.

CHAPTER 2

Literature Review

2.1 Scope of literature review

The general aspects of processing-microstructure-relationships, processing window and austemperability of ADI are reviewed in the following sections. Section 2.2 describes the austempering process and microstructural changes during the austempering heat treatment. Section 2.3 outlines the effect of alloying elements, heat treatment parameters (such as temperature and time) on microstructure and mechanical properties of the material. Section 2.4 describes the concept of processing (austempering) window and the effect of heat treatment parameters and alloying elements on processing window. A background on the models developed for prediction of the time for isothermal transformation, processing window and segregation in ADI are provided in

section 2.5. In section 2.6 the effect of alloying elements and processing parameters on austemperability of ADI are reviewed. The models developed for prediction of the austemperability are addressed in this section. In the final section (2.7) a summary of the literature review and the purpose of this work is outlined.

2.2 Austempered ductile iron

Heat treatment of ductile iron castings produces a significant difference in mechanical properties from as-cast ductile iron (Davis, 1996; Blackmore & Harding, 1984). The common heat treatment processes applied to ductile iron are stress relieving, annealing, austempering, normalising, quenching and tempering. Among these heat treatments, austempering produces a combination of strength and ductility superior to other heat treatments of the iron (Davis, 1996) (Figure 2.1).

Austempered ductile iron (ADI) is a material with an excellent combination of strength, fracture toughness, wear resistance and damping capacity (Keough, 1995; Ahlstrand, 1997; Yamakawa et al., 1997). These properties make ADI suitable for a wide variety of applications in automotive, truck, agricultural, industrial, railroad, construction and military components (Keough, 1995). ADI has an excellent economic competitiveness with steels due to less energy consumption per unit weight to produce, approximately 90% of ductile iron is recycled, lower density (10-15% lighter than steels),

manufacturing flexibility of cast product and damping capacity (Keough, 1995; Bahmani, Elliott & Varahram, 1997; Nallicheri, Clark & Field, 1991).

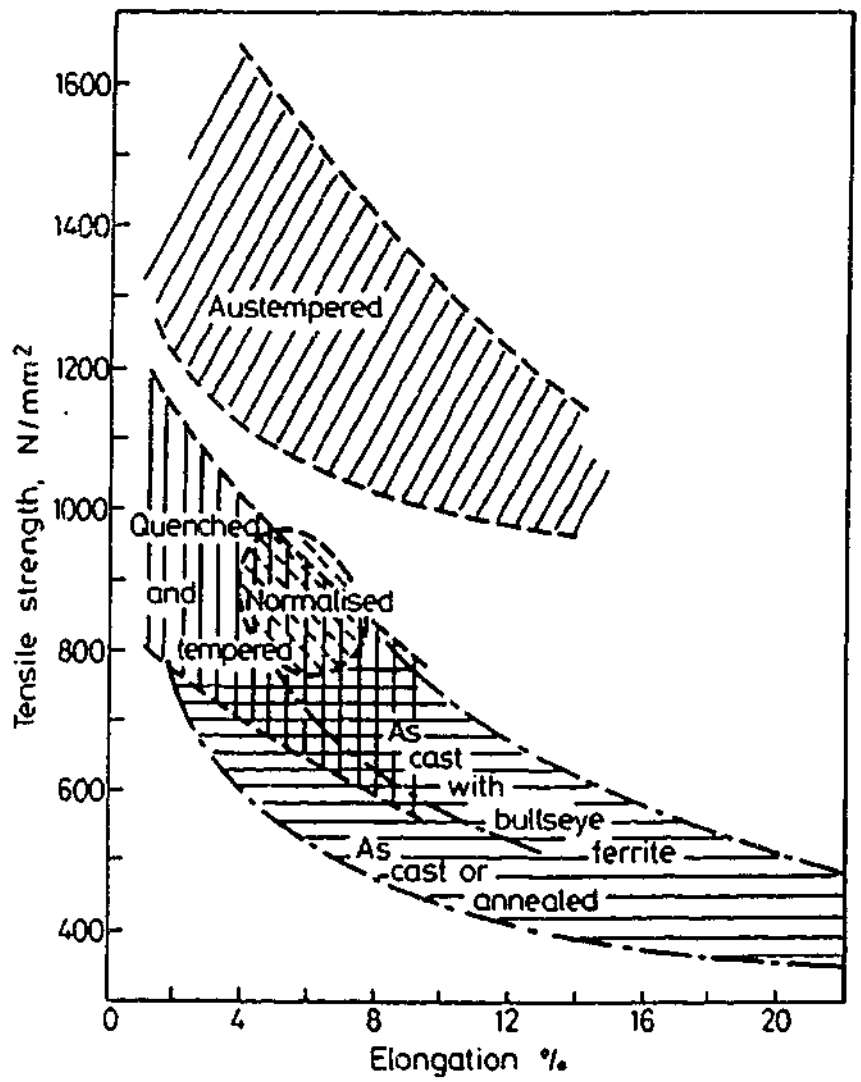

Figure 2.1 Strength and ductility of ductile irons achieved as-cast and by heat treatment (Blackmore & Harding, 1984)

A high strength to weight ratio and lower cost of production corresponding to ADI makes the material attractive to be a substitute for aluminium (Hayrynen, 1995; Keough, 1995). Commercial and environmental advantages of ADI benefit several industries, such as foundry, automotive, manufacturing, etc. (Keough, 1995; Ahlstrand, 1997; Yamakawa et al., 1997).

2.2.1 Ductile iron

Ductile iron is a type of cast iron possessing superior strength and impact resistance, in which spherodisation of graphite is produced by treating the molten metal with magnesium (Mg) or Cerium (Ce) (Tottle, 1984; Callister, 1991). The common names for this material are spheroidal graphite (SG) cast iron, ductile cast iron and nodular iron (Callister, 1991).

As-cast microstructures of ductile iron usually consist of ferrite, pearlite or both constituents depending on section size and alloy composition. It is well known that ductile iron possesses a heavily segregated microstructure that is due to the solidification process (Rouns & Rundman, 1987). During the solidification of ductile iron carbide forming elements such as Mn and Mo concentrate in the intercellular boundaries while graphitising elements such as Si, Cu and Ni segregate in eutectic cells (Rouns & Rundman, 1987) (Figure 2.2). In this study we are mostly involved with as-cast pearlitic ductile iron (bull's eye) in which graphite nodules are surrounded by ferrite in a pearlitic matrix (Figure 2.3).

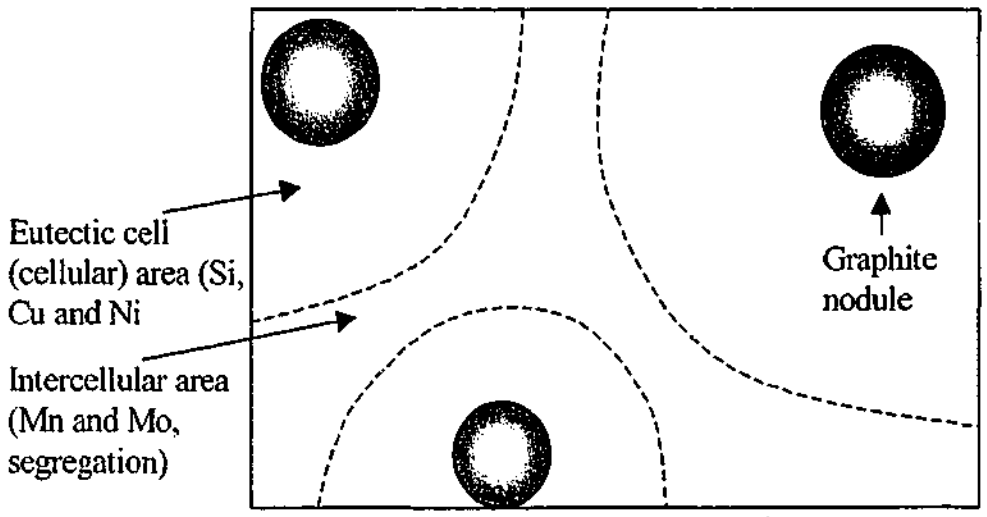

Figure 2.2 Schematic presentation of the alloying elements segregation in ductile iron matrix (Rouns & Rundman, 1987)

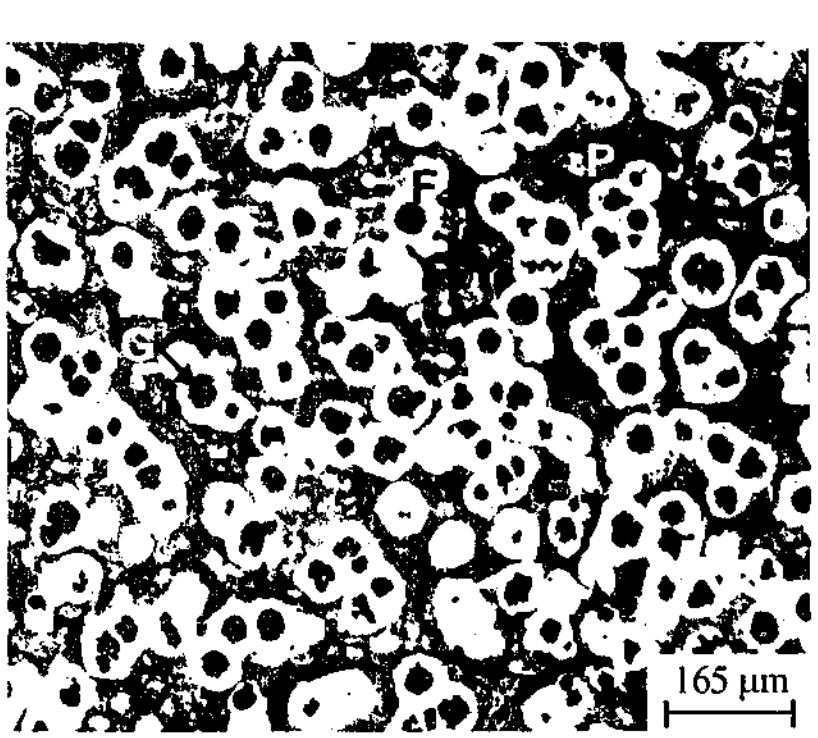

Figure 2.3 Micrograph of pearlitic (bull's eye) ductile cast iron: (G) graphite, (F) ferrite and (P) pearlite (etchant: Nital 2%)

2.2.2 Austempering heat treatment

Austempering heat treatment changes the as-cast microstructure of ductile iron (Figure 2.3) to a matrix of ausferrite and graphite nodules (Figure 2.4). Ausferrite is a mixture of acicular ferrite and (high carbon) austenite (Elliott, 1997).

A conventional austempering heat treatment is a three-stage process. At the first stage, 'austenitising', ductile iron is heated and held at a temperature range of 850-950°C (A-B-C in Figure 2.5) for 1-2 hours to achieve a fully austenitic microstructure saturated with carbon (0.6-1.1%C) (Elliott, 1997). This is followed by second stage (C-D) that is quenching fast enough from the austenitising temperature to austempering temperature to avoid austenite transformation to pearlite. The third step is austempering (D-G) in the temperature range of 250-400°C, followed by cooling to room temperature (G-H) (Elliott, 1997). Other austempering heat treatment processes such as step austempering (Bayati, Elliott & Lomier, 1995) are not discussed in this study.

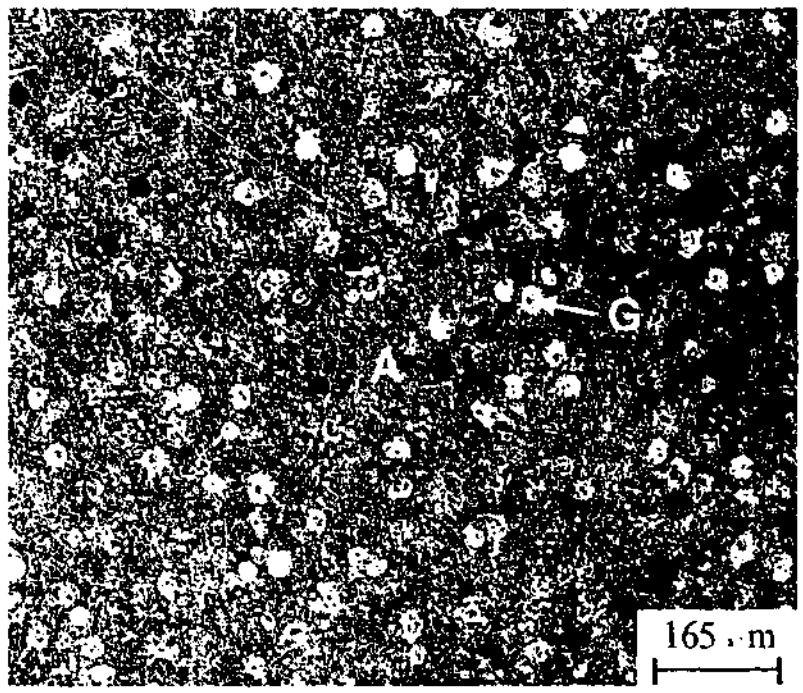

Figure 2.4 Micrograph of austempered ductile iron: (G) graphite nodule and (A) ausferrite (etchant: Nital 2%)

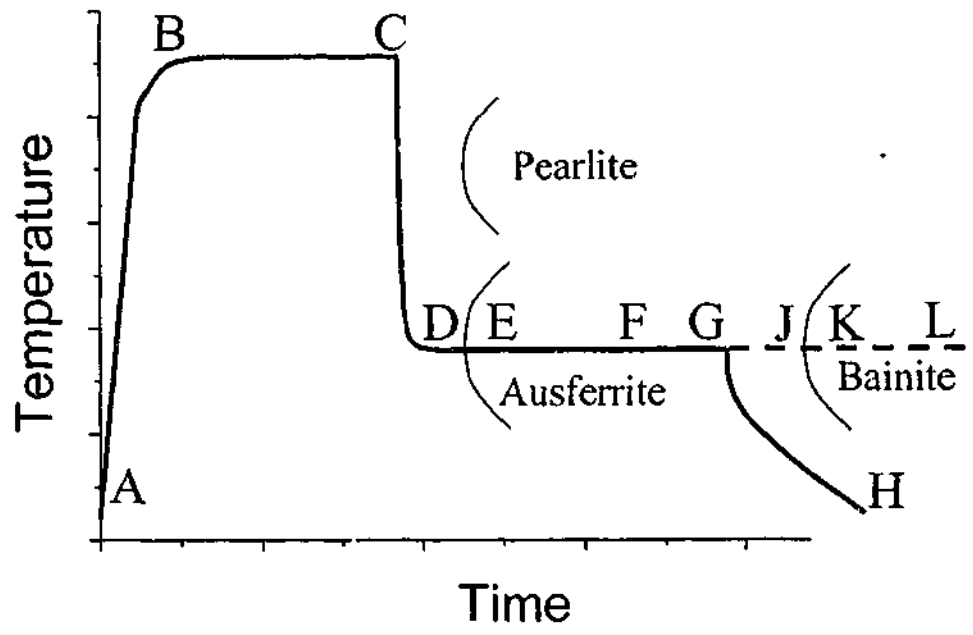

Figure 2.5 Schematic diagram of the austempering heat treatment

2.2.3 Austempering reactions

The first transformation in the austempering reaction (stage I reaction) (D-J in Figure 2.5) is the formation of acicular (ausferritic) ferrite from a fully austenitic matrix after a short period of time (D-E). There are still debates as to whether ferrite formation in ADI (similar to steels) involves a conventional nucleation and growth process or a diffusionless transformation (Bhadeshia & Edmonds, 1980; Hehmann, Kinsman & Aaronson, 1970).

This conflict arises in the choice between the reconstructive and displacive modes of solid state transformation. Hehmann, Kinsman and Aaronson (1970) suggest that growth of ferrite from the parent austenite follows a diffusion controlled growth (reconstructive) mechanism. On the other hand, Bhadeshia and Edmonds (1980) claim that bainitic (acicular) ferrite grows by the propagation of discrete martensitic sub-units (displacive mechanism). However, in both theories, carbon diffuses to the neighbouring austenite during isothermal transformation due to lower solubility of carbon in ferrite (equilibrium maximum 0.02% and paraequilibrium maximum 1.2%C) compared to austenite (maximum 2.2%C) (Bhadeshia, 1992).

Extension of the isothermal transformation time leads to an increase in carbon concentration of austenite. In the time period E-F the austenite carbon level increases to 1.2-1.7%. This (reacted) austenite may exist at room temperature. However, it is not fully saturated with carbon and is metastable.

For instance, below room temperature or under stress an austenite with 1.2-1.6% carbon content may transform to martensite and cause problems with machining, dimensional change and loss of ductility (Elliott, 1997).

Further extension of austempering time (F-G in Figure 2.5) leads to an increase in ausferritic ferrite volume fraction and enrichment of residual austenite (Elliott, 1997). During this time period carbon content of austenite reaches 1.8-2.2% making this phase both chemically and mechanically stable at room temperature (Elliott, 1997). For this reason an austenite with a high amount of carbon (1.8-2.2%) is called reacted stable austenite and is desirable in the ausferritic microstructure of high ductility ADI.

Referring to the above explanation, at the stage I austempering reaction austenite transforms to ausferritic ferrite (AF) and high carbon austenite (HCA) which includes reacted stable austenite with 1.8-2.2%C and un-reacted metastable austenite with 1.2-1.7% C (Equation 2.1).

Stage I reaction: $$\text{Austenite} \rightarrow \text{AF} + \text{HCA} \qquad (2.1)$$

Stage II austempering reaction occurs with further increase in austempering time (J-K-L). At this stage, high carbon austenite with 1.8-2.2% carbon content transforms to (bainitic) ferrite and carbide (Equation 2.2) (Elliott, 1997). This transformation is detrimental for ADI mechanical properties due to formation of carbides in the microstructure and a decrease in volume fraction of HCA.

Stage II reaction: HCA → (Bainitic) Ferrite + Carbide (2.2)

Different terminologies have been applied in regards to the state of austenite and ferrite in the literature corresponding to ADI microstructure. For example, some authors apply the term (carbide free) bainitic ferrite (BF) to the state of ferrite in ADI (Yescas, Bhadeshia & Mackay, 2001; James & Thomson, 1998). This is due to the fact that, similar to high Si steels (>1.5%), austenite transforms to carbide free (bainitic) ferrite because the high Si content of ADI (>2%) suppresses formation of carbide in ferrite phase.

Other researchers (Kovacs, 1994; Elliott, 1997) follow a more unified definition for ADI microstructural constituents. In this definition, ferrite in ADI microstructure is referred to either as acicular ferrite or bainitic ferrite. Acicular ferrite is a product of the stage I reaction and bainitic ferrite is a product of the stage II reaction (Kovacs, 1994; Elliott, 1997). The names suggested for the three types of austenite of different carbon content in ADI are (i) un-reacted (metastable) austenite with less than 1.2% carbon, (ii) reacted metastable austenite with carbon content between 1.2%-1.7%, and (iii) reacted stable austenite with carbon content between 1.8%-2.2%, (Kovacs, 1994).

Some of terminologies used above are cause for debate and in our work we do not intend to argue on them. We consider the most important microstructural constituents for our study as: (i) ausferrite which is a mixture

of HCA and ausferritic ferrite, (ii) ausferritic (acicular) ferrite (AF) which is a ferrite phase saturated with carbon similar to carbide free bainitic ferrite in high Si steels (Bhadeshia, 1992), (iii) high carbon austenite (HCA) with a carbon content of 1.2-2.2%, and (iv) un-reacted austenite (URA) which contains less than 1.2% carbon and transforms to martensite at room temperature. The HCA which is retained at room temperature (retained austenite) is a mixture of reacted stabilised austenite (1.8-2.2%C) and reacted metastable austenite (1.2-1.7%C). A summary of abbreviations for microstructural constituents is provided in the list of symbols.

2.2.4 Austemperability

A slow cooling rate from the austenitising to austempering temperature normally occurs in a thick section size ductile iron that results in transformation of austenite to high temperature products such as pearlite (Voigt & Loper, 1984), an example of which is shown in Figure 2.6. Pearlite is detrimental for mechanical properties of ADI and is not desired in the matrix (Bahmani & Elliott, 1994). 'Austemperability' of ductile iron is the capability of ADI to permit quenching to austempering temperature without formation of pearlite (Voigt, Lee & Tu, 1991).

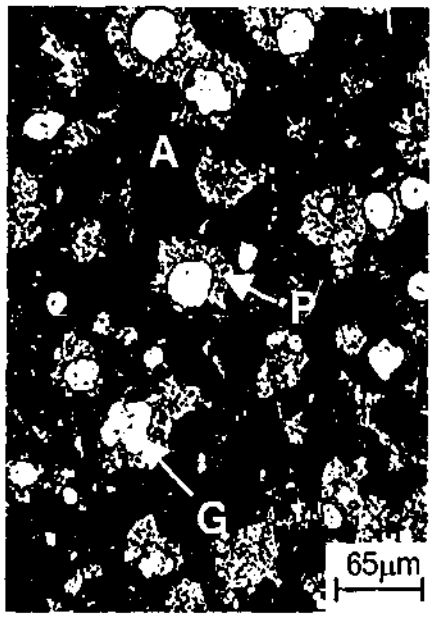

Figure 2.6 Micrograph corresponding to formation of pearlite in ADI microstructure due to slow cooling rate of 8°C/s: (A) ausferrite, (P) fine pearlite and (G) graphite

In general the addition of alloying elements (more than the minimum levels necessary to control austempering kinetics), an increase in austenitising temperature and quench severity of quenching media (H) improves austemperability (Voigt, Lee & Tu, 1991; Voigt & Loper, 1984; Kazerooni, Nazarboland & Elliott, 1997).

However, most of the austemperability measurements for ADI are based on hardenability of ductile iron measured either by Jominy test or continuous cooling of alloyed and unalloyed ductile irons to room temperature (Voigt, Lee & Tu, 1991; Lee & Voigt, 1989; Dorazil et al., 1986, 1989). This is due to the similarity of the concepts of austemperability and hardenability. Hardenability refers to the ability to cool a ferrous material rapidly enough to

form martensite and thereby avoid transformation above the M_s (martensite start) temperature to pearlite and/or bainite (Voigt, Lee & Tu, 1991). However, austemperability only refers to the ability to miss the pearlite nose of the CCT curve and subsequently transform at the bainite transformation temperature (Voigt & Loper, 1984).

2.3 Processing-microstructure-mechanical property relationships

Several specifications are being formulated for mechanical properties of ADI. However, the most stringent and most used is the ASTM A897:1990 standard in which minimum values for mechanical properties correspond to different grades of ADI (Table 2.1). Grades of ADI are established to categorise the material for different applications. For instance, grades 1 and 2 (low grades) are useful for high ductility and high toughness while grades 4 and 5 (high grades) are beneficial for high strength and high wear resistance applications (Table 2.1).

The minimum values for the ASTM standard corresponding to each grade of ADI will be satisfied if a correct proportion of microstructural constituents (such as AF, HCA and martensite) is achieved. The amounts of the microstructural constituents are dependent on the alloying elements, austempering process variables such as austenitising time, austenitising temperature, austempering time and austempering temperature (Rouns & Rundman, 1987).

Grade	Tensile Strength (MPa)	Yield Strength (MPa)	Elongation (%)	Impact Energy (Joules)	Typical Hardness (BHN)
1	850	550	10	100	269-321
2	1050	700	7	80	302-363
3	1200	850	4	60	341-444
4	1400	1100	1	35	388-477
5	1600	1300	N/A	N/A	444-555

Table 2.1 Hardness, toughness and tensile properties at room temperature for austempered ductile iron grades specified in ASTM A 897 M (Davis, 1996)

2.3.1 Effect of austenitising

Austenitising treatment requires sufficient time and temperature to produce a carbon-saturated austenite with 1.1-1.3%C (Trudel & Gagne, 1997; Rouns & Rundman, 1987). It has been suggested that two hours austenitising is needed to achieve a fully austenitic microstructure (Rouns & Rundman, 1987). An extension in austenitising time leads to an increase in austenite carbon content (that is sourced from graphite nodules) and a longer time for isothermal transformation of austenite to ausferrite (stage I reaction) (Bayati & Elliott, 2000).

Austenitising temperature is normally between 850-950°C. Decreasing the austenitising temperature reduces the carbon content of austenite which increases the driving force for stage I reaction and consequently reduces the time for isothermal transformation (Bayati & Elliott, 1995; Nazarbonland &

Elliott, 1997). However, low carbon austenite decreases austemperability of ADI (Bayati & Elliott, 1995; Trudel & Gagne, 1997).

An increase in austenitising temperature leads to insertion of more carbon from graphite nodules to the surrounding matrix. This has two effects, (i) increasing the volume fraction of HCA which is necessary for high ductility ADI and (ii) extension of the time for transformation of austenite to ausferrite (stage I reaction) (Bayati & Elliott, 1995).

2.3.2 Effect of austempering

In order to achieve the optimum mechanical properties for a particular ADI composition, we need to obtain the maximum volume fraction of ausferrite in the matrix. Austempering temperature and time are the most important processing variables that control the volume fraction of ausferrite and other microstructural constituents such as martensite and carbide.

2.3.2.1 Austempering temperature

The grade of ADI (Table 2.1) mainly depends on austempering temperature; the higher the temperature, the lower the grade of ADI (Elliott, 1997). This is because of a change in morphology of ausferritic ferrite and volume fraction of microstructural constituents with austempering temperature.

At low austempering temperatures (250-300°C) the morphology of the ausferritic ferrite has a fine (needle-like) microstructure with HCA of carbon concentration about 1.8-2.2%, similar to steels with lower bainite microstructure (Darwish & Elliott, 1993; Yazdani & Elliott, 1999a). The fine structure of the ausferritic ferrite at low austempering temperature is associated with a large under-cooling of the austenite and a slow diffusion rate of carbon in austenite that results in further nucleation of ferrite plates rather than their growth.

Morphology of austenite/ausferritic ferrite (carbide free bainitic ferrite) at low austempering temperatures strongly affects the mechanical properties of the ADI. A short distance between the fine ausferritic (bainitic) ferrite platelets at low austempering temperatures cuts the network of retained austenite that is essential to prevent crack propagation in the matrix and therefore, decreases the ductility and toughness of the material (Yan & Zhu, 1996). A combination of fine ausferritic ferrite and HCA (<20%) produces an ausferrite matrix of high strength, high hardness, high wear resistance but low ductility (grades 4 and 5 of ADI) (Yazdani & Elliott, 1999a; Trudel & Gagne, 1997).

At 300-400°C austempering temperatures (high austempering temperatures) ausferritic ferrite appears with a coarse (feathery-like) morphology with HCA of less carbon content but higher volume fraction compared to the microstructure formed at low austempering temperatures

(Yazdani & Elliott, 1999a). The HCA in some areas in the matrix may not be saturated with carbon (1.2-1.6%C) and transforms to martensite at temperatures lower than room temperature or under load. A high volume fraction of HCA (25-40%) with a feathery like AF in the matrix contributes to high ductility but low strength and hardness, hence, low grades (eg: grade 1 and 2 in Table 2.1) of ADI (Yazdani & Elliott, 1999a; Elliott, 1997).

2.3.2.2 Austempering time

In order to achieve optimum mechanical properties for ADI the isothermal transformation time (austempering time) has to be chosen carefully. A short austempering time (before the time at which stage I reaction finishes) causes austenite to remain un-reacted and transforms to martensite at room temperature (Nazarboland & Elliott, 1997a; Trudel & Gagne, 1997). This martensite forms long continuous paths in the intercellular boundaries which facilitates crack growth and decreases the ductility of the material (Nazarboland & Elliott, 1997a). Another disadvantage of a short austempering time is that HCA may not be saturated with carbon and remains mechanically unstable and during deformation transform to martensite (Nazarboland & Elliott, 1997a).

A long austempering time (beyond the time at which stage II reaction starts) results in transformation of HCA to bainitic ferrite and carbide. This has two negative consequences for mechanical properties. Firstly, formation of

carbides (Equation 2.2) that is detrimental to strength and toughness of the ADI (Voigt & Loper, 1984, Nazarboland & Elliott, 1997b) and secondly, a decrease in volume fraction of HCA which is essential for ductility of the material (Aranzabal et al., 1997; Nazarboland & Elliott, 1997a).

In general, the optimum mechanical properties are obtained if the isothermal transformation time (austempering time) is chosen corresponding to the time at which the stage I reaction finishes and the time before the stage II reaction starts.

2.3.3 Effect of alloying elements and segregation

Alloying elements (other than carbon and Si) are required to avoid high-temperature reaction products such as pearlite in large section size ADI (Davis, 1996; Rouns & Rundman, 1987). Si in amounts greater than 2% is necessary to obtain graphite instead of iron carbide during the solidification of ductile iron (Rouns & Rundman, 1987). This amount of Si results in formation of carbide free bainitic ferrite (ausferritic ferrite) during the first stage of the isothermal transformation (Bhadeshia, 1992; Elliott, 1997).

In this study alloying elements (Cu, Ni, Mn and Mo) that are widely used for ADI are considered for investigation. Similar to steels, these alloying elements change the matrix austenite carbon content during austenitisation and carbon content of the austenite during the austempering process (Rouns &

Rundman, 1987; Bhadeshia, 1992; Moore, Rouns & Rundman, 1985). Alloying elements also change the rate of austenite transformation through their effect on carbon diffusion or partitioning to one phase or another (Rouns & Rundman, 1987; Bhadeshia, 1992).

However, it is well known that segregation during solidification results in a non-uniform (inhomogeneous) distribution of alloying elements throughout the matrix (Davis, 1996; Rouns & Rundman, 1987; Moore, Rouns & Rundman, 1985). For instance, Mn and Mo which promote pearlite hardening segregate into intercellular regions of the casting, promoting the formation of iron and alloy carbides (Davis, 1996; Rouns & Rundman, 1987) (Figure 2.7). In contrast, ferrite and pearlite stabilising alloying elements such as Si are present in large concentrations around graphite nodules (Davis, 1996; Rouns & Rundman, 1987; Hamid Ali & Elliott, 1996) (Figure 2.7).

The rate at which (ausferritic) ferrite is able to grow into austenite is controlled by the rate at which carbon (partitioned from the ferrite) is permitted to diffuse to the austenite (Bhadeshia, 1992; Rouns & Rundman, 1987). Austenite stabilising alloying elements such as Mn and Mo (that segregate to the intercellular area) decrease the rate of the austenite transformation, pushing the austempering time corresponding to intercellular areas longer than that for eutectic cells (around graphite nodules) (Rouns & Rundman, 1987). This leads to incomplete stage I reaction in the intercellular

area in which austenite remains un-reacted (URA) and is not carbon enriched to avoid transforming to martensite on cooling to room temperature (Rouns & Rundman, 1987). Martensite produces a relatively continuous band in the intercellular area (which facilitates crack propagation) resulting in a poor toughness (Rouns & Rundman, 1987).

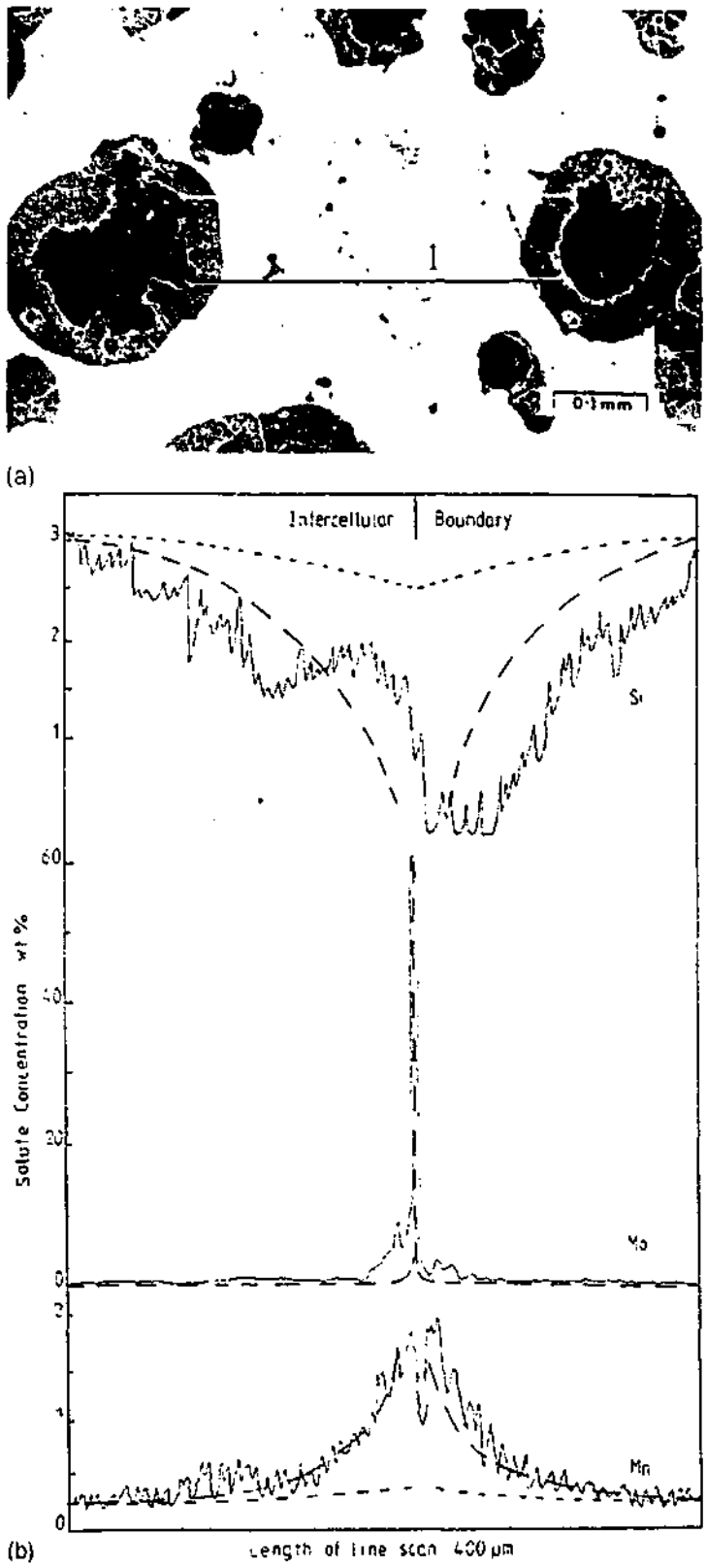

Figure 2.7 (a) EDAX line scan of as-cast microstructure corresponding to a ductile iron of composition (wt%) 3.39C, 2.56Si, 0.25Mn, 0.29Cu, 0.25Mo and 0.04Mg and (b) Mn, Mo and Si (solute) distribution along line scan 1 in Figure 2.7a (Nazarboland & Elliott, 1997b)

Nodule count of a ductile iron casting affects the gradient of the segregated alloying elements in the microstructure. Nodule count of the iron is the number of spheroidal graphite nodules per unit area (eg: nodules mm^{-2}). A small nodule count (eg: 50 nodules mm^{-2}) increases segregation of the alloying elements due to an increase in inter-nodular distance (Figure 2.8).

For instance, Liu and Elliott (1999) have shown that a decrease in inter-nodular distance from 150μm to 28μm leads to a decrease in Si concentration in the intercellular area from 2.5% to 1.6% (Figure 2.8). In contrast, Mn and Mo concentration increases in the intercellular areas with an increase in inter-nodular distance (Figure 2.8). In general, a high nodule count (eg: 150-200 nodules mm^{-2}) associated with the cast structure reduces segregation which is beneficial for austempering heat treatment (Liu & Elliott, 1999; Trudel & Gagne, 1997).

The as-cast ductile iron must posses high nodularity (>80%) to be suitable for ADI production. Nodularity indicates that what proportion of the graphite nodules are spherical in ductile cast iron. Irregular graphite particles act as stress raisers, decreasing the mechanical properties of ductile iron and ADI (Trudel & Gagne, 1997).

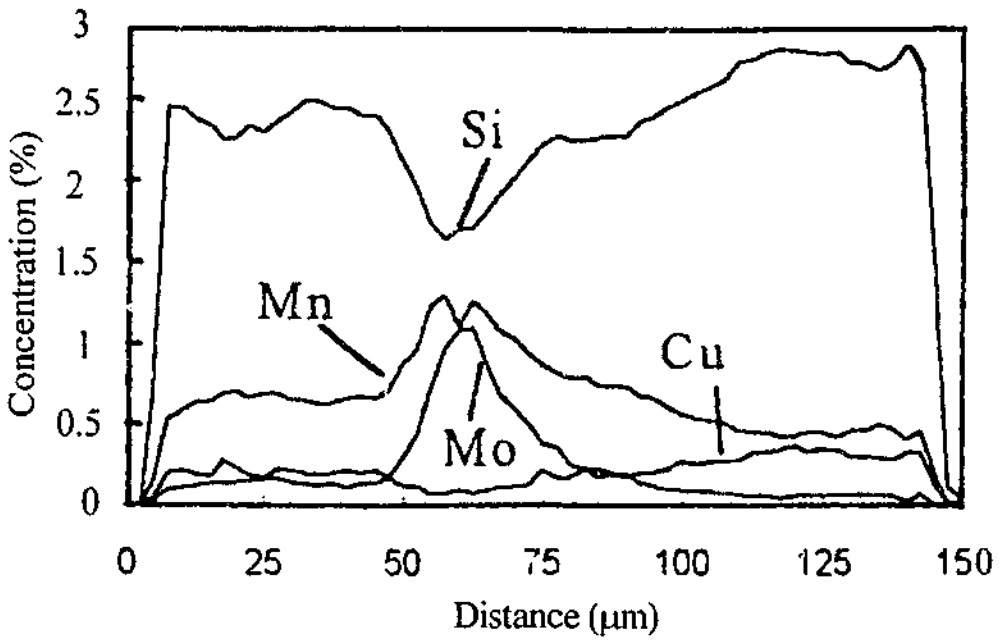

(a)

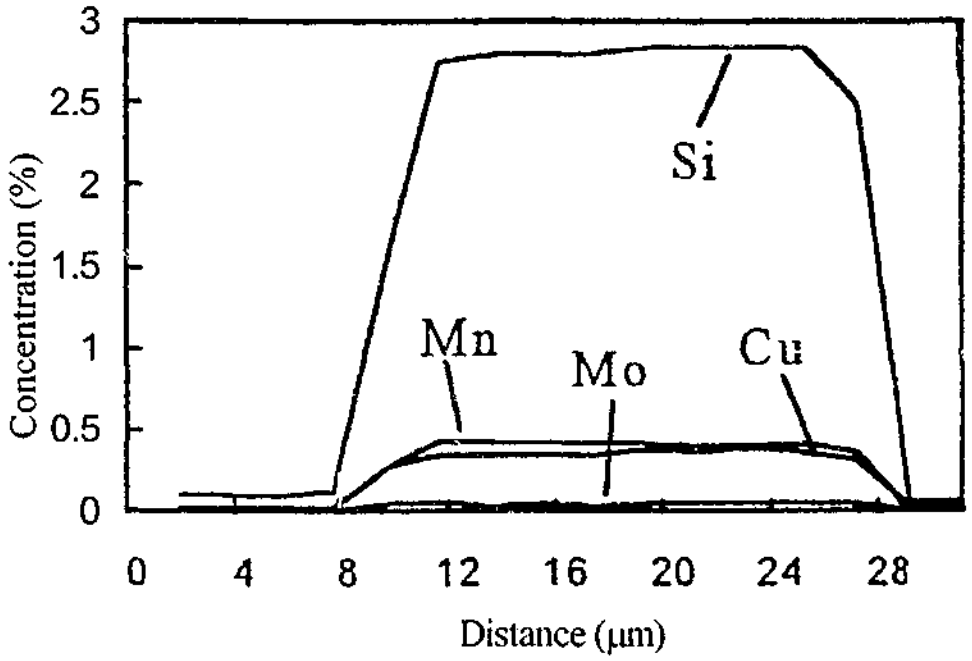

(b)

Figure 2.8 Examples of Electron Probe Micro Analysis (EPMA) line scan profiles measured on as-cast microstructure of a ductile iron of composition (wt%) 3.48C, 2.51Si, 0.56Mn, 0.311Cu, 0.15Mo, 0.04Mg, 0.016P and 0.012S for (a) large and (b) small inter-nodular distances (Liu & Elliott, 1999)

2.4 The processing window

Since segregation cannot be removed from a ductile iron microstructure, formation of martensite and carbide is inevitable in the ADI matrix. However, Elliott and Co-workers (1997) have studied the relationship between the mechanical properties and microstructural constituents in several irons and defined a window of time and temperature that is called the 'processing window'. The processing window identifies the limits for the amount of martensite (URA) and carbide that can be tolerated in the matrix to the satisfaction of the ASTM A897M:1990 standard for ADI (Figure 2.9) (Elliott, 1997; Bayati & Elliott, 1999).

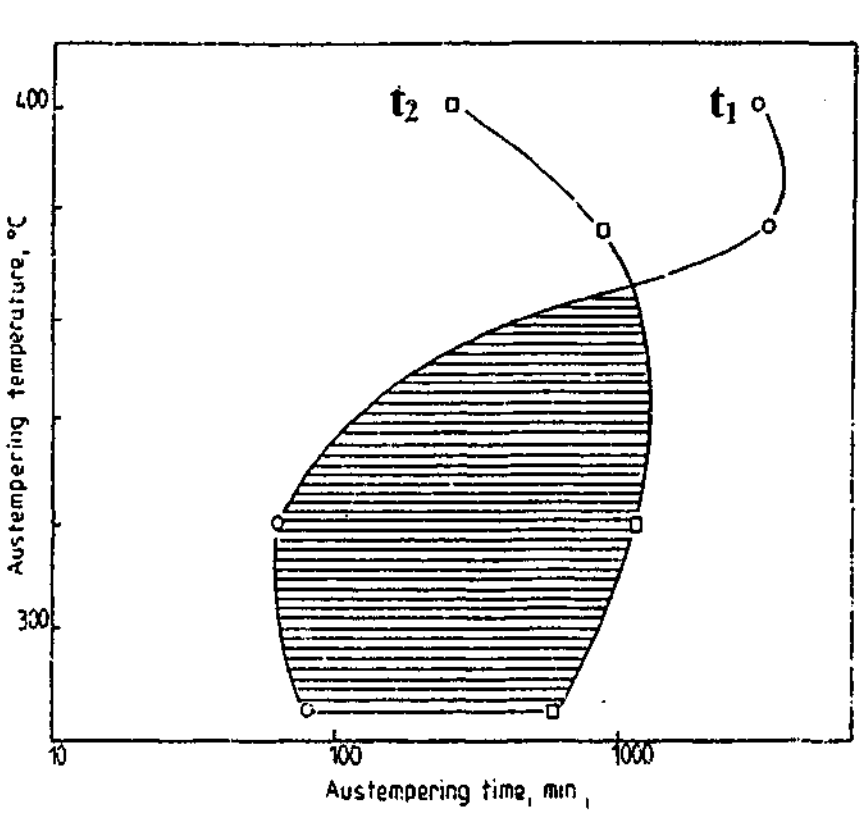

Figure 2.9 Austempering heat treatment processing window (hatched area): (t_1) the lower boundary and (t_2) the upper boundary of the processing window (courtesy of Bayati & Elliott, 1997)

A processing window (austempering window) consists of two curves; t_1 and t_2 (Figure 2.9). The lower limit (t_1) of the processing window (end of the stage 1 reaction) is defined according to the maximum volume fraction of martensite that can be tolerated in the matrix without any detriment to the minimum limits for mechanical properties defined by ASTM standard A897M:1990 (Elliott, 1997). In earlier studies, Darwish and Elliott (1993) established a 1% martensite limit for the lower boundary of the processing window. This limit increased to 3% in later studies by Hamid Ali and Elliott (1996a; 1996b) with further mechanical property investigations.

Identification of the martensite limit (3%) for estimation of the lower boundary of the processing window is important because of the segregated matrix of ADI. Non-uniform distribution of the alloying elements results in the stage I reaction occurring at a higher rate in the eutectic cells compared to the intercellular areas. For instance, due to higher Si (ferrite stabiliser) concentration in eutectic cells, stage I reaction may finish in the eutectic cells before it starts in the intercellular areas. The 3% volume fraction of martensite can be measured experimentally using a metallography technique (eg: heat tint etching) followed by image analysis (Hamid Ali & Elliott, 1996b).

However, experimental determination of the volume fraction of martensite in ADI matrix is time consuming and involves a considerable amount of experimental work. For instance, in order to determine the time at

which 3% martensite presents in the microstructure, the volume fraction of martensite has to be measured for many specimens at different isothermal holding times. Another example is that a change in alloying elements and austenitising temperature changes the carbon content of the austenite and therefore, martensite start temperature of the iron. Therefore, the volume fraction of martensite has to be measured experimentally for any change in alloying elements or austenitising temperature.

The upper boundary of the processing window corresponds to the time at which stage II reaction (Equation 2.2) starts during the isothermal holding. The fine scale of carbide brings difficulties to identifying the start of the stage II reaction in the matrix (Darwish & Elliott, 1993). Because of this, Darwish and Elliott (1993) have defined the start of the stage II reaction according to the time corresponding to the decomposition of HCA to BF and carbide (Equation 2.2). Hamid Ali and Elliott (1996a, 1996b) have shown that decomposition of up to 10% HCA does not produce enough carbide to prevent ADI from satisfying the minimum requirements of ASTM A897M:1990 standard. Therefore, Hamid Ali and Elliott (1996a, 1996b) defined the upper boundary of the processing window as the time at which the maximum amount of HCA decreases by 10%.

The volume fraction of HCA can be measured using X-Ray diffraction (XRD) analysis for several ADI specimens austempered at different holding

times (Hamid Ali & Elliott, 1996b). This presents a profile of HCA versus austempering time from which the 10% fall of HCA from its maximum value (t_2 in Figure 2.10) can be calculated (Hamid Ali & Elliott, 1996b).

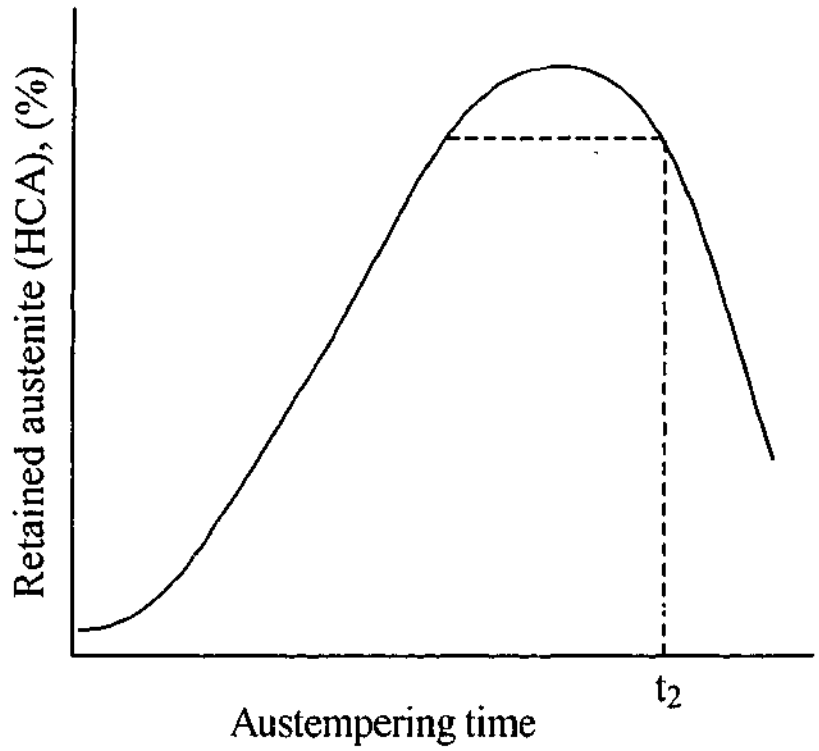

Figure 2.10 Schematic diagram representing variation of the HCA (retained austenite) with austempering time and the time for calculation of the upper limit of the austempering window (t_2) (Hamid Ali & Elliott, 1996b)

This method of calculation of t_2 presents a practical and relatively simple approach to identifying the start of the stage II reaction and has been utilised widely in the literature (Bayati & Elliott; 1997; Bayati & Elliott, 1995; Hamid Ali & Elliott, 1996b). However, calculation of the upper boundary of the processing window using XRD measurements is time consuming and expensive due to the fact that a change in alloying elements concentration,

austenitising temperature and austempering temperature changes the kinetics of the stage II reaction and therefore, the time for decomposition of HCA.

The processing window is open if stage I reaction finishes before the stage II reaction starts ($t_1<t_2$) and is closed if stage I reaction ends after start of the stage II reaction ($t_1>t_2$) (Figure 2.9) (Elliott, 1997; Hamid Ali & Elliott, 1996b). The material may fail to satisfy the ASTM standard for ADI mechanical properties if the austempering window is closed (Hamid Ali & Elliott, 1996a).

Alloying elements concentration and austenitising temperature change the boundaries of the austempering window (Figures 2.11 and 2.12). For example, an increase in Mn content of ductile iron from 0.25 to 0.67 (wt%) delays the processing window to a longer austempering time. The reason for a shift in processing window to longer austempering times is that Mn stabilises austenite and therefore, delays the stage I and stage II reactions. Among the irons in Figure 2.11, tendency for formation of carbide (specially at high austempering temperature) is the highest for the iron of 0.67% Mn (Figure 2.11). This results in closure of the processing window at the lowest austempering temperature (370°C) for iron C compared to irons A and B (Figure 2.11).

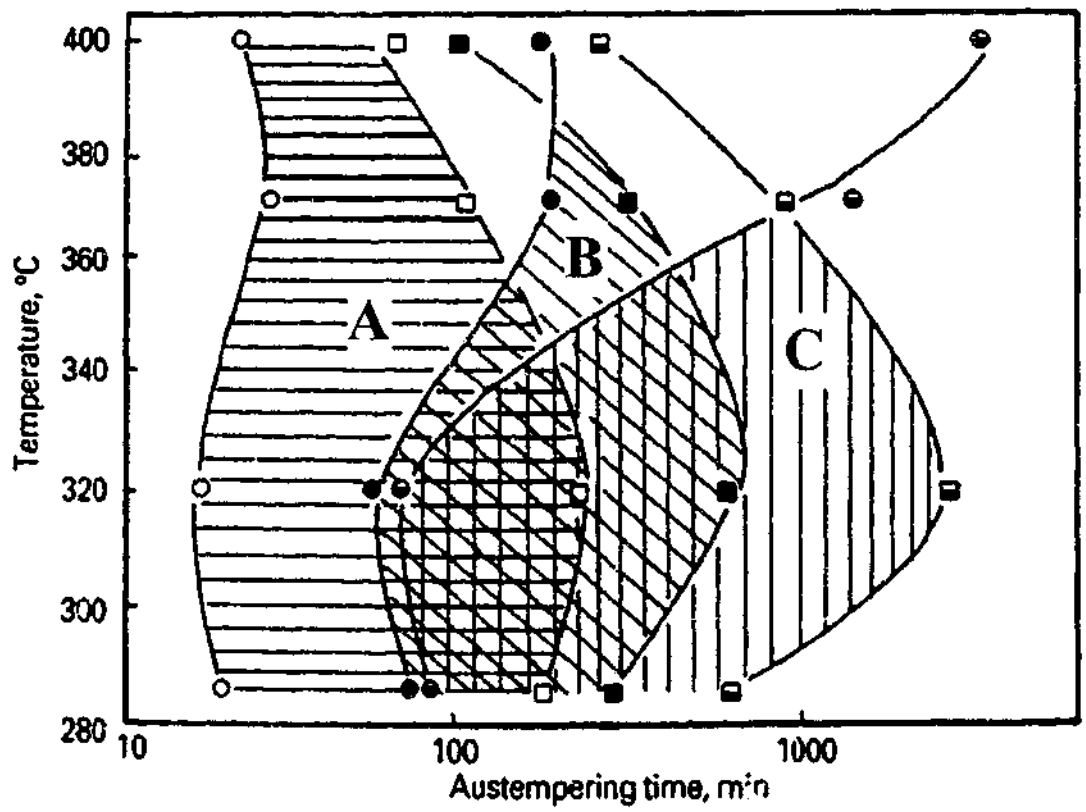

Figure 2.11 Variation of the austempering heat treatment processing window for three irons of: (A) 0.25%, (B) 0.37% and (C) 0.67% Mn content (Elliott; 1997)

The influence of austenitising temperature (cited by Elliott, 1997) on the processing window is that an increase in austenitising temperature from 870°C to 950°C narrows the austempering window and delays the processing window to a longer austempering time (Figure 2.12). This is due to an increase in carbon content of austenite with an increase in austenitising temperature (Hamid Ali & Elliott, 1997) which delays stage I (t_1) and stage II reactions (t_2) (Figure 2.12). A higher carbon content of austenite corresponding to iron C compared to irons A and B results in a larger amount of carbide (specially at high austempering temperatures) in iron C microstructure and therefore,

closure of its processing window at lower austempering temperatures (Figure 2.12) (Hamid Ali & Elliott, 1997). Closure of the processing window prevents achievement of high ductility and high toughness (low) grades of ADI.

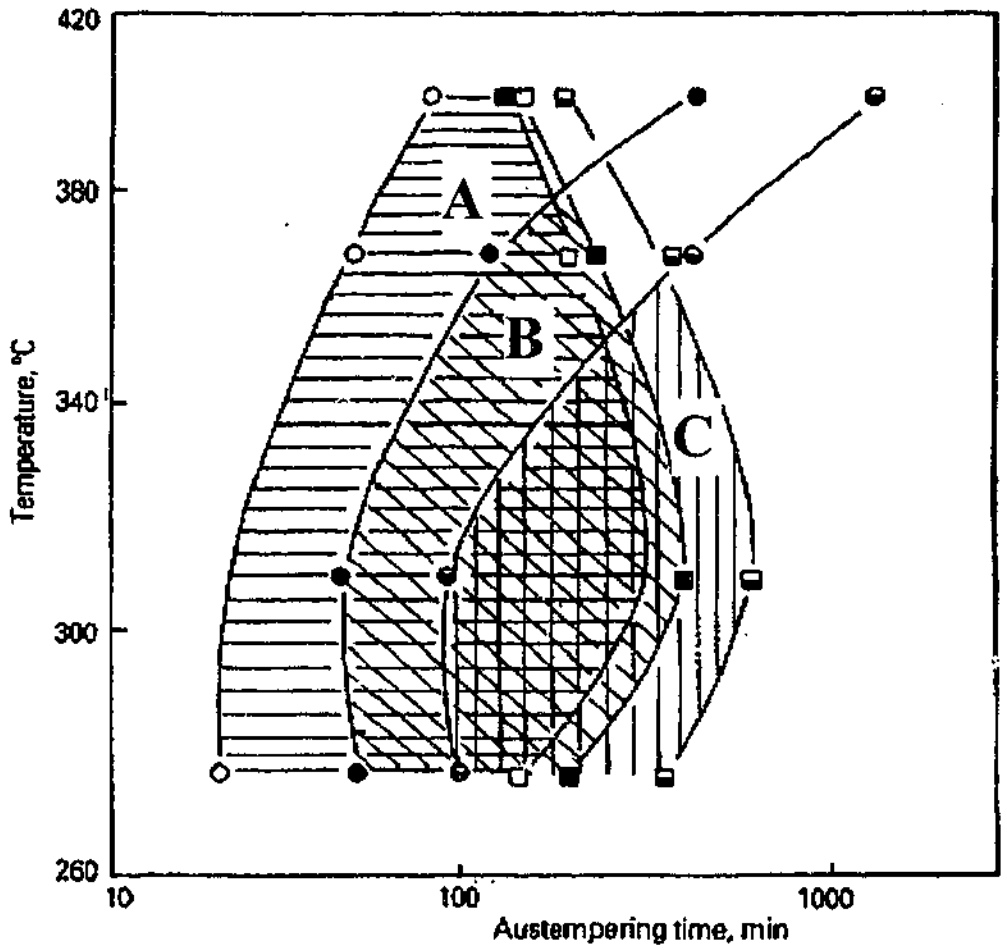

Figure 2.12 Variation of the processing window for an iron of composition (wt%) 3.5C, 2.6Si, 0.25Mn, 0.27Mo, 0.16Ni, 0.48Cu and 0.04Mg austenitised at: (A) 870°C, (B) 900°C and (C) 950°C (courtesy of Elliott, 1997)

In summary, Elliott and co-workers have identified the critical volume fraction of martensite and HCA for the lower and upper boundary of the austempering window. However, measurement of martensite and HCA involves time consuming and costly experimental work because a change in

alloying elements and austenitising temperature lead to a change in processing window boundaries. Therefore, a model for the estimation of the austempering window boundaries would be beneficial.

2.5 Background on the models for austempering process

In order to estimate the processing window for ADI we need a model to predict (i) the time for isothermal transformation of austenite to ausferrite (stage I reaction) and (ii) the time for decomposition of HCA to BF and carbide (stage II reaction). There have been some studies on estimation of the stage I reaction products (AF and HCA) during the isothermal transformation (Yescas, Bhadeshia and MacKay, 2001; James & Thomson; 1999). There has been limited studies on the second stage of the austempering reaction (Campos-Cambranis et al., 1998), however, no model is yet available for estimation of the time for transformation of HCA to BF and carbide at stage II austempering reaction.

Yescas, Bhadeshia and MacKay (2001) have developed a neural network model for quantitative estimation of retained austenite (HCA) in ADI matrix. They have trained their model based on chemical composition of the iron, austenitising time, austenitising temperature, austempering time and austempering temperature. In this model the lower boundary of the austempering window is estimated according to the time at which the volume fraction of HCA reaches its maximum. The upper boundary of the processing

window corresponds to the time at which the volume fraction of HCA starts to decline. However, these definitions for the austempering window boundaries do not correspond to Elliott's definition (Elliott, 1997) that is important for satisfaction of the ASTM standard for mechanical properties of ADI. Another constraint with the neural network model is that it has not been evaluated with experimental examinations.

James and Thomson (1998) show that the bainite model for isothermal transformation of high Si steels (Chester & Bhadeshia, 1997) can be utilised to estimate the maximum volume fraction of AF in ADI matrix. They applied the model to the ADI microstructure by modification of a function for calculation of the autocatalysis. Autocatalysis, the increase in transformation rate as ferrite nucleates adjacent to previously transformed regions, is defined as a function of the alloying composition, in particular the matrix carbon concentration (James & Thomson, 1998; Rees & Bhadeshia, 1992).

In later studies, James and Thomson (1999) have shown that their model outcomes were in good agreement with dilatometry results for calculation of the maximum volume fraction of AF (Figure 2.13). However, James and Thomson's (1999) model does not define the processing window boundaries. For instance, the time at which the stage I reaction ends (eg: 3% martensite in the matrix) and the time corresponding to the start of the stage II reaction are not computed in the model.

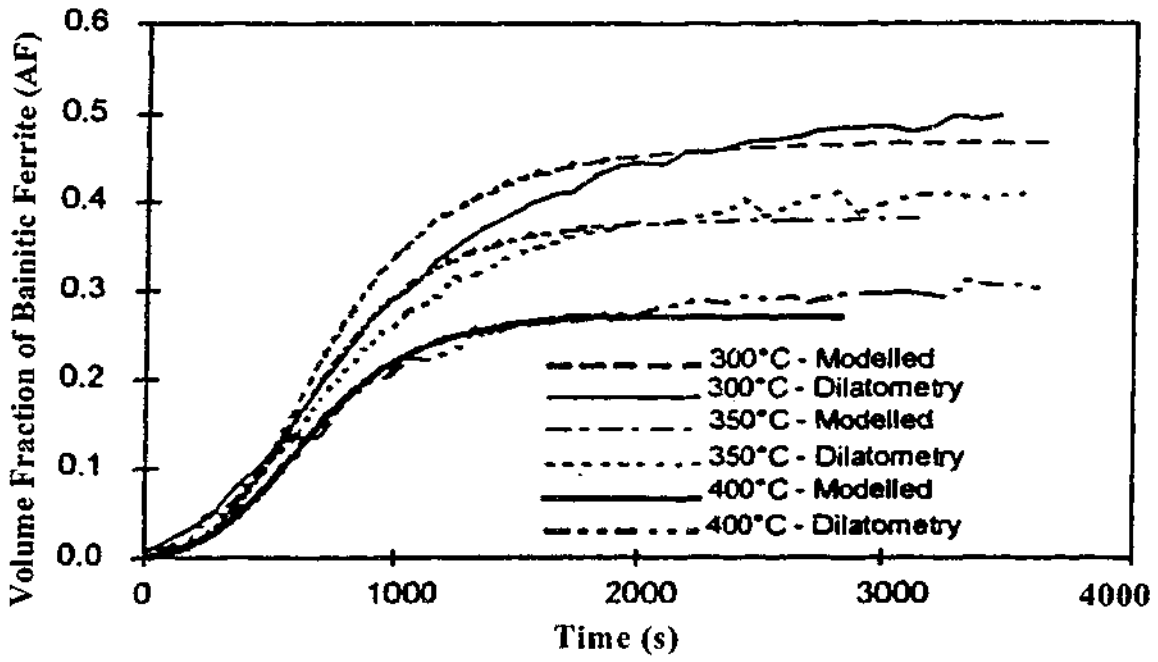

Figure 2.13 Modelled and predicted curves for the austenite to AF transformation of an austempered ductile iron of composition (wt %) Fe-3.72C-2.02Si-0.44Mn-0.035P-0.007S-0.01Ni-0.04Cu-0.051Mg (James & Thomson, 1999)

2.5.1 Background on the model for prediction of the segregation in ADI matrix

There has been considerable work done on estimation of the segregation (microsegregation) in ductile cast iron (Liu & Elliott, 1998a, 1998b, 1999). In earlier studies, Liu & Elliott (1998a) developed a numerical model that considers redistribution of solute in the micro-volume sphere. Their model allows for time dependent growth of austenite in the micro-sphere and interface movement during solidification as well as solute diffusion in the solid-liquid phases and satisfies total solute conservation in the micro-volume element. The model calculates the solute distribution in the solid and liquid

phases during solidification and solute distribution in the solid after solidification (Liu & Elliott, 1998b).

In later studies, Liu & Elliott (1999) assessed the model for calculation of the microsegregation utilising Electron Probe Micro Analysis (EPMA) line scan solute profiles. Their results, however, show that a direct comparison between line scan solute profiles and model calculations cannot be used to assess the prediction results for segregation because of the differences between solidification conditions and those assumed in the model (Liu & Elliott, 1999). In the same study, Liu & Elliott (1999) have shown that their model for prediction of the microsegregation is in good agreement with statistical analysis of the experimental data that reports solute concentration vs. normalised distance curves from the experimental data. Liu and Elliott's (1999) model, however, does not report the alloying element profiles according to the nodule count (inter-nodular distance) of the iron. This is the only information from ductile iron providers which could be used for prediction of segregation in ADI matrix.

2.6 Background on the model for austemperability

Considerable work has been done to estimate austemperability of ADI (Voigt, Lee & Tu, 1991; Lee & Voigt, 1989; Dorazil et al., 1986, 1989). Voigt, Lee and Tu (1991) have shown that austemperability (or maximum section size that can be successfully austempered) can be determined from the

austenite transformation characteristics (the hardenability) of an alloy and the quench severity of the austempering bath. In other studies, Dorazil et al. (1986, 1989) have developed an empirical model to determine the austemperability according to critical diameter (D_k) of ductile iron. Their model estimates D_k according to chemical analysis (Cu, Ni, Mn and Mo) of ductile iron and the austempering salt bath temperature.

However, Voigt, Lee and Tu (1991) and Dorazil et al. (1989) empirical models do not take into account Si concentration in the ductile iron matrix. Another shortcoming with the Dorazil model is that it does not include austenitising temperature in the model for austemperability. Si content of the ductile iron and austenitising temperature are important because of their effect on austenite carbon content, which influences austenite transformation kinetics. For instance, an increase in austenitising temperature increases austenite carbon content, which improves the stability of austenite and delays pearlite formation (increases austemperability) in ADI (Kazerooni, Nazarboland & Elliott, 1997).

2.7 Summary

It was shown that heat treatment parameters (such as austenitising temperature, austenitising time and austempering temperature) and alloying elements change the rate of isothermal transformation and therefore, the processing window for austempering (Rounds & Rundman, 1987; Moore,

Rouns & Rundman, 1985; Bayati & Elliott, 2000). It was explained that the models available for simulation of the isothermal transformation time and segregation in ADI were not adequate for prediction of the processing window boundaries.

The purpose of this study is to estimate the upper and lower limits of the processing window utilising a model for isothermal transformation of austenite to (carbide free) bainite for high Si steels. Our aim is more focused on practical application of the model for the processing window. Therefore, this work does not intend to prove any of the theories in regards to transformation mechanisms of austenite to bainite argued in the literature (Hehemann, Kinsman & Aaronson, 1972; Bhadeshia, 1992).

Another aim of this work is to determine austemperability according to austenite carbon content (austenite transformation kinetics) using simulated pearlite curve and quenching curve within a ductile iron test bar. This is a new approach for estimation of the austemperable section size of ADI.

CHAPTER 3

Experimental Techniques

3.1 Introduction

This chapter describes the experimental details involved in sample preparation, characterisation techniques and property measurements relevant to the modelling of the processing window and austemperability. Section 3.2 outlines the ductile iron samples dimensions, composition and microstructural properties. Section 3.3 provides details on equipment and experimental methods used to obtain cooling curves in a heavy section size ductile iron, and to validate the model for the processing-austemperability window. Section 3.4 explains mechanical tests applied to ADI specimens. The experimental

techniques for identification and determination of microstructural constituents are detailed in section 3.5. The final section (3.6) focuses on volume fraction of high carbon austenite (HCA) measurement using x-ray diffraction.

3.2 Materials and specimens

Two ductile iron test bars with compositions given in Table 3.1 were cast in a commercial foundry. The diameter and length of test bar 1 were 76.2 mm (3-inch) and 175 mm, respectively. Test bar 2 had 50.8 mm (2-inch) diameter and 175 mm length.

Element / Ductile Iron	C	Si	Mn	Mo	Cu	Ni	Mg
Test bar 1	3.63	2.4	0.39	0.24	0.25	0.04	0.04
Test bar 2	3.41	2.46	0.36	0.18	0.25	-	0.036

Table 3.1 Chemical compositions of ductile iron test bars (wt %)

A disc was cut from the middle section of test bar 1 after austempering heat treatment to determine the radius at which pearlite starts to form in the large section size test bar. Samples were cut from as-cast test bar 2 before heat treatment and utilised to evaluate the outcome of the models for the processing window and the processing-austemperability window. 10×10×10 mm specimens of test bar 2 were used to validated the model for the processing window. Tensile and un-notched Charpy test samples were machined from test

bar 2 according to ASTM E8M and ASTM E23 respectively, to examine the outcome of the model for the processing-austemperability window (Figure 3.1).

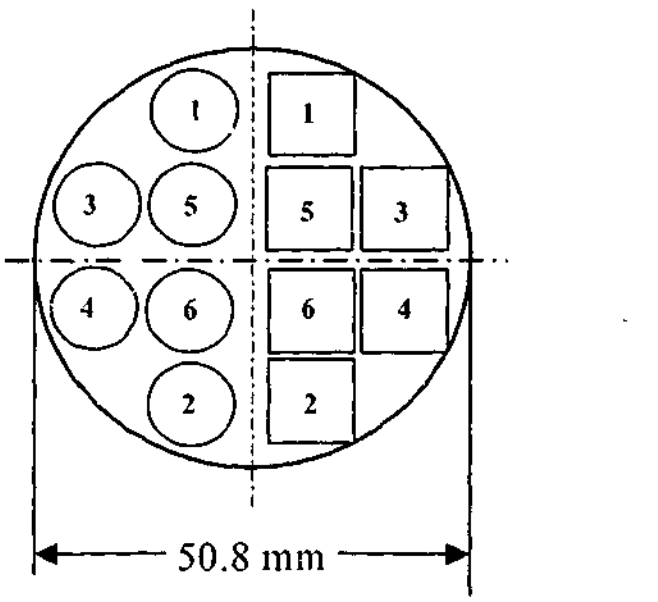

Figure 3.1 Schematic diagram for location of tensile and impact test specimens cut from test bar 2

3.3 Processing schedules and equipment

3.3.1 Heat transfer measurements

Heat transfer measurements were conducted on iron 1 test bar to determine temperature profile at the sub-surface, ¼ thickness and centre of the test bar during the cooling from austenitising to austempering temperature (Table 3.2). The profiles were used firstly, to estimate diffusivity of ductile

iron which was necessary for heat transfer model for austemperability and secondly, to evaluate the predicted pearlite curve corresponding to test bar 2.

Thermocouples	Radius from the central axis of the test bar (mm)	Height from the top of the test bar (mm)
1 (Sub-surface ~3mm)	35.5	5
2 (¼ Thickness)	19	44
3 (Centre)	0	87.5
4 (¼ Thickness)	19	131
5 (Sub-surface ~3mm)	35.5	170

Table 3.2 Co-ordinates corresponding to the locations at which temperature was measured during the heat treatment of the test bar 1

Test bar 1 was austenitised at 910°C for 2.5 hours in an endothermic controlled atmosphere furnace, quenched and isothermally held at 360°C in a salt bath containing 50% sodium nitrite and 50% potassium nitrate and finally cooled in air. The salt bath temperature was homogenised, using an impeller (Figure 3.2). Five chromel-alumel (K-type) thermocouples were located at the sub-surface, ¼ thickness, and centre of the test bar (Table 3.2).

Thermocouples were connected to a Pico TC-08 data logger and a personal computer to record the temperature during the austenitising and austempering process (Figure 3.2). To observe the temperature difference between the top and the bottom of the test bar, two thermocouples, 1 and 2, were located at the same depth as thermocouples 5 and 4, respectively (Table 3.2).

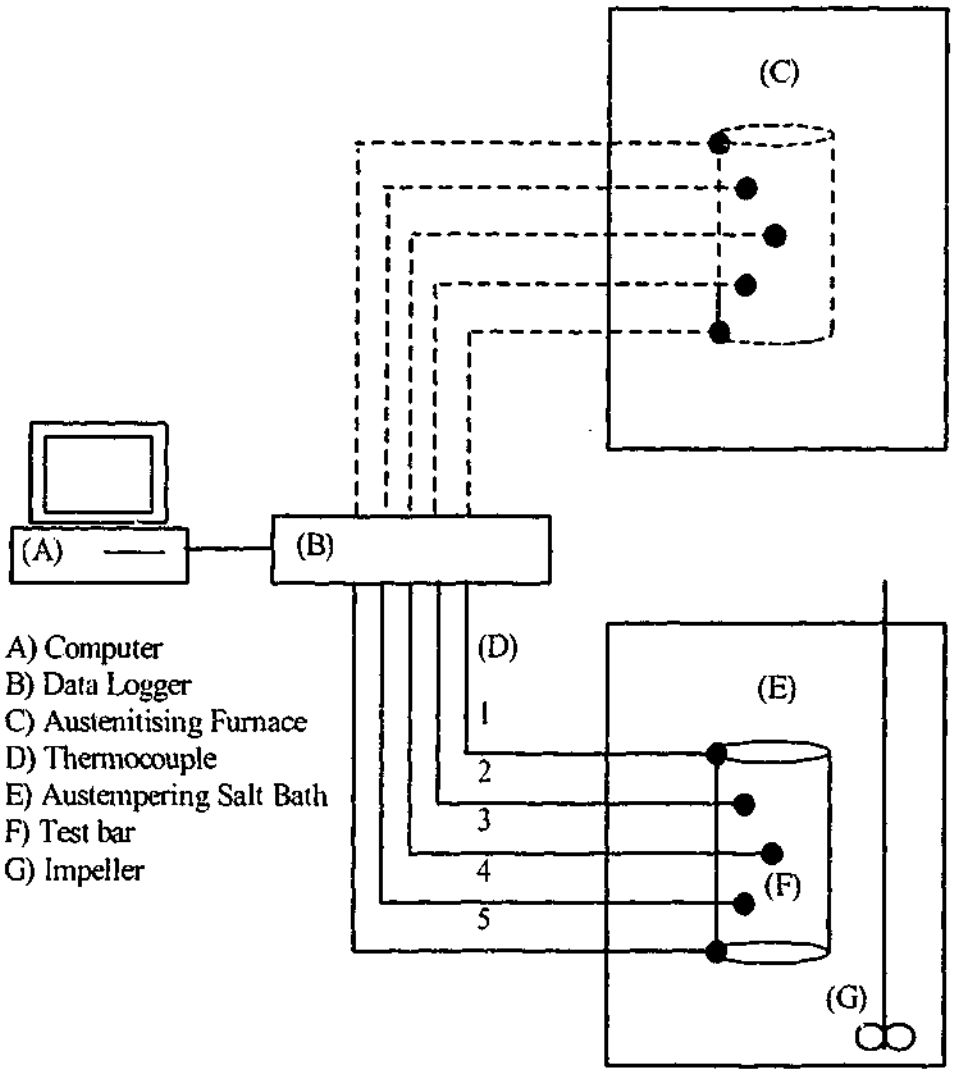

Figure 3.2 Experimental set up to achieve cooling curves at the sub-surface, ¼ thickness and centre of the test bar 1.

3.3.2 Experimental methods to evaluate the model

Three austempering temperatures 300, 340 and 380°C were selected to validate the models. Two samples were tested for each austempering temperature. In order to examine the predicted processing window associated with test bar 2, samples (10×10×10 mm) were austenitised at 905°C for 2

hours in an argon atmosphere, quenched and isothermally held in a Temposal salt bath and then cooled in air.

Experimental evaluation of the model for the processing-austemperability window was conducted utilising a set-up (Figure 3.3) to simulate the cooling rate from austenitising to isothermal transformation temperature. Impact and tensile specimens were austenitised at 905°C for 2 hours in an argon atmosphere (B-C in Figure 3.3), quenched in high speed air to the austempering temperature (C-D), isothermally held in a Temposal salt bath (D-E) and cooled in air (E-F). A K-type thermocouple connected to a data logger and personal computer was located at the end of the specimens to monitor the temperature through all heat treatment routes (Figure 3.3).

A fan was used for quenching the specimens. The fan speed (air flow) was controlled utilising a variac (Figure 3.3). The airflow (quenching rate) was calibrated for impact and tensile samples separately (Appendix I). This was due to dimensional differences between impact and tensile specimens. For instance, heat transfer was slower through impact test samples due to their thicker section size compared to tensile specimens. The calibration was carried out using dummy samples according to a procedure (Figure 3.4).

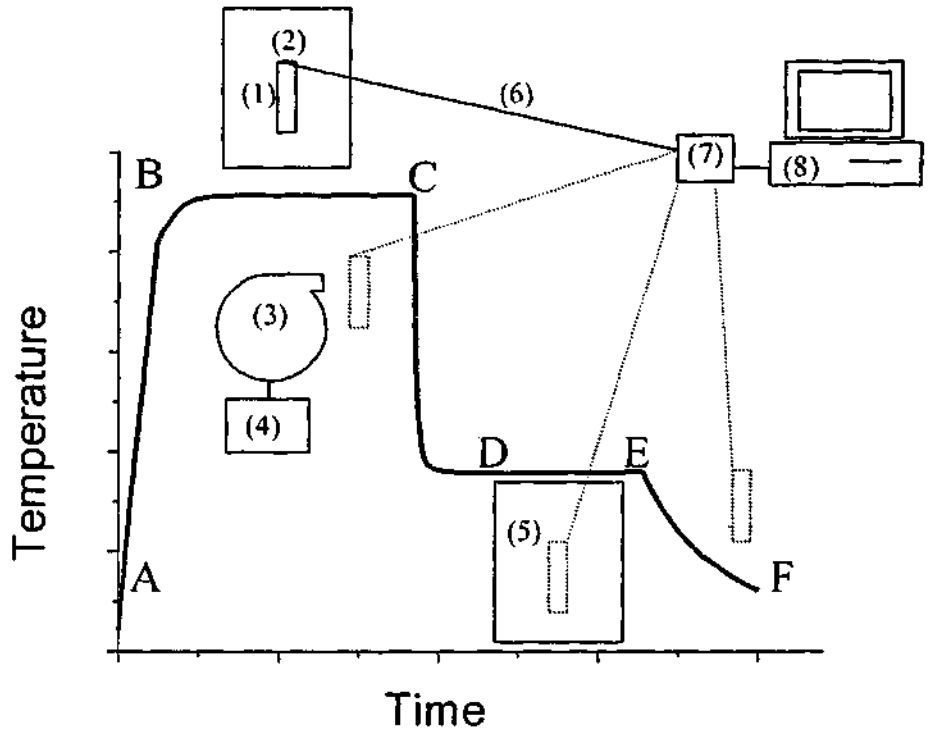

1) Specimen
2) Austenitising Furnace
3) Fan
4) Variac
5) Austempering Salt Bath
6) Thermocouple
7) Data Logger
8) Computer

Figure 3.3 Experimental set up to simulate the cooling rate corresponding to the model for austemperability

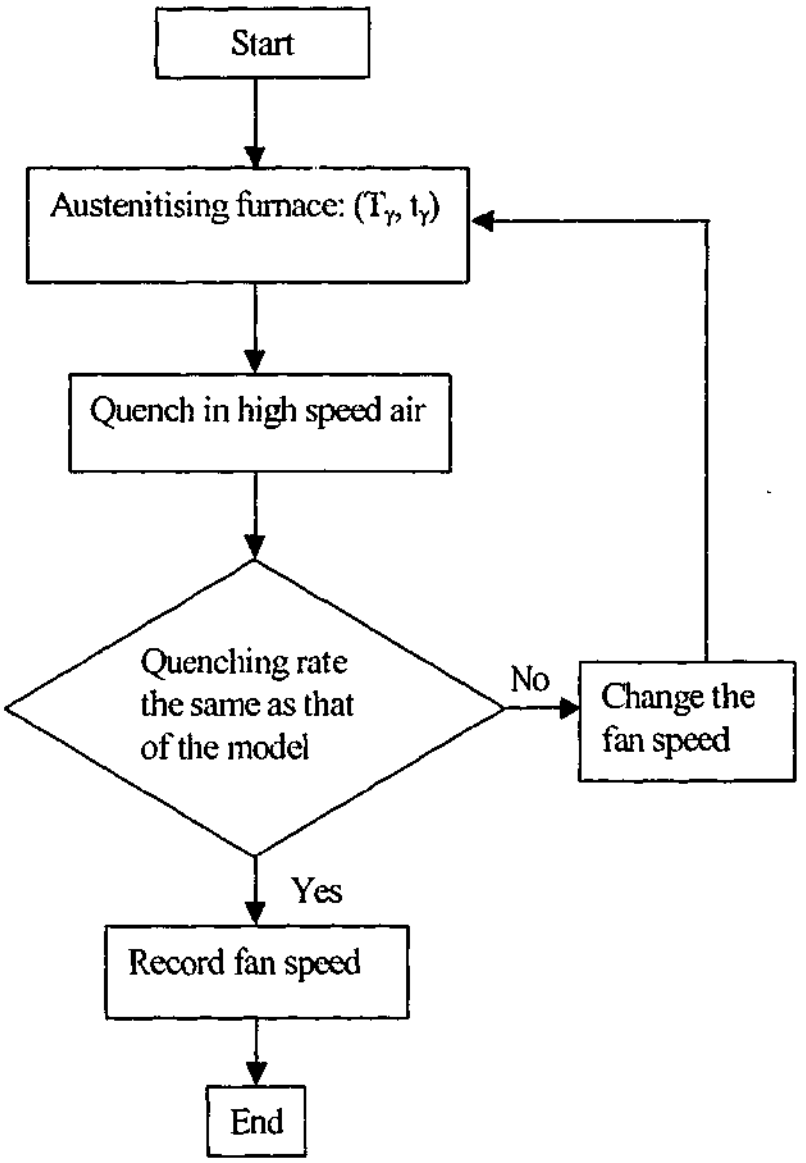

Figure 3.4 Set up for calibration of the fan

3.4 Mechanical testing

Tensile tests were performed on an Instron 4505 testing machine using a crosshead speed of 1 mm min^{-1}. A minimum of two specimens were tested for each austempering temperature. The ultimate tensile strength (UTS) and elongation to fracture were recorded. The un-notched Charpy specimens were tested at room temperature on a Mohr & Federhaff 20-kg pendulum impact

test machine. Two samples were tested for each isothermal transformation temperature.

The effect of section size on the hardness of test bar 2 was studied using a Vickers hardness machine with a load of 30 kg. Microhardness measurements were made on a Matsuzawa Seiki MHT-1 microhardness tester with a load range of 25 to 100 grams to characterise microstructural constituents such as pearlite, eutectic carbide and ausferrite formed in test bar 1. The average value of 10 tests was recorded for both hardness and microhardness tests.

3.5 Metallography and image analysis

Polished samples of iron 1 were etched in 2% Nital to reveal pearlite and ausferrite in the microstructure. In order to observe some special microstructural constituents such as martensite, retained austenite and eutectic carbide, a heat tinting method was utilised (Kovacs, 1987). Heat tinting is an oxidation process and preserves phases in distinct colours (Table 3.3 and Figure 3.5) (Kovacs, 1987). Iron 2 samples were polished and etched in 2% Nital, heated in air at 260°C for eight hours and cooled to room temperature. All polished, etched and heat tinted samples were qualitatively investigated using an Olympus PMG3 microscope.

Microstructural constituent	**Colour**
Unreacted austenite	Light blue
Reacted, high carbon austenite	Purple
Ferrite	Beige
Eutectic carbide	White or cream
Martensite	Dark blue

Table 3.3 Phases and corresponding colours for ADI microstructure after heat tinting (Kovacs, 1987).

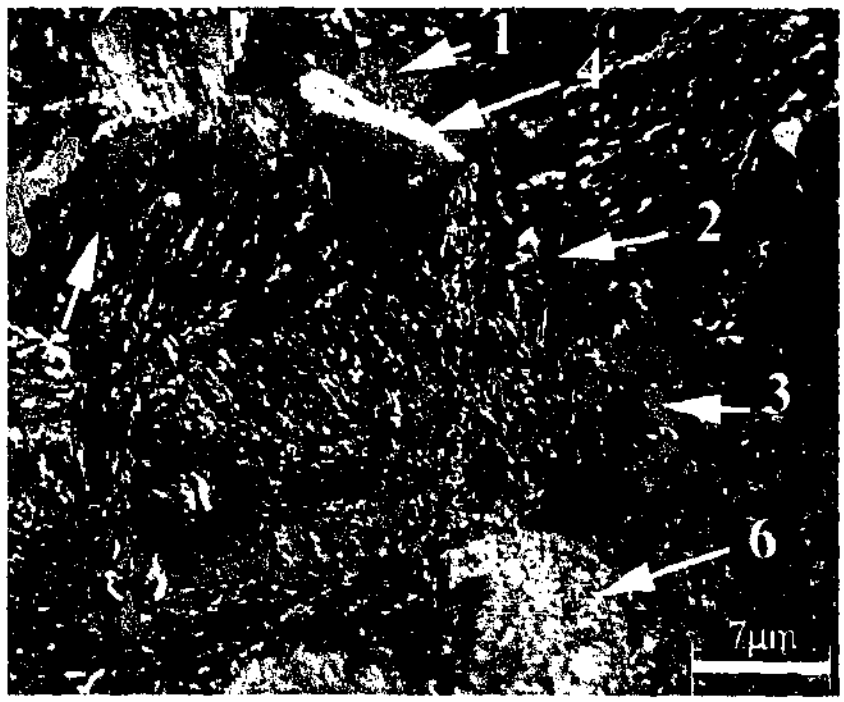

Figure 3.5 An example of a heat tint etched specimen: 1- Low carbon (retained) austenite, 2- High carbon (retained) austenite, 3- (Ausferritic) ferrite, 4- Eutectic carbide, 5- Martensite and 6- Graphite nodule

Images were acquired from the matrix using an Olympus DP10 digital camera. Image analysis software (Adobe PhotoShop ™ equipped with image analysis plug-ins) was utilised to determine the volume fraction of martensite

and prior austenite grain size (G_A). The volume fraction of martensite was measured by area percent, that is the ratio of the total detected phase area to image frame area. Ten images were acquired for each measurement and the average value was recorded.

Prior austenite grain size is one of the inputs of the model. The prior austenite grains were revealed using a sample of test bar 2 with dimensions 10×10×10 mm. The specimen was austenitised at 910°C for 2 hours and quenched in water. The sample was polished and etched in 4% Nital and then light polished to disclose the prior austenite grains. The prior austenite grain size was quantified based on the number of grains located in a straight line at a specific magnification as:

$$G_A = \frac{\text{Number of grains crossed by the straight line}}{\text{Length of the straight line / Magnification}} \qquad (3.1)$$

The average number of grains was determined in 4 different directions (0°, 45°, 90° and 135°) with 5 lines at each direction. The magnification was 150 times.

3.6 X-ray analysis

One of the most accurate methods for retained austenite measurement is X-ray analysis, with almost 0.2% precision (Cullity, 1978). This technique was used to obtain the volume fraction of HCA in microstructures. Scanning was performed using a Phillips PW 1130 diffractometer with graphite

monochromated CuK_α radiation at 40 kV and 30 mA in the 2θ range of 40-90° at a rate of 0.05 degree.min^{-1}. The integrated intensities of the $(200)_\alpha$, $(211)_\alpha$, $(200)_\gamma$ and $(220)_\gamma$ peaks were used in Direct Comparison Method (DCM) to determine the volume fraction of HCA (Cullity, 1978). In DCM, austenite content of ADI is measured by direct comparison of the integrated intensity of austenite line with the integrated intensity of (ausferritic) ferrite using the following equation:

$$\frac{I_\gamma}{I_\alpha} = \frac{R_\gamma}{R_\alpha} \times \frac{C_\gamma}{C_\alpha} \tag{3.2}$$

where, I_γ is integrated intensity per unit length of diffraction line (J.s^{-1}.m^{-1}) for austenite phase, I_α is integrated intensity per unit length of diffraction line (J.s^{-1}.m^{-1}) for (ausferritic) ferrite phase, C_γ is the value for austenite (%), C_α is the value for ferrite (%) and R_γ and R_α are values that dependant on the crystal structures and lattice parameters of the austenite and ferrite phases, respectively (Cullity, 1978; Darwish & Elliott, 1993).

The value of C_γ/C_α can therefore be obtained from a measurement of I_γ/I_α and a calculation of R_γ and R_α. Once C_γ/C_α is found, the value of C_γ can be obtained from the additional relationship (Equation 3.3) (Cullity, 1978).

$$C_\gamma + C_\alpha = 1 \tag{3.3}$$

In choosing diffraction lines to measure, overlapping or closely adjacent lines from different phases must be avoided (Cullity, 1978). The

"Traces*" software was utilised for curve fitting to minimise errors introduced from background radiation.

* Traces is a software product of Diffraction Technology Pty. Ltd.

CHAPTER 4

Modelling

4.1 Introduction

This chapter describes the approach to model the processing window and austemperability of ADI. Section 4.2 provides details on calibration of a model for isothermal transformation of austenite to bainite for estimation of the processing window boundaries. Section 4.3 outlines a model for prediction of the heat transfer in a large section size austempered ductile iron and application of the model for prediction of the austemperability with respect to the pearlite curve of the TTT diagram. The final section (4.4) introduces the processing-austemperability window which provides a more informative tool for the design of ADI.

4.2 The model for prediction of the processing window

In order to model the processing window, a mathematical model which was developed for isothermal transformation of high silicon (Si) steels was utilised (Chester & Bhadeshia, 1997). This approach was chosen due to similarity between the microstructural constituents in both ADI and high silicon steels. For instance, the presence of a high amount of Si leads to the formation of carbide-free ferrite (Bhadeshia, 1992). Another example is that the austenite phase enriches with carbon during isothermal transformation, leading to formation of high carbon austenite (HCA) (Bhadeshia, 1992; Rees & Bhadeshia, 1992).

However, ADI has a higher carbon concentration (up to 2%) in the matrix and a more largely segregated microstructure compared to high Si steels. Thus, the model for bainite transformation in high Si steels (Chester & Bhadeshia, 1997) cannot be directly applied to ADI, and thus it needs to be calibrated.

4.2.1 The model for isothermal transformation in high Si steels

Many different mechanisms and theories have been developed for the isothermal transformation of austenite to bainite (Hehemann, Kinsman & Aaronson, 1972; Bhadeshia, 1992). The only comprehensive model for prediction of the time for isothermal transformation of austenite to bainitic

ferrite has been developed for steels in which carbide precipitation is suppressed (Bhadeshia, 1992; Takahashi & Bhadeshia, 1991). The relevance of such a model to ADI results from the high (>1.5%) Si content of ADI, in which austenite transforms to carbide free (ausferritic) ferrite through ejection of carbon from ferrite to the neighbouring austenite.

The transformation model explains the incomplete reaction phenomenon according to the assumption that (carbide free) bainitic ferrite grows without diffusion (Takahashi & Bhadeshia, 1991). The incomplete reaction occurs in steels where other reactions do not interfere (or occur simultaneously) with the growth of bainitic ferrite. The maximum volume fraction of ferrite that forms at the extended holding time at the isothermal transformation temperature is far below that expected on the basis of equilibrium or paraequilibrium transformation. The reaction stops when the carbon concentration of the residual austenite approaches the T_o curve, which describes the locus of all points on the phase diagram where austenite and ferrite of the same chemical composition have identical free energies.

A reconstructive transformation mechanism in which carbon partitions during growth (so that the product phase is not limited by austenite grain boundaries, and can grow to any size) can continue until the austenite reaches its equilibrium or paraequilibrium composition (Takahashi & Bhadeshia, 1991). Knowing this, Takahashi and Bhadeshia (1991) have shown that the

incomplete reaction phenomenon can be explained by carbon being partitioned into the residual austenite immediately after the growth event.

Bhadeshia (1982) developed a mathematical model of the overall transformation kinetics of the bainite reaction in respect to steels bearing more than 1.5% Si (that suppresses carbide formation in bainitic ferrite). To achieve a realistic time, Rees and Bhadeshia (1992) refined the model for isothermal transformation taking into account two criteria. Firstly, the nucleation rate corresponding to Widmanstätten start temperature (W_s) is constant for all steels and secondly, driving force for bainitic transformation decreases as transformation proceeds due to carbon enrichment of untransformed austenite. Chester and Bhadeshia (1997) further modified this model calculating the bainite sub-unit size according to austempering temperature.

The isothermal transformation model (Equation 4.1) estimates the time for the displacive formation of carbide free bainitic ferrite from austenite in high Si (>1.5%) steels. In this model, carbon partitions into the residual austenite shortly after the growth of each bainite plate is extinguished (Bhadeshia, 1982, Chester & Bhadeshia, 1997). Equation 4.1 calculates the transformation time required to form a given volume fraction of (carbide free) bainitic ferrite (v). The amount of (bainitic) ferrite phase is expressed as a normalised volume fraction, ξ, with respect to the maximum possible volume fraction θ determined from the limiting carbon concentrations (calculated from

the lever rule). Terms of Equation 4.1 are provided in list of symbols (pages X, XI and XII).

$$t_A = \frac{e^C}{A(B+1)}\begin{Bmatrix} e^E\left(\ln\left|1+B\xi\right| + f(-(E+D\xi)) - f(-E)\right) \\ -e^{-D}\left(\ln(1-\xi) + f(D(1-\xi)) - f(D)\right) \end{Bmatrix} \quad (4.1)$$

where $A = \frac{uK_1}{\theta}$, $B = \beta\theta$, $C = \frac{K_2}{RT_A}\left(1 + \frac{\Delta G^0_m}{r}\right)$, $D = \frac{K_2\left(\Delta G^0_m - G_N\right)}{rRT_A}$, $E = \frac{D}{B}$, $\xi = \frac{\nu}{\theta}$, $f(x) = \frac{x}{1\times 1!} + \frac{x^2}{2\times 2!} + \frac{x^3}{3\times 3!} + \ldots$, $\theta = \frac{(x_{T_0} - \bar{x})}{(x_{T_0} - x_\alpha)}$, $\beta = \lambda_1\left(1 - \lambda_2\bar{x}\right)$ and $K_1 = \left(\bar{L}K_1^{\cdot}\right)^{-1}$.

Equation 4.1 estimates the time for isothermal transformation according to austempering temperature (T_A), the initial value of the maximum nucleation energy (ΔG°_m), the universal nucleation function (G_N), mole fraction of carbon at the temperature above which the austenite to ferrite transformation cannot take place without diffusion (X_{To}), equilibrium mole fraction of carbon in ferrite (X_α), mole fraction of carbon in the alloy (ξ), the grain size of the parent austenite (G_A) and constant parameters K, K_1, K_2, λ_1 and λ_2 are given in Table 4.1.

Constant	K_1	K_2	λ_1	λ_2	R	r
Value	34.456	2.098×10^4	147.5	30.327	8.134	2540

Table 4.1 Constant values in Equation 4.1 (Chester & Bhadeshia, 1997)

The value for ΔG°_m, G_N, X_{To}, X_α, and θ parameters in Equation 4.1 are computed for test bar 2 and presented in Appendix II. These values can be

determined by running the freely-available programs detailed in the Materials Algorithm Project Program Library (1999a, 1999b and 1999c).

In contrast to steels, carbon concentration in the ADI matrix is lower than that reported in the chemical analysis because of the formation of graphite during solidification. Hence, the matrix carbon concentration for ADI is estimated as:

$$X_c = -0.435+0.335\times10^{-3}T_\gamma+1.61\times10^{-6}T_\gamma^2+0.006(\%Mn)-0.11(\%Si) \\ -0.07(\%Ni)+0.014(\%Cu)-0.3(\%Mo) \qquad (4.2)$$

where X_c is the estimated percentage of carbon concentration of the austenite at the austenitising temperature (T_γ) (Nazarboland & Elliott, 1997a).

Autocatalysis

Among the variables in Equation 4.1, the autocatalysis factor (β) is critical for our study. Autocatalysis is a term commonly associated with martensitic transformations in steels in which nucleation of martensite is believed to begin at structural imperfections in the parent phase (Bhadeshia, 1992). Bhadeshia (1992) has revealed that the initial density of pre-existing defects (eg. in austenite) is not large enough to explain the kinetics of martensitic transformation. The extra defects necessary to account for the faster than expected transformation rates of austenite to martensite are attributed to autocatalysis. New nuclei are induced as a result of the formation of martensite plates that are available at nucleation sites for further

transformation. For instance, in strain-induced autocatalysis, the creation of more potent nucleation defects is caused by some plastic accommodation in the parent phase (Bhadeshia, 1992).

Another example is 'interfacial autocatalysis'. This refers to the nucleation of new martensitic units from the existing martensite-austenite interfaces. Hence, the initial formation of a plate of martensite stimulates a disproportionately large degree ('burst') of transformation (Bhadeshia, 1992).

Bhadeshia (1992) explains that the autocatalysis occurs as a result of the severe elastic and plastic disturbance of the austenite in the immediate vicinity of a plate of martensite that is due to the shape change during the martensitic transformation. On this basis, autocatalysis occurs during the bainitic reaction due to similar martensitic transformation shape deformation.

However, a significant difference is that the driving force for the bainitic reaction is considerably lower than that for the martensitic reaction, which leads to fewer available nucleation sites in the vicinity of bainite plates (Bhadeshia, 1992). Further nucleation on the previously formed plates is limited by carbon build up at the ferrite-austenite interface (Rees & Bhadeshia, 1992). This leads to a temporary local decrease in the driving force for diffusionless transformation and consequently a delay in the isothermal transformation time (austempering time) corresponding to bainitic transformation (Rees & Bhadeshia, 1992).

Rees and Bhadeshia (1992) propose the following equation for calculation of the autocatalysis factor β:

$$\beta = \lambda_1\left(1 - \lambda_2 \bar{x}\right) \tag{4.3}$$

where ξ is the mean value for mole fraction of carbon in the alloy and λ_1 and λ_2 are empirical constants (Table 4.1).

4.2.2 Application of the model for isothermal transformation

Application of the isothermal transformation model to ADI is justified on the assumption that transformation to ausferrite is controlled by carbon partitioning into the retained austenite. However, other studies show that the model is not directly applicable for prediction of the time for ausferritic reaction and needs some modifications (James & Thomson, 1999).

In proposed model of this study, β is a function of the mole fraction of carbon ($\bar{x}$) and the austempering temperature (T_A). A change in the mole fraction of carbon ($\bar{x}$) in the parent austenite leads to a change in the amount of carbon ejected from ferrite to the neighbouring austenite (Bhadeshia, 1992). This effect is accommodated in the model using Equation 4.1. However, this equation overestimates the time for ausferritic reaction. Austempering temperature changes the mobility of carbon and leads to a change in autocatalysis. For instance, at high austempering temperatures carbon atoms ejected from ferrite propagate more easily to the neighbouring austenite,

facilitating nucleation of new neighbouring ferrite plates. This causes an increase in the autocatalysis factor and consequently a decrease in time for isothermal transformation.

The effect of alloying elements and austempering temperature on the autocatalysis is complex and no model is yet available for the β, $\bar{x}$ and T_A relationship. For this reason, the experimental data sourced from the literature for three irons (Tables 4.2 and Figure 4.1) were used to compute a function for β which calibrates the isothermal transformation model for ausferritic reaction. The following explains this approach to estimate the start of the processing window.

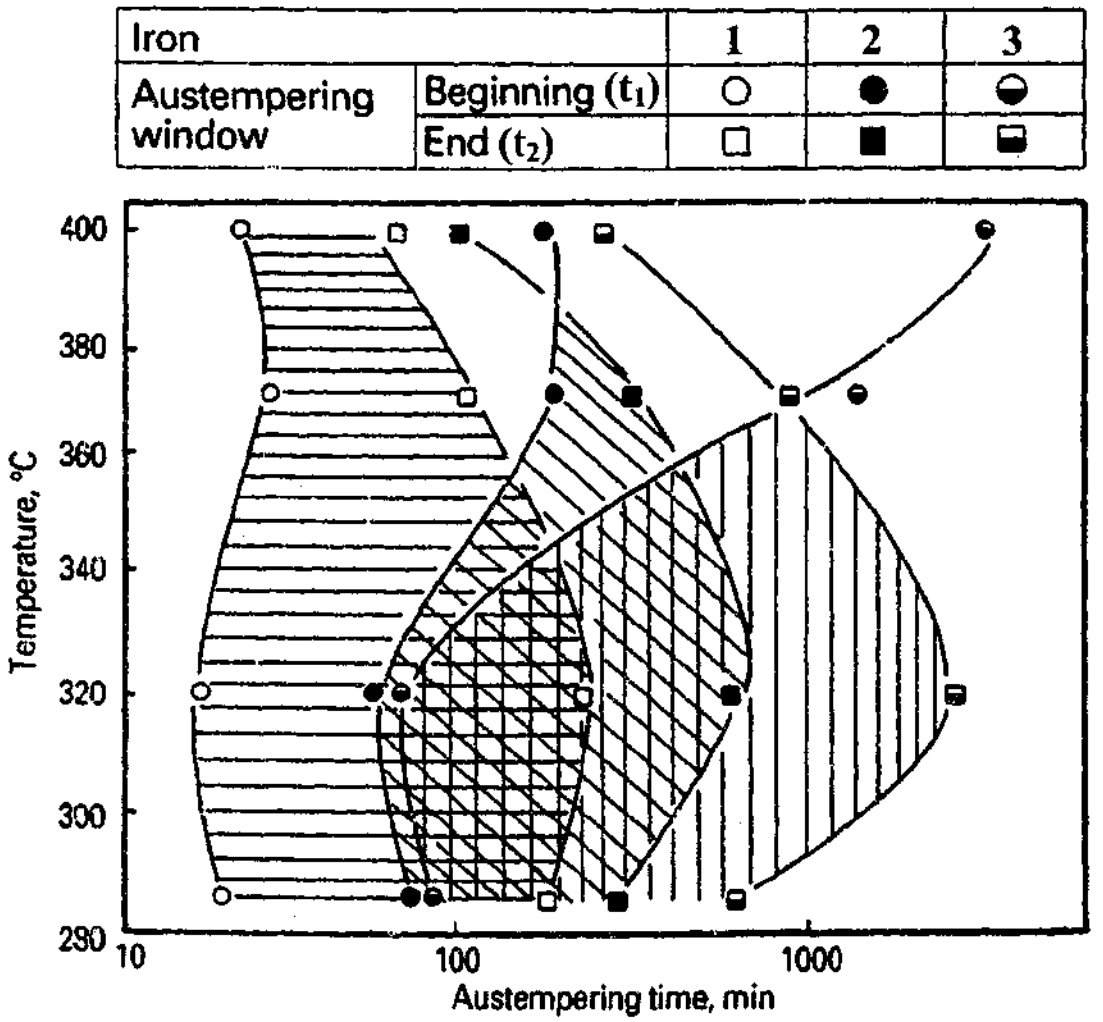

Figure 4.1 The processing window for irons 1, 2 and 3 austenitised at 920°C (Elliott, 1997).

Iron	%C	%Si	%Mn	%Mo	%Cu	%Mg	$\bar{x}$
1	3.55	2.72	0.25	0.25	0.25	0.04	0.0381
2	3.59	2.56	0.37	0.25	0.29	0.04	0.0389
3	3.52	2.64	0.67	0.25	0.25	0.04	0.0386

Table 4.2 Alloy composition and mole fraction of carbon for three processing windows in Figure 4.1

4.2.2.1 Calibration of the isothermal transformation model for estimation of the lower boundary of the processing window

The volume fraction of the microstructural constituents (except graphite nodules) during the stage I reaction can be estimated from Equation 4.4:

$$\text{Volume of the microstructural constituents (\%)} = \%\nu + \%3\alpha_M + \%V_{HCA} \qquad (4.4)$$

where V_{HCA} is the volume fraction of high carbon austenite, α_M is volume fraction of martensite and $\nu=\xi.\theta$ is the volume fraction of the ausferritic ferrite.

At the beginning of the processing window (end of the stage I reaction) the ausferritic ferrite volume fraction reaches its maximum value ($\xi=1$ and $\nu=\theta$). Therefore, at $\xi=1$ the master Equation 4.1 estimates the time for the lower boundary of the processing window, knowing that θ is obtained from the lever rule in the para-equilibrium Fe-C phase diagram and the rest of the variables, except β, are calculated from the TTT diagram program (Materials Algorithm Project Program Library, 1999a). Hence, β is the only variable in Equation 4.1 that controls the rate of ausferritic ferrite formation during the isothermal transformation. Using Equation 4.1 and the experimental t_1 of irons 1, 2 and 3 (Figure 4.1), β was calculated for austempering temperatures of 285, 320, 375 and 400°C (Figures 4.2 and 4.3).

Computation of β was achieved utilising the functions, subroutines and programs provided by Bhadeshia and Co-workers in the Materials Algorithm Project (MAP) web site (Materials Algorithm Project Program Library, 1999a, 1999b, 1999c) the flow diagram for which is shown in Figure 4.2. Equation 4.1 was coded into a computer program, called MAP_STEEL_NEW2 (Materials Algorithm Project Program Library, 1999b). The data necessary for this program were alloying elements concentration, T_A, t_l, T_γ, ΔG°_m, X_{To}, ξ, θ, G_A, $\bar{x}$ and four fitting parameters (Table 4.1).

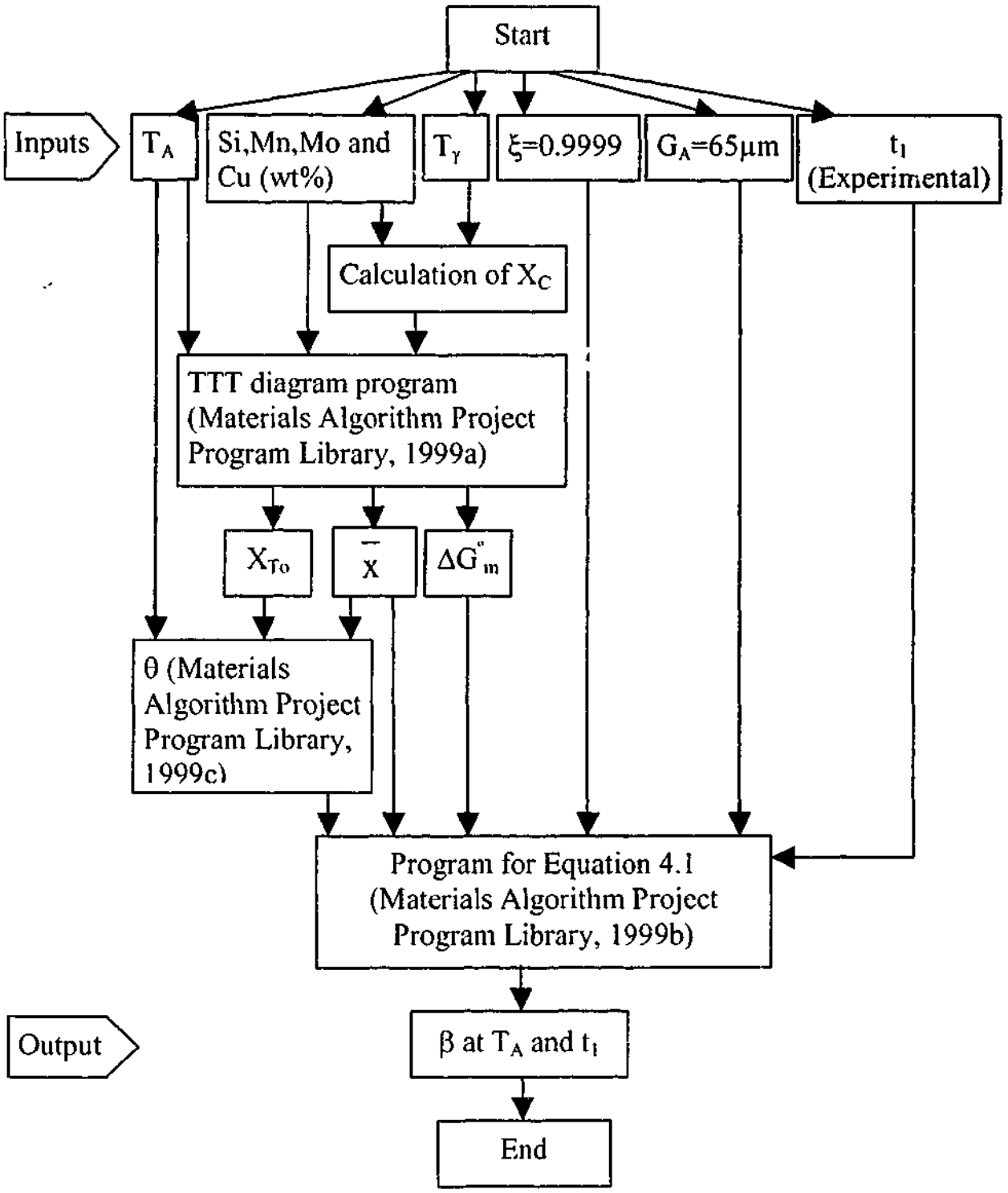

Figure 4.2 Flow chart for calculation of β corresponding to ausferritic reaction in irons 1, 2 and 3

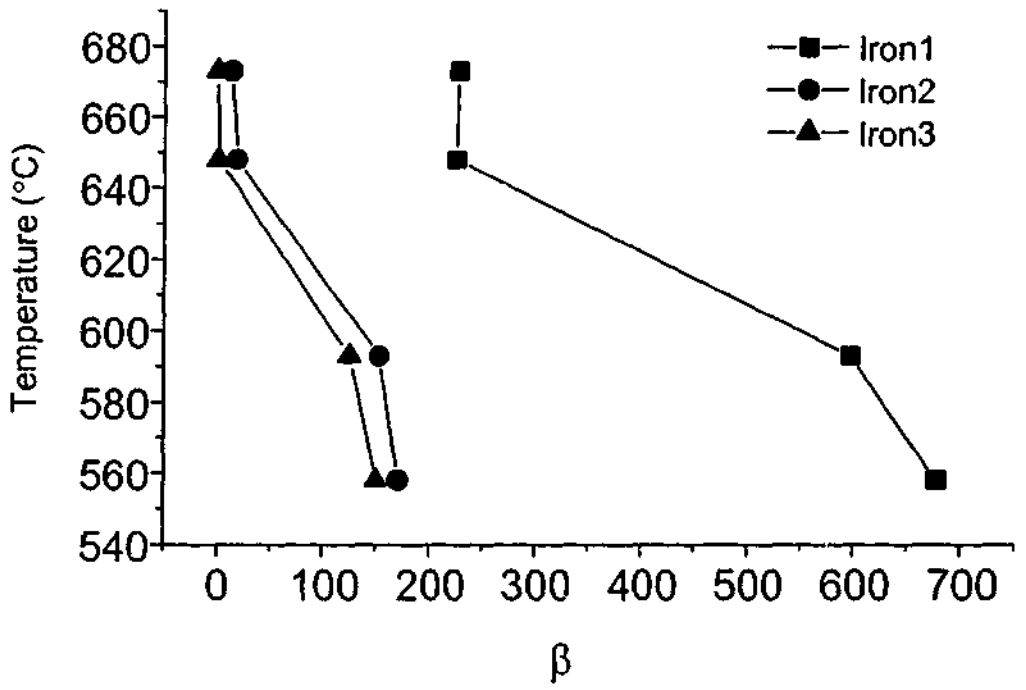

Figure 4.3 Variation of β calculated according to experimental processing windows of iron 1, 2 and 3 with austempering time and temperature

The values of T_A, t_1, T_γ were obtained for irons 1, 2 and 3 from experimental data sourced from the literature (Figure 4.1). The parameters ΔG°_{m}, X_{To} and $\bar{x}$ were obtained from the program MAP_STEEL_MUCG73 (Materials Algorithm Project Program Library, 1999a) and θ was computed using the MAP_STEEL_MV function (Materials Algorithm Project Program Library, 1999c) (Figure 4.2).

The prior austenite grain size (G_A) was measured to be 65μm for test bar 2 and considered to be the same for irons 1, 2 and 3. This was due to the fact that the G_A corresponding to irons 1, 2 and 3 were not available in the literature and austenitising time (2 hours) and temperature (910-920°C) were almost similar for all irons. The effect of alloying elements on G_A was not

considered in this study. Further study is needed to find out the relationship between the G_A, austenitising time, austenitising temperature and composition of the ADI.

The carbon concentration in the matrix (X_c) was estimated according to Equation 4.2 (Figure 4.2). The factor ξ is selected very close to unity, but not equal to unity for all calculations due to the mathematical limitations for the solution of Equation 4.1 (Figure 4.2).

Substitution of a function (Equation 4.5) for $\beta=f(T_A, \bar{x})$ in the Equation 4.1 calibrates the equation for estimation of the lower boundary of the processing window. The β function was calculated from the β values of irons 1, 2 and 3 (at all austempering temperatures) (Figure 4.3) using a multiple linear regression technique (Montgomery & Runger, 1999).

$$\begin{aligned}\text{Log}(\beta) = &- 759.58 - 132.79\,T_A + 0.24\,T_A^2 + 7085.54\,\bar{x}\,T_A \\ &- 91935.54\,\bar{x}^2\,T_A - 12.84\,\bar{x}\,T_A^2 + 166.51\,\bar{x}^2\,T_A^2\end{aligned} \qquad (4.5)$$

The number of significant figures was selected as two to minimise the difference between the estimated values for β (Equation 4.5) and the β values corresponding to experimental processing windows of irons 1, 2 and 3. This was due to the fact that a further increase in the number of significant figures (>2) did not decrease the standard error corresponding to the β function (Figure 4.4).

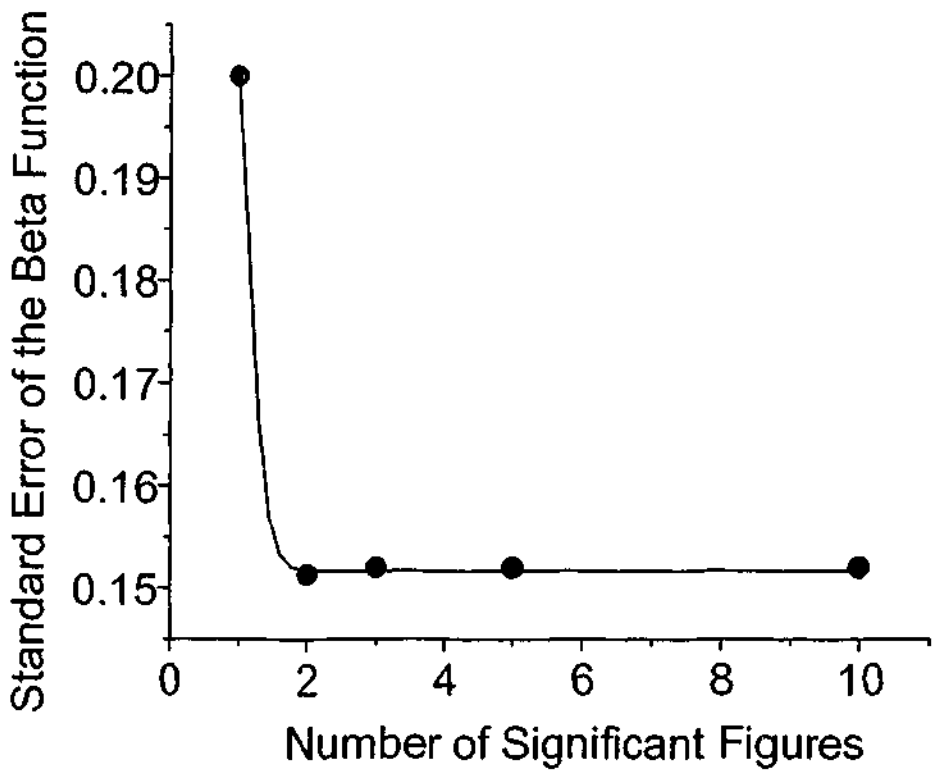

Figure 4.4 Variation of the β function (Equation 4.5) standard error with respect to the number of significant figures.

The multiple linear regression was used to calculate the β function instead of other approaches such as kinetics and thermodynamics methods because of segregation in the ADI matrix. Segregation of alloying elements results in a local change in mole fraction of carbon from graphite nodules towards intercellular areas. For instance, a lower carbon concentration ($\bar{x}$) around graphite nodules (due to a higher concentration of ferrite stabilising alloying elements (ie: Si and Cu) compared to intercellular areas leads to an increase in autocatalysis and consequently a shorter time for isothermal

transformation. However, no model is yet available to predict autocatalysis according to alloying elements segregation profile in ADI matrix.

The calibrated Equation 4.1 (with β from Equation 4.5) takes alloying element concentrations (wt.%), austenitising temperature (T_γ) and austempering temperature (T_A) as input and computes the time for ausferritic ferrite to reach its maximum value at t_1 (Figure 4.5). The carbon concentration in the matrix was estimated from Equation 4.2. $\bar{x}$, ΔG°_{m} and X_{To} were computed from the TTT diagram program (Materials Algorithm Project Program Library, 1999a) and θ was calculated from the MAP-STEEL-MV program (Materials Algorithm Project Program Library, 1999c) (Figure 4.5).

The outcome of the calibrated model for the lower boundary of the processing window in the austempering range of 285-400°C follows the experimental data (sourced from the literature) corresponding to irons 1 and 2 (Figures 4.6a and 4.6b). However, the model curves do not match the experimental points corresponding to iron 3 at 380 and 400°C at which the processing window is closed ($t_1 > t_2$) (Figure 4.6c). This difference between the calibration and experimental data is discussed in Chapter 6.

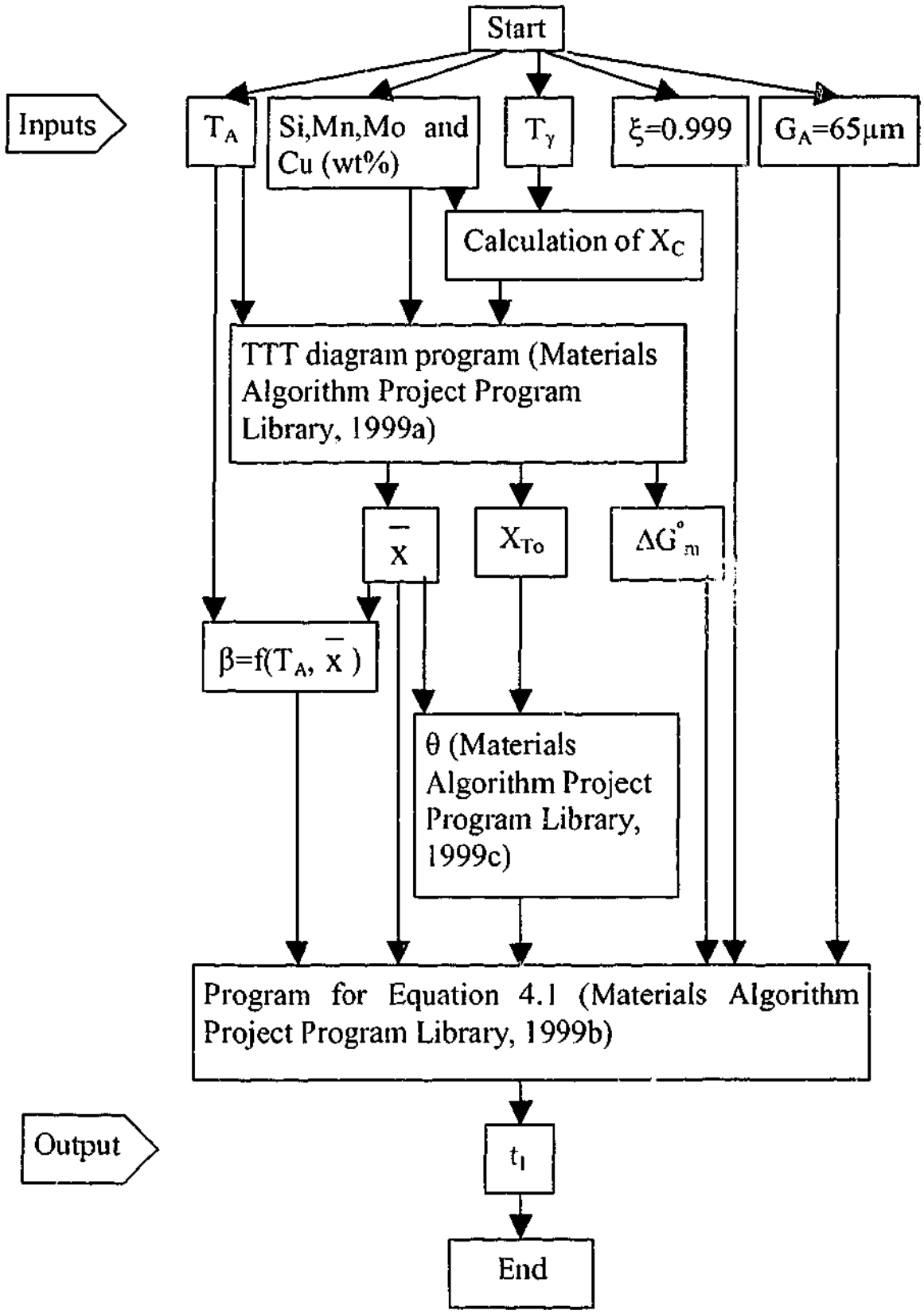

Figure 4.5 Flow chart for calculation of the lower (t_l) boundary of the processing window using the calibration β function.

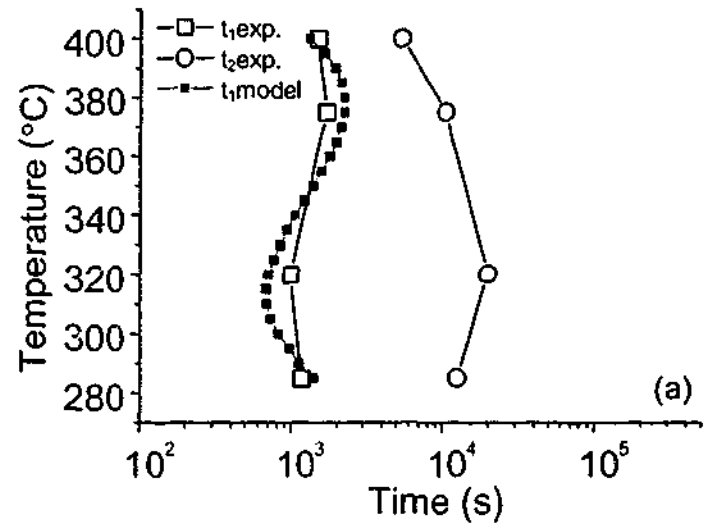

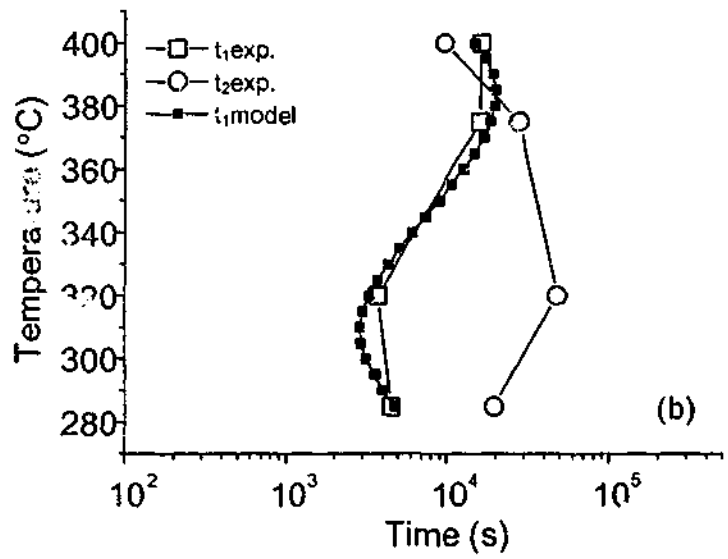

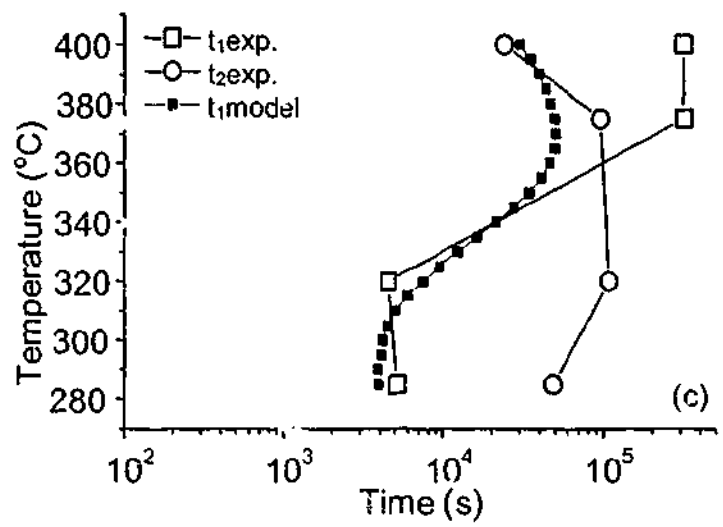

Figure 4.6 Comparison of experimental data (Elliott, 1997) and the (calibrated) model results for lower boundary of the iron 1 (a), iron 2 (b) and iron 3 (c) processing windows at austenitising temperature of 920°C.

4.2.2.2 Estimation of the upper boundary of the processing window

The upper limit of the processing window is the time at which 10% of the HCA (reacted stabilised austenite) transforms to bainitic ferrite and carbide during the isothermal transformation (Elliott, 1997). However, no model is presently available to predict this time. For this reason, a value for Δt ($\Delta t = t_2 - t_1$) which represents the time interval at which HCA starts to transform to bainitic ferrite and carbide at t_1 and reaches 90% of its maximum value at t_2 was utilised for estimation of the upper limit of the processing window (the hatched area corresponding to each processing window in Figure 4.1).

The experimental values for Δt (Figure 4.7) of irons 1, 2 and 3 were utilised to fit a multiple linear function to the austempering temperature and mole fraction of carbon (Equation 4.6). In order to minimise the difference between the experimental values and the outcome of the multiple linear function, the logarithm of Δt was chosen for the calculation of Equation 4.6. Similar to the β function, two significant figures were chosen for Equation 4.6 to minimise the standard error corresponding to the Δt function.

$$\text{Log}(\Delta t) = -1959.79 + 151810.11\,\bar{x} - 2708917.71\,\bar{x}^{2} - 6.75\,T_A + 189.75\,\bar{x}\,T_A - 2.04\,\bar{x}^{2}\,T_A^{2} \qquad (4.6)$$

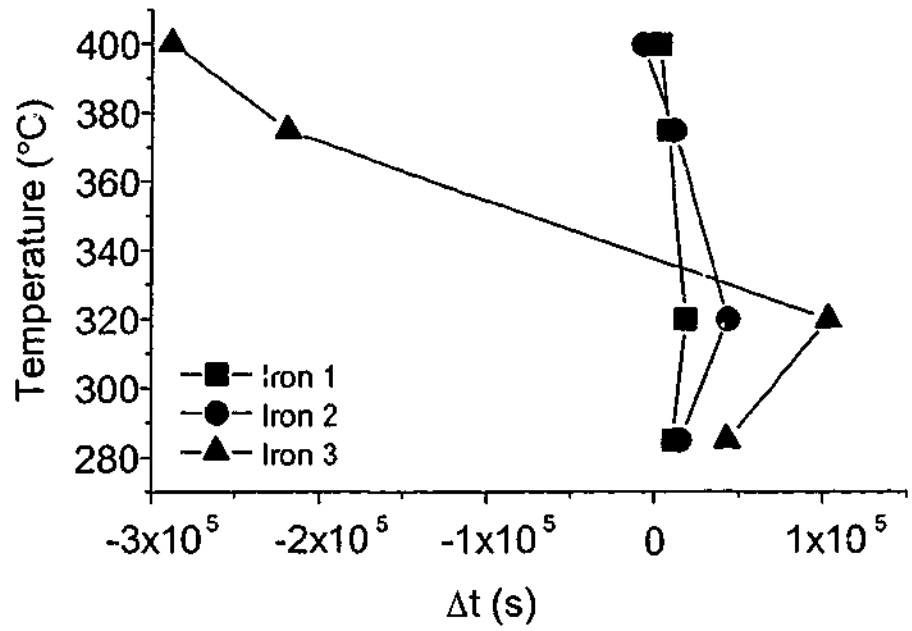

Figure 4.7 Variation (with austempering time and temperature) of Δt calculated from processing windows corresponding to irons 1, 2 and 3

The value for this function was added to the value for t_1 (Figure 4.5) to calibrate the model for the upper boundary of the processing window (Figure 4.8). All of the parameters in Figure 4.8 were calculated similar to the parameters in Figure 4.4. Computed upper limits (t_2) of the processing window for irons 1, 2 and 3 in the austempering range of 285-400°C similarly followed the experimental data for the points at which the processing window was open ($t_1<t_2$) (Figure 4.9). However, the model curves did not match the experimental points at which the processing window was closed ($t_1>t_2$) (Figures 4.9b and 4.9c). This difference between the calibration and experimental data is discussed in Chapter 6.

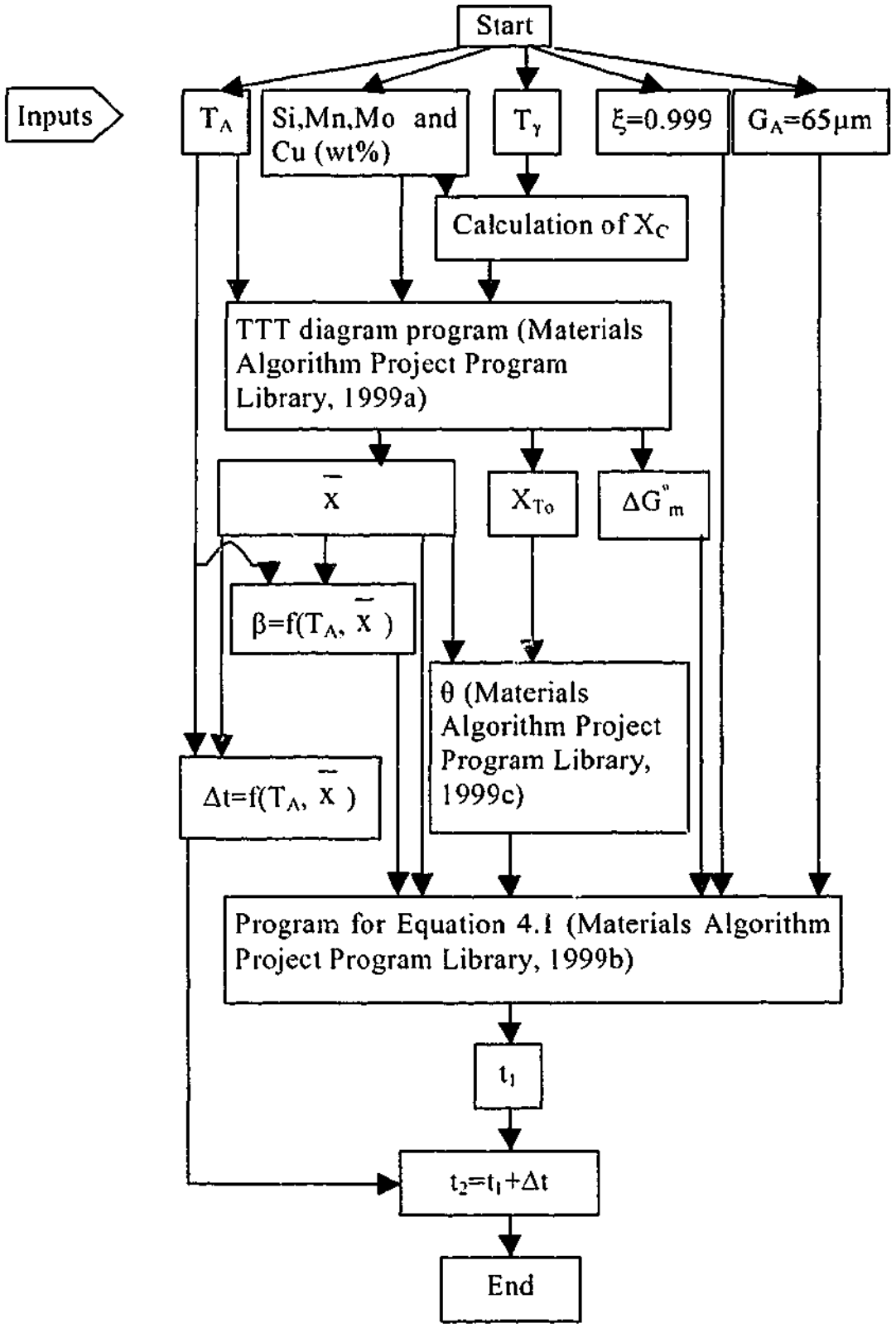

Figure 4.8 Flow chart for calculation of the lower (t_1) and upper (t_2) boundaries of the processing window using the β and Δt functions.

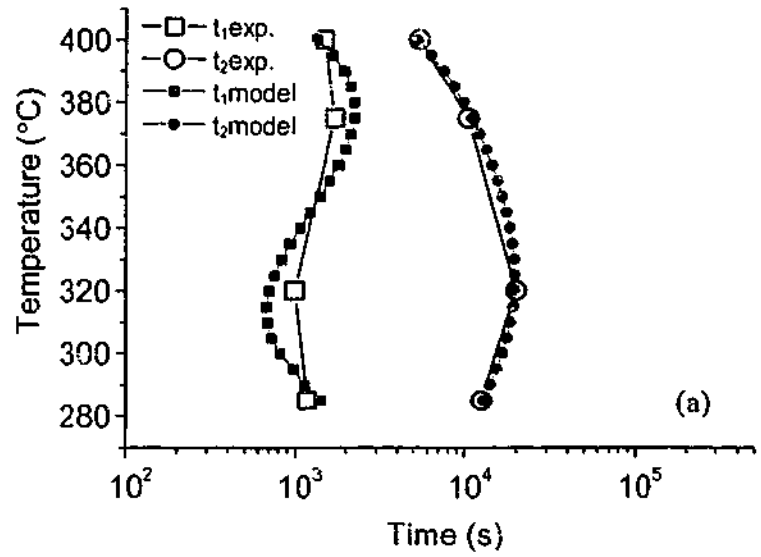

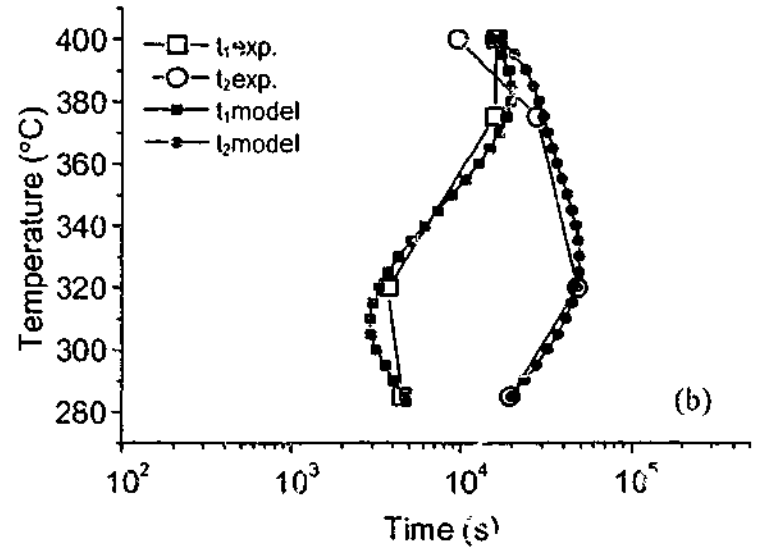

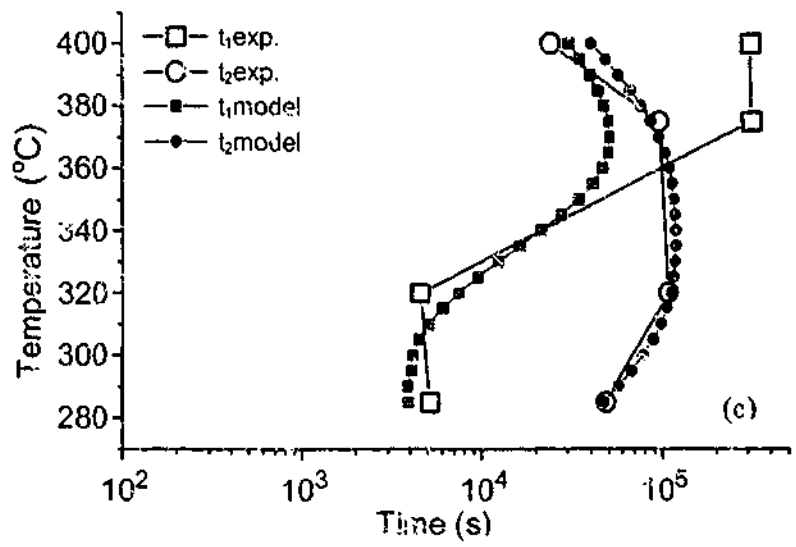

Figure 4.9 Comparison of the experimental data (Elliott, 1997) and the model results for the upper and lower boundaries of iron 1 (a), iron 2 (b) and iron 3 (c) processing windows at austenitising temperature 920°C.

4.3 The model for prediction of austemperability

Austemperability of ADI is computed by means of the maximum radius of a ductile iron test bar in which no pearlite is present in the microstructure after an austempering heat treatment. Obviously, the austemperability results can be reported in many other ways such as diameter of the test bar or distance from the quenching end. In order to estimate the austemperability, a mathematical model for heat transfer in a solid cylinder and a program for prediction of the TTT diagram were utilised.

Austemperability was calculated according to the temperature at which a simulated cooling curve at the centre of an ADI test bar touches the tip of the pearlite curve of the TTT diagram. A question may arise as to why the TTT diagram was chosen instead of the CCT diagram when it is possible to calculate the CCT diagram according to the TTT diagram data using the Scheil equation?

The TTT diagram was chosen instead of the CCT diagram to adopt a more conservative approach with respect to pearlite formation (Honeycombe & Bhadeshia; 1995), and therefore avoid overestimation of the time and temperature at which pearlite starts to form in the matrix. Overestimation of the time for pearlite formation in the matrix may occur as a result of segregation that is not included in this study.

4.3.1 The model for heat transfer

The aim of the heat transfer model is to predict the cooling curve from the austenitising to the austempering temperature in the thickest section size of the material that can be used later for prediction of the austemperability of ADI. For this reason, a model for conduction of heat in an infinite solid cylinder was chosen that requires solution of the following partial differential equation (Poirier and Geiger, 1994).

$$\frac{\partial T}{\partial t} = \alpha \nabla^2 T = \alpha \left[\frac{\partial^2 T}{\partial x^2} + \frac{\partial^2 T}{\partial y^2} + \frac{\partial^2 T}{\partial z^2} \right], \tag{4.7}$$

where T is temperature, t is time, x, y, z are coordinates in space and α is the thermal diffusivity of the material (Poirier & Geiger, 1994).

When temperature is not a function of time but only depends on location in cylinder the following boundary condition applies to the Equation 4.7.

$$\nabla^2 T = \frac{\partial^2 T}{\partial x^2} + \frac{\partial^2 T}{\partial y^2} + \frac{\partial^2 T}{\partial z^2} = 0 \ , \tag{4.8}$$

It was assumed that the internal resistance of the body controls the cooling in material. In this case the surface temperature immediately changes to the final temperature which is the temperature of the quenching media. Taking into account this assumption, solution of the differential Equation 4.7

for an infinite cylinder using separation method (Poirier & Geiger, 1994) will be:

$$\frac{T-T_f}{T_i-T_f}=\frac{4}{\pi}\sum_{n=0}^{\infty}\frac{(-1)^n}{2n+1}\exp\left[\frac{-(2n+1)^2\pi^2}{4}\frac{\alpha t}{R_c^{\,2}}\right]\cos\frac{(2n+1)\pi}{2}\frac{x_c}{R_c}\,, \qquad (4.9)$$

where T is the specimen temperature (°C), T_i is the initial temperature (°C), T_f is the final temperature (°C), α is thermal diffusivity (m^2s^{-1}), R_c is radius (m), x_c is distance from the surface (m), t is time (s) and n is a constant. The value for 'n' was chosen as 60 to make Equation 4.9 smooth for our application (Figure 4.10). Equation 4.9 estimates the quenching curve at any location within an infinite test bar by calculation of time at different temperatures with x_c, R_c, T_f, T_i as (input) constants.

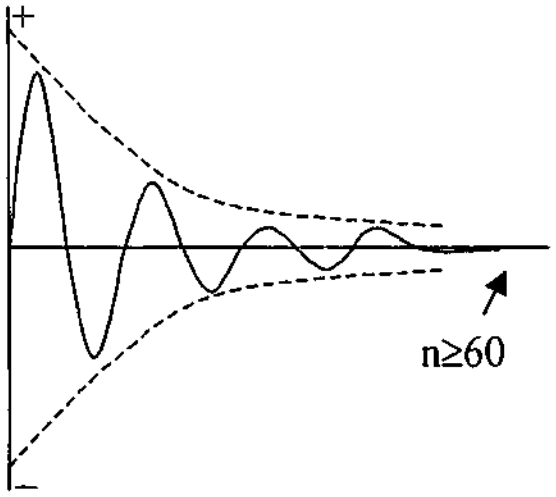

Figure 4.10 Schematic diagram representing the effect of constant 'n' on Equation 4.9.

4.3.2 Calibration of the heat transfer model for ductile iron

In order to apply the heat transfer model to ductile iron, an assumption and a calculation were made. It was assumed that the height (170 mm) of the ductile iron test bar 1 compared to its diameter (70mm) is long enough to consider the test bar as an infinite solid cylinder. The thermal diffusivity is normally calculated from the following Equation:

$$\alpha = \frac{k_t}{\rho . c_p} \tag{4.10}$$

where α is thermal diffusivity (m^2s^{-1}), k_t is thermal conductivity ($W.m^{-1}.K^{-1}$), ρ is density ($kg.m^{-3}$) and c_p ($m^2.s^{-2}.K$) is the specific heat of the material. However, due to the presence of graphite nodules, Equation 4.10 cannot be utilised for ductile iron. For this reason, thermal diffusivity was calculated according to the time at which the simulated cooling curve of the model overlaps the experimental cooling data at the centre of test bar 1 (Figure 4.11).

The cooling curve at the centre of the test bar 1 (achieved from the thermocouple 3 in Figure 3.2) was chosen for calibration of the heat transfer model to satisfy the criteria for application of the model for ductile iron. The criterion for application of the model was that the internal resistance of the body controls the cooling in the material. This criterion was fulfilled at the thickest section size of test bar 1, which was the middle section where thermocouple 3 was located (Figure 3.2).

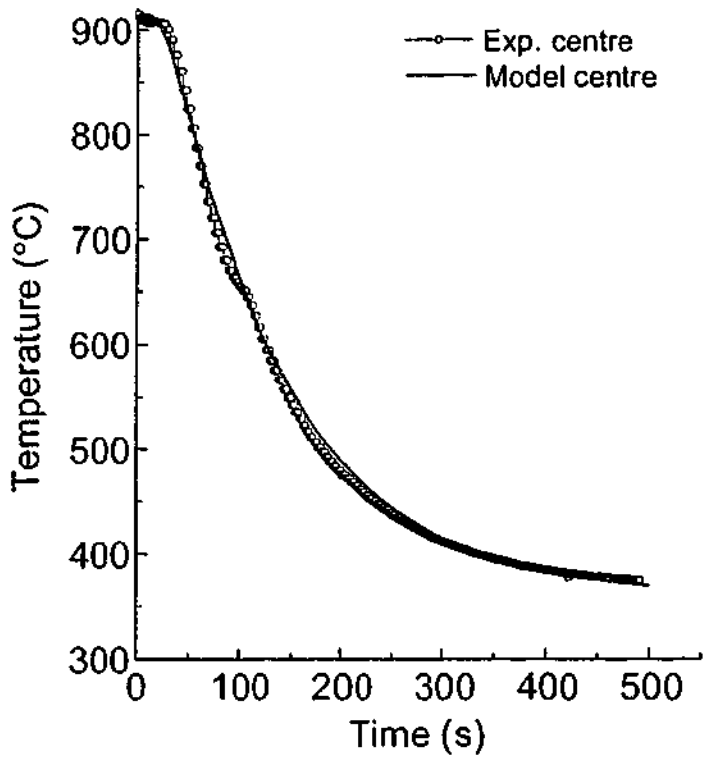

Figure 4.11 Comparison of the experimental and calibrated heat transfer curves at the centre of the test-bar 1

The best fit for thermal diffusivity ($\alpha = 4.96\times10^{-6}$ m^2s^{-1}) was achieved by calculation of Equation 4.9 at the centre of the test bar ($x_c = R_c$) for 500 s with a 5 s stepping time (Figure 4.11). The value 4.96×10^{-6} m^2s^{-1} for the thermal diffusivity of the ductile iron was lower than the thermal diffusivity of steels (~9.6×10^{-6} m^2s^{-1}), which was probably a result of the presence of graphite nodules.

An upper bound estimate of the value for thermal diffusivity in order to confirm the value $\alpha = 4.96\times10^{-6}$ m^2s^{-1} for test bar 1 utilises a simple rule of mixtures. In this estimation, thermal diffusivities corresponding to iron

(assuming that the ferrous matrix of ADI has similar thermal properties to iron) and graphite (nodules) are combined in the equation:

$$\alpha_{ADI} = f.\alpha_{Iron} + (1-f)\,\alpha_{Graphite} \qquad (4.11)$$

where α_{ADI} is diffusivity of the austempered ductile iron, α_{Iron} is diffusivity of iron (which is similar to ADI matrix), $\alpha_{Graphite}$ is diffusivity of graphite, f is volume fraction of matrix and (1-f) is volume fraction of graphite.

The estimated diffusivity for test bar 1 using physical properties (Table 4.3) and Equation 4.11 for 90% iron (matrix that is similar to steels) and 10% graphite was 7.7×10^{-6} m^2s^{-1}. The difference between this value and the value based on experimental data is because effect of porosity was not taken into account for thermal diffusivity of graphite. The porous graphite in ductile iron will result in lower values for both k_t and $\rho.c_p$ compared to the data for the pure material (Table 4.3).

Material	k_t (W m^{-1} °C^{-1})	c_p (J kg^{-1} °C^{-1})	ρ (kg m^{-3})	α (m^2 s^{-1})	*b*
Iron (Fe)	80.3	444	7860	7×10^{-6}	2.8×10^{-8}
Graphite	23.8	712	2250	1.4×10^{-5}	3.8×10^{-7}

Table 4.3 Estimated thermal diffusivity for iron (Fe) and graphite using physical properties (Tottle, 1984) and Equation 4.10.

A similar parameter to α is the contact coefficient *b* (Equation 4.12) that indicates the rate of absorption of thermal energy when a low temperature and a high temperature surface are in contact (Tottle, 1984). Compared to iron (Fe), a large value of *b* corresponding to graphite in Table 4.3 indicates that

the temperature difference between the interior and the surface of the material when heat is added or removed is high, and therefore, graphite decreases the rate of heat transfer in ADI. The relevance of the contact coefficient to this study is only to confirm that graphite decreases the heat transfer in ADI matrix.

$$b = k_t.\rho.c_p \qquad (4.12)$$

The small discrepancy at 100 s and 650°C in the experimental curve in Figure 4.11 was due to recalescence accompanying formation of pearlite in the microstructure during cooling from the austenitising to the austempering temperature, and was not important for calibration of the heat transfer function.

The calibrated heat transfer model was in good agreement with the experimental data at the ¼ thickness (thermocouples 2 and 4 in Figure 3.2). However, the experimental curves associated with thermocouples 1 and 5 at (3 mm) sub-surface had some discrepancies with model data (Figure 4.12). The difference between the experimental and the predicted cooling curves (in sub-surface) results from the fact that the locations of the thermocouples 1 and 5 did not satisfy the requirements for the heat transfer model. This result is in conflict with criteria for application of the heat transfer model (Equation 4.9) in two areas.

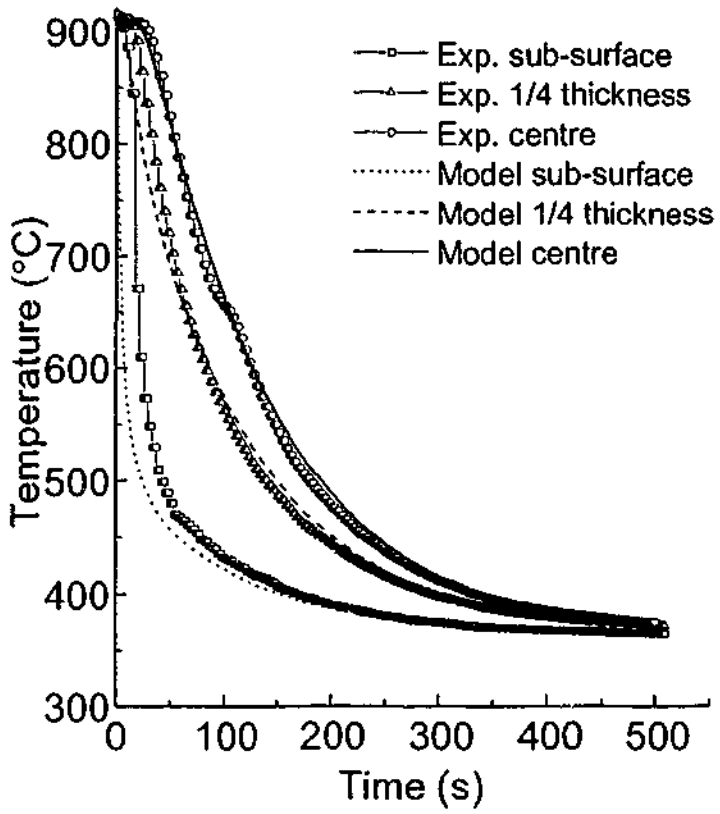

Figure 4.12 Comparison of the experimental and simulated cooling curves associated with iron 1 test bar

First, the thermocouples 1 and 5 were located at the edge of the test bar 1 (Figure 3.2) and therefore, their reported temperature did not satisfy the assumption that heat transfer occurs within an 'infinite' solid cylinder. Second, thermocouples 1 and 5 were located at sub-surface of test bar 1 at which heat transfer was not controlled by internal resistance of the material due to a thin (3 mm) section size. However, the difference between the ideal and the experimental cooling curves at the sub-surface of the test bar 1 was not significant for the austemperability model due to the fact that pearlite formation is always expected at much larger (ie: >10mm) section sizes than at the sub-surface of the material.

The calibrated heat transfer model was utilised to find the point at which the cooling curve touches the pearlite curve at the centre of the test bar. The pearlite curve was predicted according to the program freely available from the MAP web site (Materials Algorithm Project Program Library, 1999a). This program calculates the TTT diagram corresponding to carbon and other alloying elements in steels. However, ADI has a heavily segregated microstructure compared to steel. To accommodate this difference, a boundary condition was defined in the program to take into account segregation by means of the location at which pearlite starts to form at first in the microstructure.

The study of segregation in ADI suggests that Si (ferrite stabiliser) segregates around graphite nodules (Nazarboland & Elliott, 1997b). Therefore, austenite starts to transform to transformation products (ie: ausferrite or pearlite) around graphite nodules prior to any other place such as intercellular areas in the matrix of ADI (Bahmani & Elliott, 1994). Austenite transforms to pearlite instead of ferrite at high (> 500°C) temperatures due to its high carbon (1.2%) concentration in ADI matrix. This means that composition of the matrix around graphite nodules is to be the input of the TTT diagram program to identify the onset of austenite transformation to pearlite in ADI matrix.

However, there is no comprehensive model yet available for prediction of the alloying element compositions adjacent to graphite nodules. For this

reason, Si (as the strongest austenite de-stabiliser or ferrite former) was considered to be the input of the program for prediction of the pearlite curve for an Fe-C-Si alloy around graphite nodules. The value for Si was considered the same as that reported in chemical analysis of the ductile iron. Austenite carbon concentration was estimated around graphite nodules utilising Equation 4.2 with Si and austenitising temperature as its inputs.

In order to predict austemperability, Equation 4.9 was calculated at the centre of the test bar in which $x_c = R_c$. Therefore, austemperability of the ADI was estimated as following:

$$\frac{T_p - T_A}{T_\gamma - T_A} = \frac{4}{\pi}\sum_{n=0}^{\infty} \frac{(-1)^n}{2n+1}\exp\left[\frac{-(2n+1)^2\pi^2}{4}\frac{\alpha t_p}{(R_{cmax})^2}\right]\cos\frac{(2n+1)\pi}{2} \qquad (4.11)$$

where T_p is the temperature at the tip of the pearlite curve (°C), T_γ is the austenitising temperature (°C), T_A is austempering temperature (°C), R_{cmax} is austemperability (m), t_p is the time corresponding to the tip of the pearlite curve (s), α is thermal diffusivity of ductile iron (m^2s^{-1}) and n is a constant (n=60).

Austemperability was computed utilising Equation 4.11 with T_A, T_γ and Si composition as inputs (Figure 4.13). The carbon concentration in the matrix (X_c) was estimated from Equation 4.2 and t_p and T_p were computed from the TTT diagram program (Materials Algorithm Project Program Library, 1999a) (Figure 4.13). In order to compute the R_{cmax}, Equation 4.11 was divided into

two parts, Sigma and Ratio (Figure 4.13). The value for R_c that was computed with 10^{-7} mm steps was reported as R_{cmax} (austemperability) when Sigma was equal to "Ratio" (Figure 4.13). A value of 10^{-7} was chosen to minimise the difference between the Sigma and Ratio values in the program, which led to the lowest error for austemperability (Figure 4.13).

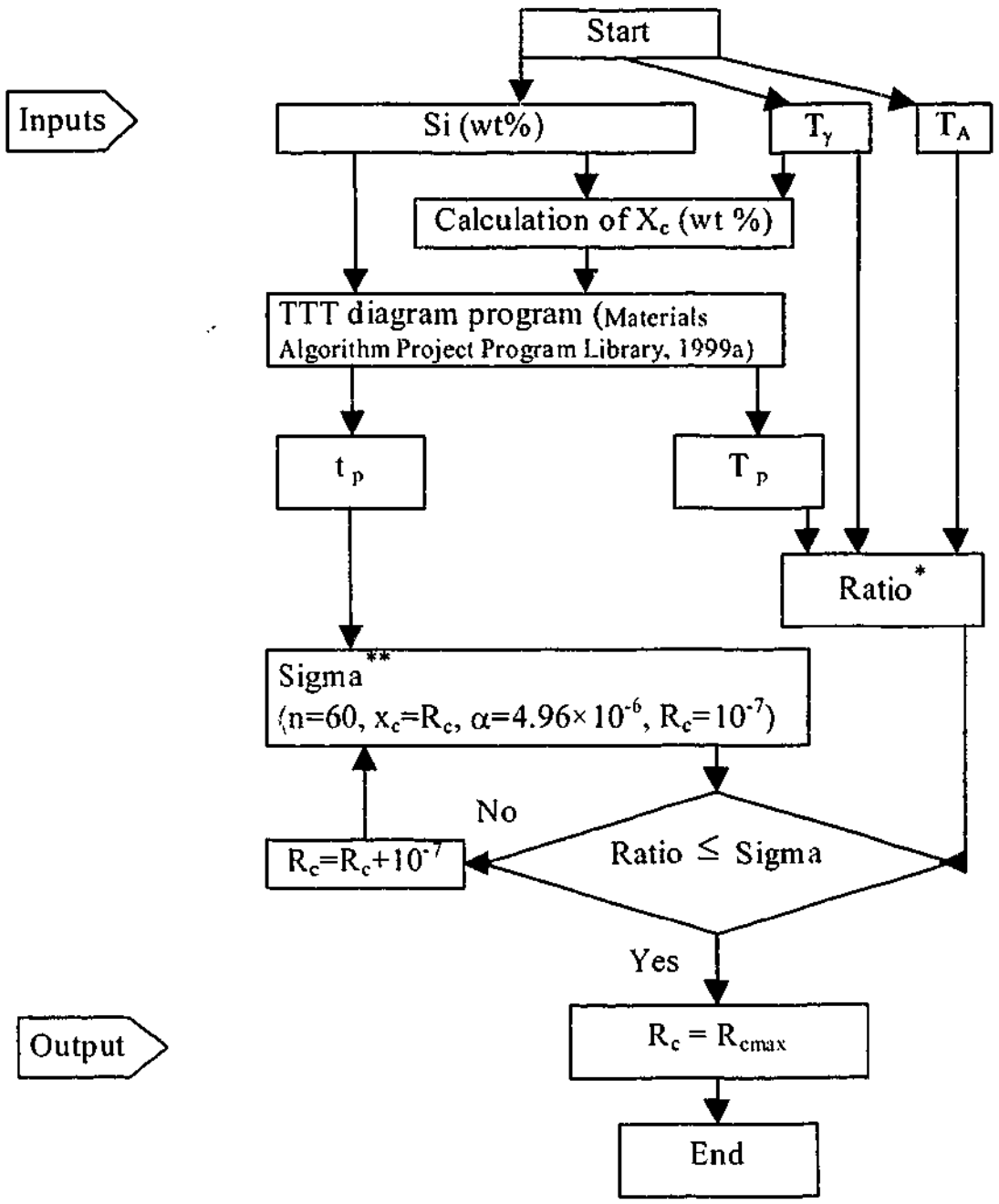

$$*\text{Ratio} = \frac{T_p - T_A}{T_\gamma - T_A}$$

$$**\text{Sigma} = \frac{4}{\pi}\sum_{n=0}^{\infty}\frac{(-1)^n}{2n+1}\exp\left[\frac{-(2n+1)^2\pi^2}{4}\frac{\alpha t_p}{R_c^{\,2}}\right]\cos\frac{(2n+1)\pi}{2}\frac{x_c}{R_c}$$

Figure 4.13 Flowchart of the program for calculation of the austemperability of the ADI in respect to TTT diagram program developed by Bhadeshia (Materials Algorithm Project Program Library, 1999a).

4.4 The processing-austemperability window

In order to obtain a more informative diagram for the processing design of ADI the model for estimation of the processing window boundaries and the program for prediction of the austemperability were merged. The new program took alloying elements, austenitising temperature and austempering temperature as input parameters and calculated the time for lower and upper boundaries of the austempering window and corresponding austemperability for ductile iron.

Execution of the program for a range of austempering temperatures (eg. 285-400°C) leads to a three-dimensional diagram (processing-austemperability window) in which a plane represents the optimum time and temperature to achieve ASTM standard with maximum austemperability for ADI (Figure 4.14). The processing-austemperability window represents a plane instead of a volume due to the fact that austemperability is a limit (maximum diameter of the ductile iron test bar that can be austempered without formation of pearlite in the matrix) that does not change with austempering time.

Similar to the processing window, a change in alloying elements and austenitising temperature changes the three-dimensional processing-austemperability window plane. Therefore, for a range of alloying elements and austenitising temperatures a volume is expected corresponding to the processing-austemperability window in which every spot satisfies the

minimum requirements of the ASTM standard defined for ADI. Further details of the processing-austemperability window are explained in the discussion chapter (chapter 6).

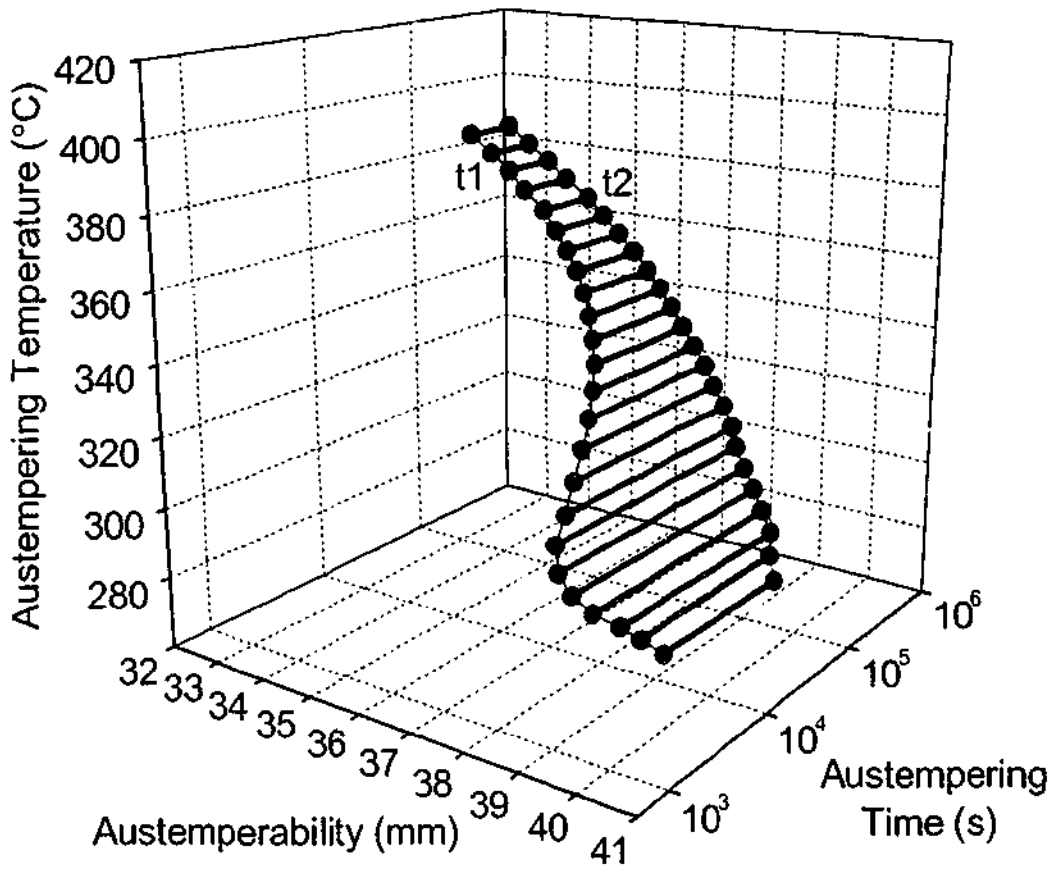

Figure 4.14 A three-dimensional diagram of the processing-austemperability window (hatched area) computed for an iron of composition (wt-%) Fe, 3.3C, 2.4Si, 0.39Mn, 0.25Cu, 0.24Mo and 0.04Mg at 910°C austenitising temperature; t_1: the beginning of the processing-austemperability window and t_2: the end of the processing-austemperability window

4.5 Summary

Two models were developed: one to estimate the processing window boundaries and the other. the austemperability of ADI. In order to estimate the processing window boundaries a model for isothermal transformation of austenite to carbide free bainite and experimental data sourced from literature were utilised. The calibrated model is to be examined for an ADI of unknown processing window in which the optimum proportion of the microstructural constituents (martensite and HCA) is expected to fulfill the criteria for the processing window boundaries and satisfy the ASTM standard for mechanical properties of ADI.

The model for austemperability of ADI computes the maximum radius of the ductile iron test bar in which the cooling curve at the centre of the test bar touches the tip of the simulated pearlite curve of the iron. The heat transfer function for simulation of the cooling curve at the centre of the test bar was calibrated according to the experimental cooling curves of the test bar 1. Therefore, the calibrated model needs to be examined for austemperability of an unknown ductile iron test bar.

CHAPTER 5

Application of the Model

5.1 Introduction

In this chapter the experimental results and discussions corresponding to evaluation of the processing window and austemperability models are presented. Section 5.2 describes a comparison between the experimental and the predicted results corresponding to the processing window of test bar 2. In this section, the predicted time for the lower boundary of the processing window of test bar 2 is validated by determination of the volume fraction of martensite. The predicted time for the upper boundary of the test bar 2 processing window is evaluated by measurement of the volume fraction of HCA.

Section 5.3 explains the approach to validate the model for austemperability by comparing the experimental results and model data associated with test bar 1. The final section presents the results for simultaneous prediction of the processing window and austemperability (processing-austemperability window). Test bar 2 mechanical properties are investigated within its predicted processing-austempering window boundaries and compared with ASTM A897M:1990 standard.

5.2 Processing window

In order to validate the model for estimation of the processing window boundaries, the time associated with the lower (t_1) and upper (t_2) boundaries of the processing window of test bar 2 were computed (Figure 4.8) for the austempering range of 285-400°C with a 5°C increment (Figure 5.1). The austenitising temperature was chosen as 905°C.

The volume fraction of martensite was determined experimentally (using metallography and image analysis) with respect to the isothermal holding time predicted by the model for the lower boundary of the processing window. The measured volume fraction of martensite was compared with the 3% value that is the expected limit defined for the lower boundary of the austempering window.

The difference between the predicted holding time for upper boundary of the austempering window and the time at which the maximum volume fraction of HCA declines by 10% was utilised to validate the outcome of the model for prediction of the time t_2. The volume fraction of HCA was determined (using X-ray analysis) for a series of austempering times and normalised according to the maximum value achieved at a particular austempering temperature.

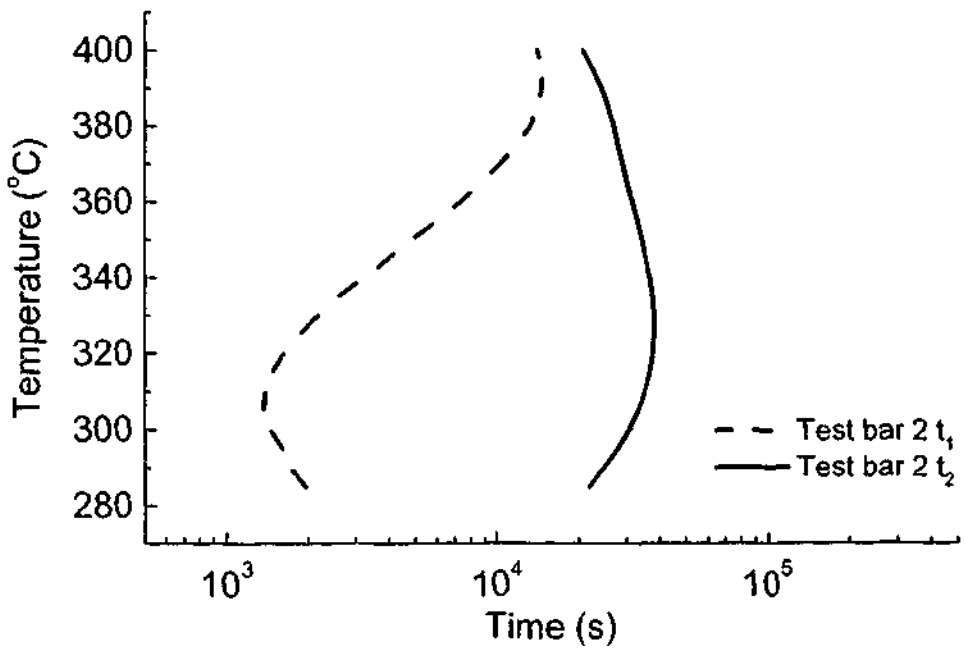

Figure 5.1 Predicted processing window of test bar 2

5.2.1 Results

The as-cast microstructure of test bar 2 was a typical "bull's eye" (Davis, 1996), consisting of graphite nodules surrounded by ferrite with a pearlite matrix (Figure 5.2). Nodule count and nodularity for the test bar were

120 (nodule mm^{-2}) and 95%, respectively, in agreement with expected values for commercial as-cast microstructure of ADI products.

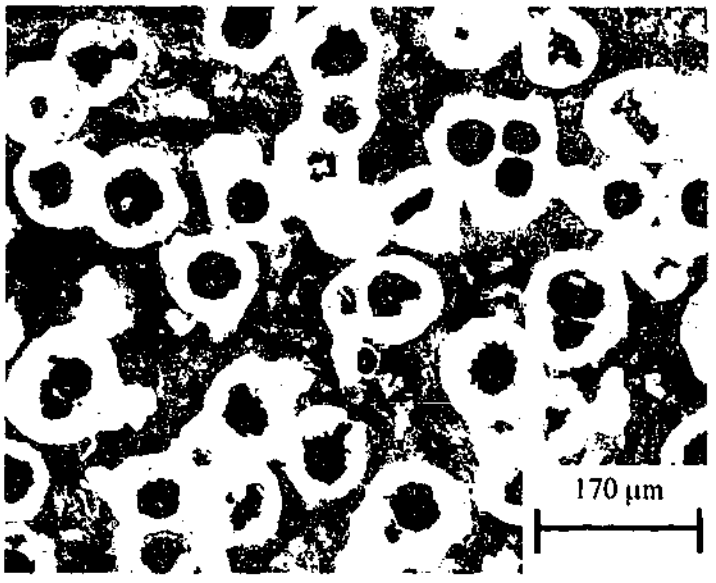

Figure 5.2 As-cast microstructure of test bar 2 (etched in nital 2%)

5.2.2 Validation of the predicted lower boundary of the processing window

Quantitative computer aided image analysis was utilised to determine the volume fraction of martensite corresponding to the lower boundary of test bar 2. The value for volume fraction of martensite was higher than 3% (that was chosen for definition of t_1 in the model) at all austempering temperatures (Figure 5.3). The largest difference between the expected and the experimental values for volume fraction of martensite was at 380°C and the smallest difference at 340°C.

In order to evaluate the predicted austempering time at the lower boundary of the processing window, the time for the volume fraction of

martensite to reach 3% was back-calculated according to the time corresponding to the experimental values at 300, 340 and 380°C (Figure 5.3). This was due to the fact that determination of the time at which exactly 3% martensite occurs in the matrix was almost impossible due to limitations in achieving a consistent colour contrast for detection of martensite using the heat tint etching technique.

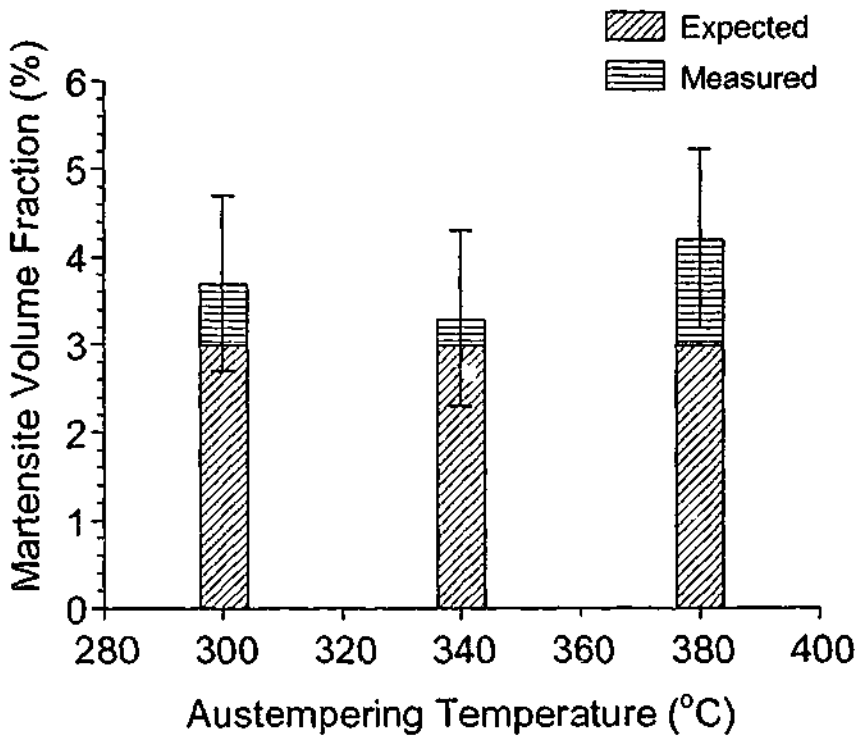

Figure 5.3 Comparison of the volume fraction of martensite achieved experimentally in test bar 2 for the predicted austempering time at t_l and the expected volume fraction of martensite at t_l (Errors are those associated with image analysis technique)

Figure 5.4 reveals that the model and the back-calculated (expected) times were in good agreement at all austempering temperatures. The difference between the expected and the model values at t_l were 15, 10 and 20 percent at 300, 340 and 380°C respectively.

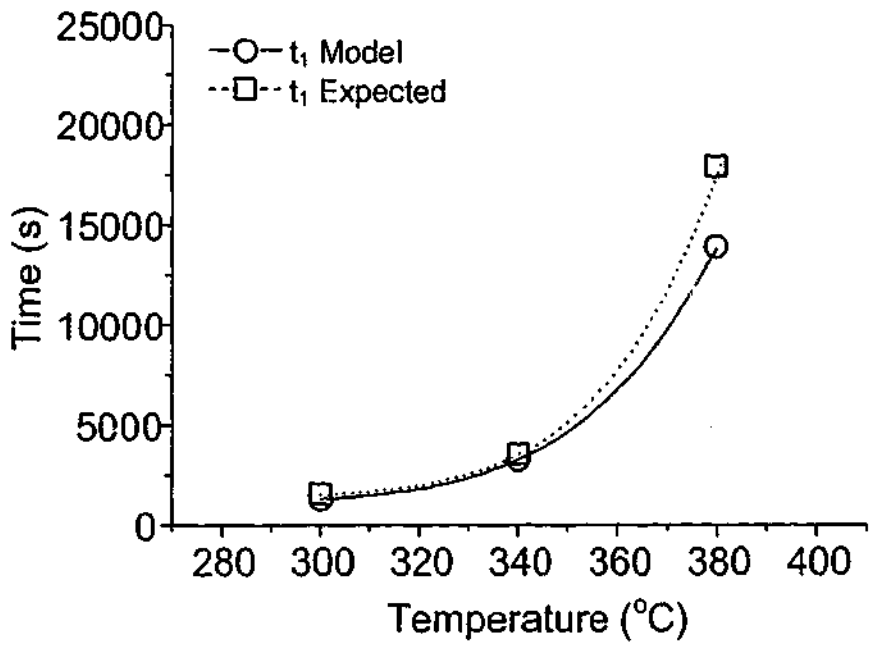

Figure 5.4 Comparison of the expected and predicted times for the lower limit of the test bar 2 processing window

5.2.3 Validation of the predicted upper boundary of the processing window

In order to validate the estimated holding time for the upper limit of the test bar 2 processing window, two issues were studied. Firstly, to find out if the maximum amount of HCA was decreased by 10% (90% of HCA available in the matrix) in the microstructure of test bar 2 at the predicted austempering time t_2. Secondly, to determine the time difference between the estimated t_2 and the time at which the maximum volume fraction of HCA declined by 10% in the test bar 2 matrix.

To identify the time at which HCA reached its maximum value and the time when 90% of HCA was presented in the matrix of test bar 2, the volume

fraction of HCA was measured using x-ray analysis of the samples austempered at 300, 340 and 380°C (Figure 5.5). The results showed that the volume fraction of HCA increased with austempering time, reaching a peak and then declining at all austempering temperatures (Figure 5.5). The highest volume fraction of HCA at 300, 340 and 380°C were 17, 25 and 34 percent respectively.

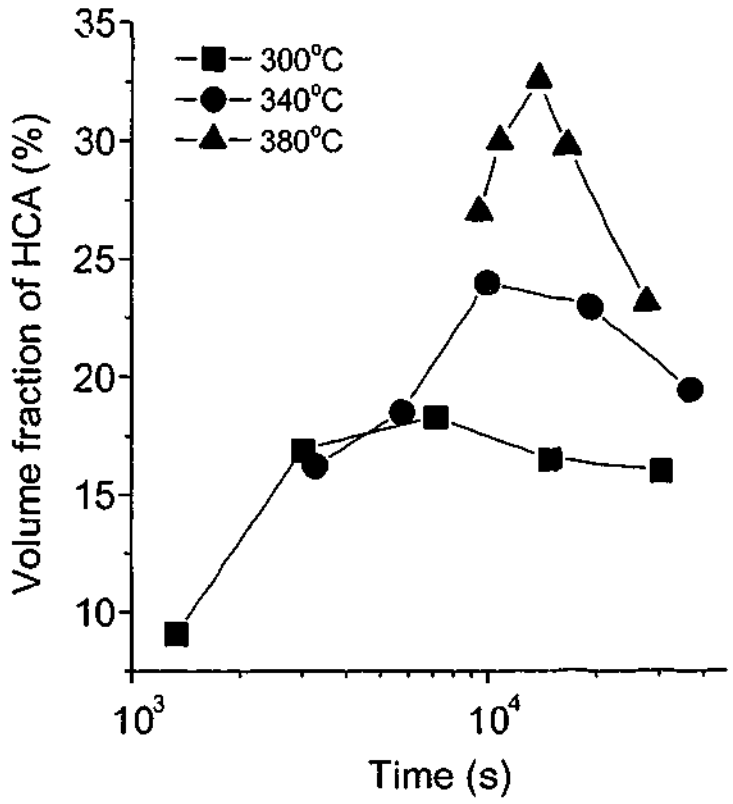

Figure 5.5 Variation of the volume fraction of HCA with austempering time corresponding to test bar 2 at 300, 340 and 380°C austempering temperatures.

The volume fraction of HCA corresponding to austempering times 30532, 36901 and 27809 s (8.5, 10.3 and 7.7 hours) predicted for t_2 of the test bar 2 were normalised according to the maximum volume fraction of HCA achieved at 300, 340 and 380°C respectively. The results showed that the

normalised volume fraction of HCA was less than 90% at all chosen austempering temperatures (Figure 5.6). The difference between the measured and the expected value of HCA increased from 3 to 19 percent with an increase in austempering temperature from 300 to 380°C.

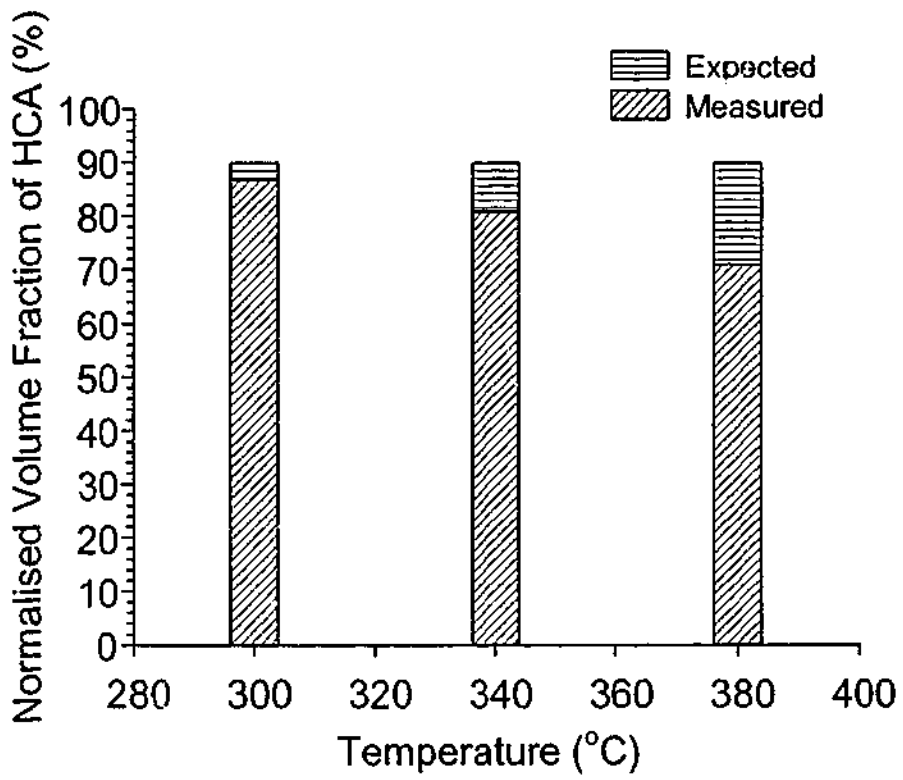

Figure 5.6 A comparison between the normalised volume fraction of HCA at 300, 340 and 380°C austempering temperatures compared with the expected (90%) volume fraction of HCA at t_2.

To find out the difference between the expected time and the model time for t_2 of test bar 2, the expected austempering time associated with the 90% of the maximum amount of HCA was calculated using experimental results and curve fitting (Figure 5.7). The fitting functions of HCA at 300, 340 and 380°C austempering temperatures (Table 5.1) do not exactly fit the experimental data (Figure 5.7). However, the difference between the fitting

curves and measured HCA values was small (<2%) at all austempering temperatures.

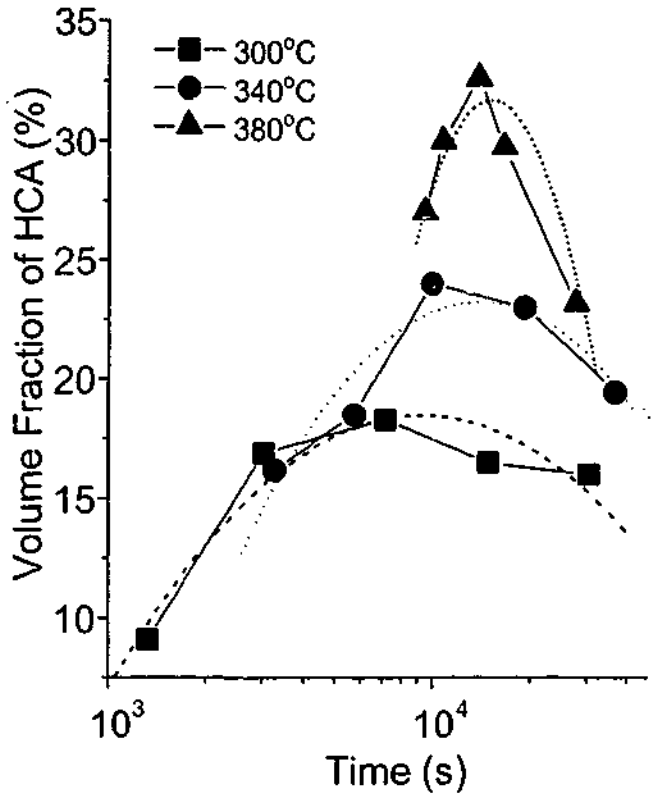

Figure 5.7 The fitting curves obtained from the variation of HCA with austempering time at 300, 340 and 380°C

Austempering Temperature (°C)	Fitting Function
300	V_{HCA}= -173.6 + 96.8 t - 12.2 t^2
340	V_{HCA}= -313.8 + 162.7 t - 19.6 t^2
380	V_{HCA}= -1865.2 + 910.6 t - 109.3 t^2

Table 5.1 Fitting functions representing variation of volume fraction of HCA with austempering time at 300, 340 and 380°C.

The time for HCA to transform to (bainitic) ferrite and carbide (stage II reaction) was decreased with an increase in austempering temperature from 300 to 380°C (Figure 5.7). This was due to that fact that the energy barrier that

must be overcome in order to carry out the stage II reaction (activation energy) was lower at 380°C compared to 300°C (Campos-Cambranis et al., 1998). The times at which 90% of HCA is present in the matrix of test bar 2 were 23700, 30830 and 21600 s (6.6, 8.5 and 6 hours), corresponding to 300, 340 and 380°C austempering temperatures (Figure 5.7).

A comparison between the expected and model values for the time corresponding to the upper boundary of test bar 2 showed that the model overestimates the austempering time at all austempering temperatures (Figure 5.8). The time difference between the model and the expected t_2 were 25, 20 and 25 percent at 300, 340 and 380°C respectively. This overestimation was larger than the results for the lower boundary of the processing window (Table 5.2).

T_A (°C)	Austempering time difference at t_1 (%)	Austempering time difference at t_2 (%)	Time difference for t_2 (%) (Austempering time difference at t_1 excluded)
300	15	25	10
340	10	20	10
380	20	25	5

Table 5.2 Time difference between the model and expected values for the predicted processing window of test bar 2.

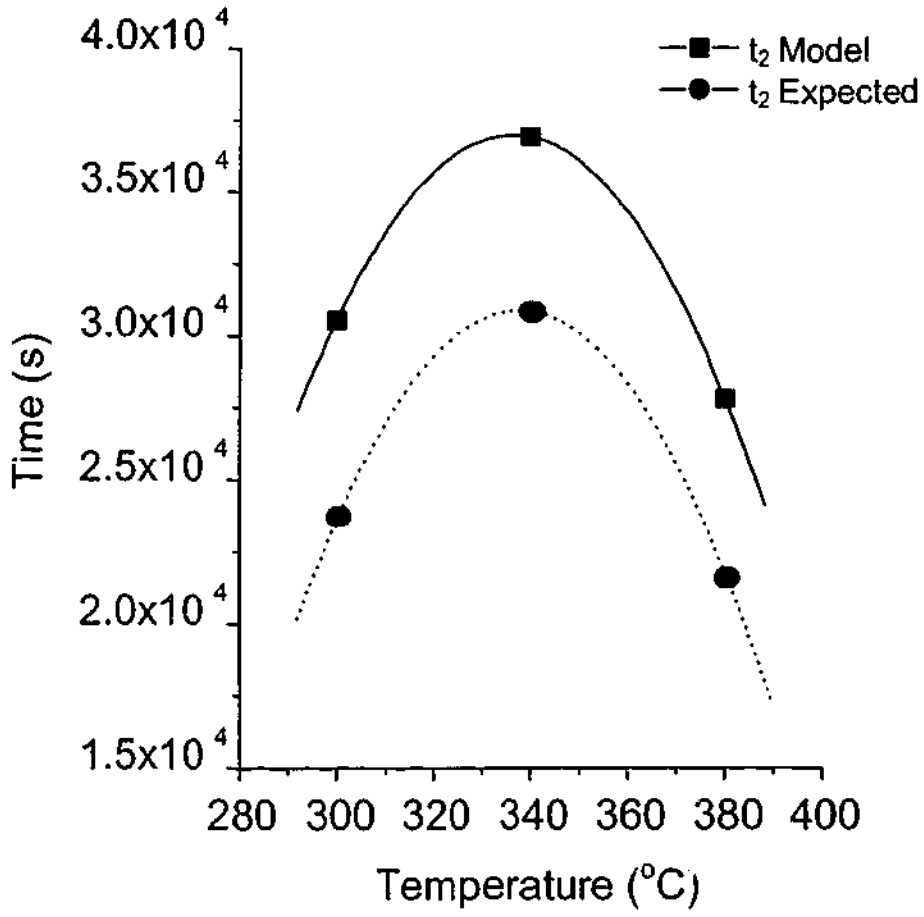

Figure 5.8 Comparison of the expected and model values for austempering times corresponding to the upper limit of the test bar 2 processing window at 300, 340 and 380°C.

5.2.4 Discussion

5.2.4.1 The lower boundary of the processing window

The volume fraction of martensite at the lower boundary of the test bar 2 austempering window is higher than the expected (3%) value at all austempering temperatures (Figure 5.3). This means that the model underestimates the time for the start of the test bar 2 processing window that is confirmed in Figure 5.4. However, errors associated with the computer aided

image analysis and fitting function of β (Equation 4.5) can easily account for this time underestimation.

The errors associated with the image analysis technique corresponding to experimental results of the irons 1, 2, 3 are not available from the literature (Elliott, 1997) to compare the accuracy of the test bar 2 experimental data. However, the colour contrast achieved using the heat tint etching technique (Chapter 3) and image analysis may introduce up to 1% error in martensite volume fraction measurement at t_1 (Figure 5.3).

The effect of the β function on the time for isothermal transformation is shown in Figure 4.6 in which the predicted curves do not exactly overlap the calibration experimental data. Therefore, the same error is expected for the predicted lower boundary of the test bar 2 processing window. A large discrepancy between the calibration data and experimental data corresponding to irons 1, 2 and 3 at high austempering temperatu :s (Figure 4.1) leads to an increase in the difference between the expected and the model time at 380°C. This difference is associated with the regression function β and can be improved by increasing the number of the experimental data for calibration of the function. For instance, instead of 12 data points corresponding to irons 1, 2 and 3 (Figure 4.1), 24 or more data points would present a better fitting function and hence, a better predicted result for t_1.

Overall, the experimental results of test bar 2 are in reasonable agreement with the predicted austempering time at the lower boundary of the austempering window of test bar 2. This outcome confirms that the calibrated bainite transformation model according to experimental data for ADI can be utilised for estimation of the lower boundary of the processing window (Chapter 4).

5.2.4.2 The upper boundary of the processing window

The difference between the predicted and expected values for t_2 is because of three issues. Firstly, the time interval Δt is calculated from a logarithm function (Equation 4.6) that always requires a positive value. For this reason, the negative values of Δt corresponding to irons 2 and 3 (Figure 4.7) were eliminated for the calculation of Δt function.

The impact of this elimination of the negative Δt data (Figure 4.9) is not significant for the predicted upper limit of the processing window because data points beyond the closing point of the processing window are not used for heat treatment. However, this limitation leads to departure of the predicted t_2 values from experimental and a slight overestimation in closure of the processing window (Figures 4.9b and 4.9c).

Secondly, a small number of data points for calculation of the Δt function (9 experimental points out of a possible 12 in Figure 4.1) limits the

accuracy of the multiple linear regression function of Δt, especially at the points close to the closure of the processing window. This may be improved by using more experimental data for calibration of the Δt function.

Finally, t_2 is computed by addition of the Δt function to the values computed for t_1 (Figure 4.7), hence, the computed value includes the error associated with the lower boundary of the processing window. For this reason, the error corresponding to t_1 must be subtracted from the time difference between the model and expected values at t_2. This decreases the error to 10, 10 and 5 percent at 300, 340 and 380°C respectively (Table 5.1), which is a reasonable difference between the model and expected results for upper boundary of the processing window.

5.3 Austemperability

The austemperability was computed according to the point at which a simulated cooling (quenching) curve at the centre of the test bar touches the pearlite curve of the TTT diagram (Chapter 4). In order to validate the model, the predicted austemperability was compared with microstructural observations that revealed the location at which pearlite started to form in test bar 1 during cooling from the austenitising (910°C) to the austempering temperature (360°C).

5.3.1 Results

The as-cast microstructure of test bar 1 was a typical "bull's eye" (Davis, 1996), consisting of graphite nodules surrounded by ferrite with a pearlite matrix (Figure 5.9). Nodule count and nodularity for the test bar were 120 (nodule mm^{-2}) and 95%, respectively and were within the acceptable range for ADI products.

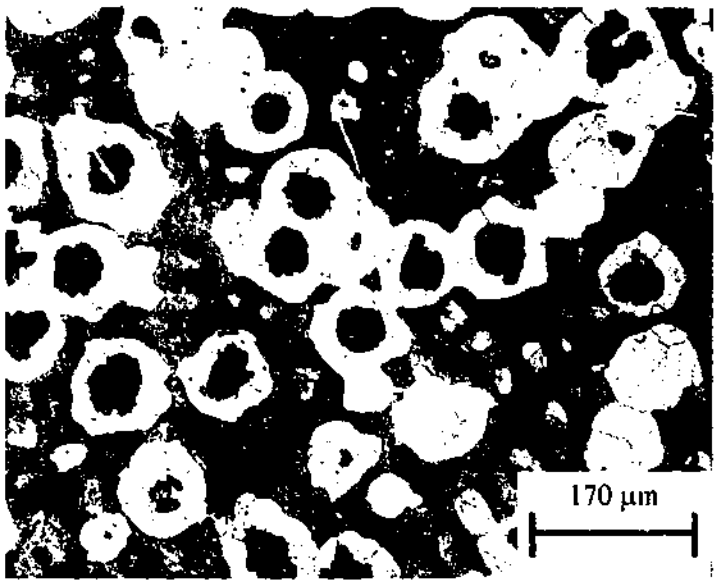

Figure 5.9 As-cast microstructure of test bar 1 (etched in 2% nital)

The experimental cooling curves at ¼ thickness (19 mm from the surface) touched pearlite curve of test bar 1 (Figure 5.10). The cooling curves at the centre (38 mm from the surface) crossed the predicted pearlite curve of the test bar (Figure 5.10). Therefore, pearlite formation was expected at ¼ thickness and centre of the test bar 1. This outcome was confirmed using metallography (Figure 5.11) and microhardness measurements.

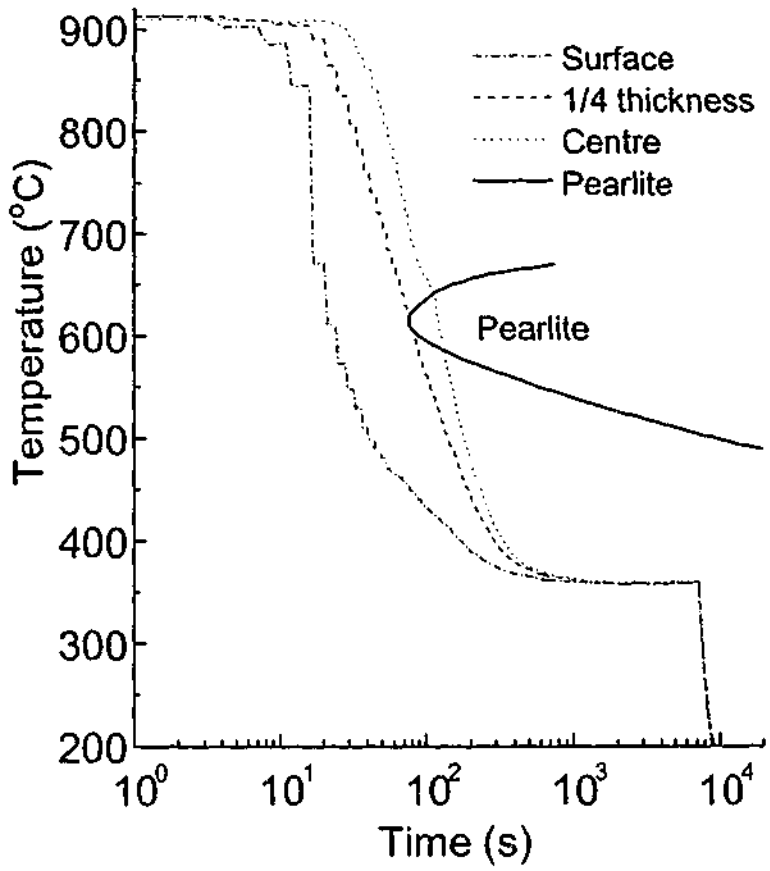

Figure 5.10 Experimental cooling curves and simulated pearlite curve corresponding to test bar 1 (pearlite curve for the TTT diagram was computed using the program freely available from the Materials Algorithm Project Program Library (1999a)).

The matrix 5mm from the surface of test bar 1 consisted of ausferrite and graphite nodules (Figure 5.11a) with microhardness of ausferrite 381 BHN. Pearlite started to appear around graphite nodules at 19 mm distance from the surface of the test bar (Figure 5.11b). The volume fraction of pearlite increased with an increase in the distance from the surface, reaching to its maximum at the centre of the bar (Figure 5.11c). Microhardness of pearlite was 251 BHN, lower than ausferrite at 381 BHN.

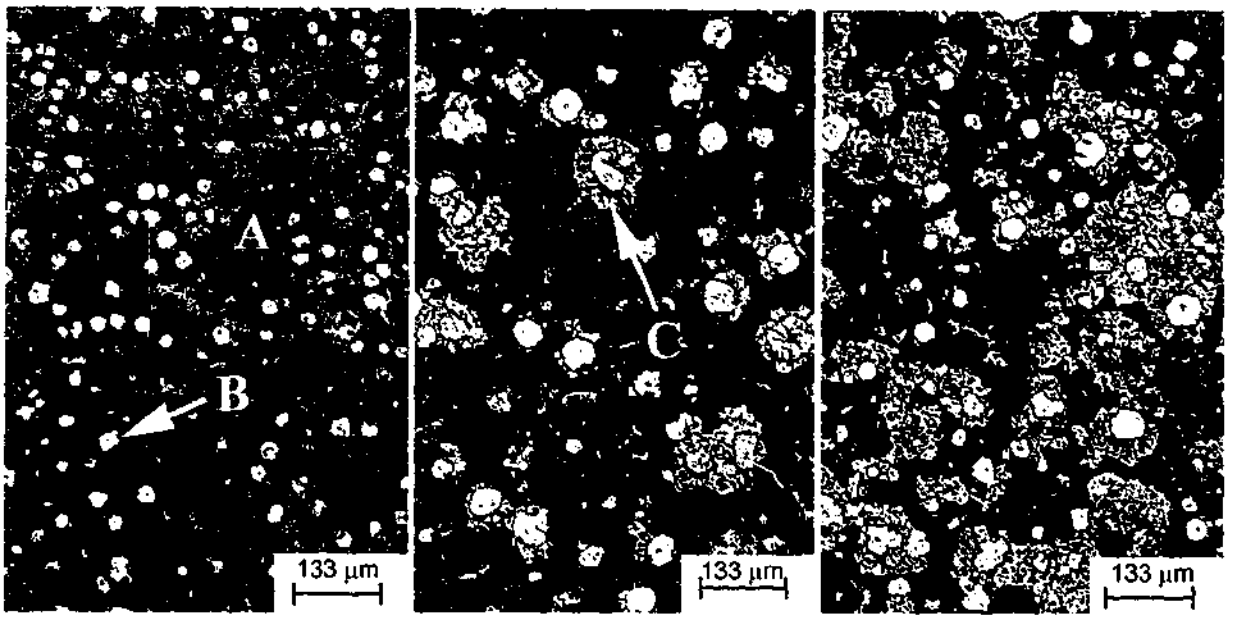

(a) (b) (c)

Figure 5.11 Microstructure at (a) sub-surface (5 mm), (b) 1/4 thickness (19 mm) and (c) centre (38 mm) distance from the surface of test bar 1 (Microstructural constituents: ausferrite (A), graphite nodules (B) and pearlite(C)).

The outcome of the austemperability program (Figure 4.13) predicted the onset of pearlite formation at 16.2 mm from the surface of the test bar 1. A micrograph of the test bar at 16 mm distance from surface of the test bar (close to the point at which pearlite starts to form) showed no pearlite formation (Figure 5.12) in the matrix.

Figure 5.12 Micrograph corresponding to 16 mm distance from the surface of test bar 1.

5.3.2 Discussion

The austemperability program successfully predicts the maximum radius at which no pearlite is present in test bar 1 (Figure 5.12). This shows that the pearlite curve of the TTT diagram is predicted accurately due to the assumption that Si (as the most important ferrite stabiliser in the ADI matrix) and carbon are the most important elements in estimation of the pearlite curve. Incorporation of other alloying elements (Cu, Ni, Mn and Mo) to the estimation of the pearlite curve results in a delay in time for pearlite formation (Figure 5.13) and consequently over-estimation of the austemperability.

For instance, the estimated austemperability increases from 16.2 mm to 36 mm if all the alloying elements (reported in chemical analysis) of test bar 1 are used for calculation of the austemperability. However, at 36 mm from the

surface of test bar 1 pearlite is already formed (Figures 5.11a and 5.11b), confirming that austemperability is overestimated.

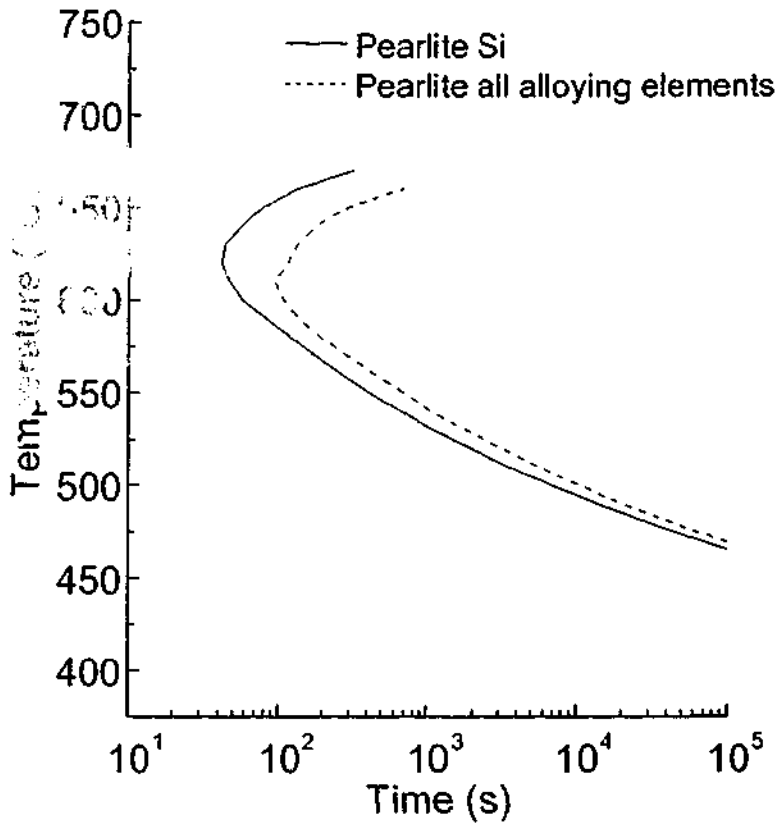

Figure 5.13 Comparison of the predicted pearlite curve according to Si and C content and pearlite curve computed from all alloying elements of test bar 1 (Table 3.1).

Disadvantage of the CCT diagram compared to TTT diagram to the model for austemperability is that the pearlite curve of the CCT diagram is always associated with longer times for a particular alloy composition. Therefore, it could be anticipated that pearlite curve of the CCT diagram, due to a slower cooling rate, leads to a longer time associated with the tip of the pearlite curve and over-estimation of the austemperability for test bar 1. However, the CCT diagram information is more realistic for prediction of the

austemperability if composition profile (segregation) of alloying elements were available around graphite nodules. Further study needs to be done to estimate alloying elements concentration around graphite nodules.

Successful prediction of the maximum size of test bar 1 (that can be austempered) confirms that the model for heat transfer is calibrated correctly for prediction of the cooling curve associated with the tip of the pearlite curve of the TTT diagram. The calibrated heat transfer model is examined utilising test bar 2 specimens in the following section.

5.4 Processing - austemperability window

The model for prediction of the processing-austemperability window was validated according to test bar 2 composition. The processing-austemperability window was predicted for the austempering range of 285-400°C with a 5°C increment for 905°C austenitising temperature (Appendix III). Three austempering temperatures (300, 340 and 380°C) were chosen for microstructure and mechanical properties investigations (Figure 5.14).

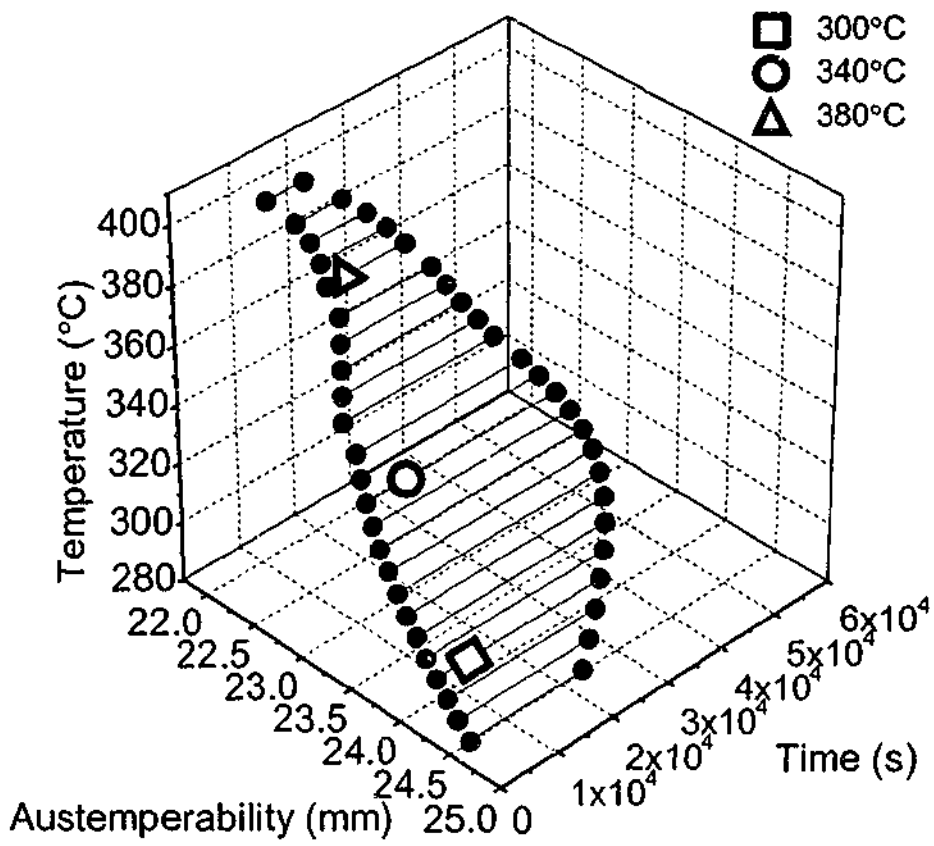

Figure 5.14 Experimental points chosen within the processing-austemperability window of test bar 2 at 300, 340 and 380°C austempering temperatures (for a better presentation of the experimental points within the processing-austemperability window the time axis is chosen linear).

A range of austempering times could be selected within the predicted processing-austemperability window of test bar 2 to investigate mechanical properties. However, austempering times presented in table 5.3 were selected for validation of the model to achieve maximum ductility for a minimum austempering time. The maximum ductility associated with the chosen austempering times (Table 5.2) was provided by the highest volume fraction of HCA in the matrix (Figure 5.5). The minimum austempering time was

chosen because it results in time and energy savings corresponding to the austempering process.

T_A (°C)	t_A (s)	R_{cmax} (mm)
300	7168	24.3
340	10002	23.5
380	16727	22.5

Table 5.3 Austempering time and austemperability of test bar 2 corresponding to austempering temperatures 300, 340 and 380°C chosen within the predicted processing-austemperability window of test bar 2.

5.4.1 Results

In order to validate the predicted austemperability (Table 5.3), tensile and impact test specimens of test bar 2 were quenched from the austenitising temperature (905°C), according to predicted cooling curves, to 300, 340 and 380°C (Figure 5.15). This was achieved utilising the set up in Figure 3.3. Each sample (connected to a thermocouple) was quenched in front of an air blower in which air speed was controlled using a variac in such a way that cooling curve of the sample followed the simulated cooling curve for austemperability (Figure 3.3). Specimens were rapidly moved to the austempering salt bath when their temperature reached the austempering temperature (Figure 3.3).

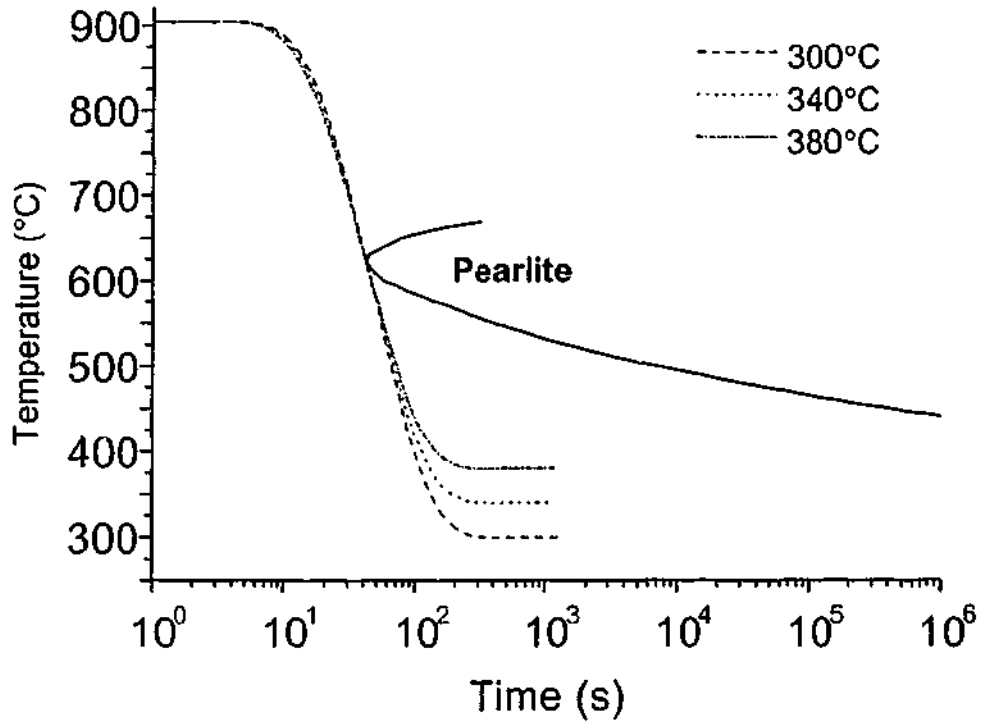

Figure 5.15 Simulated cooling curves from austenitising (905°C) to austempering temperatures at 300, 340 and 380°C corresponding to test bar 2

The experimental cooling curves corresponding to tensile and impact specimens followed the predicted curves corresponding to all austempering temperatures and did not intersect the nose of the simulated pearlite curve (Figures 5.16 and 5.17). This indicates that no pearlite was expected in the microstructures of the specimens. Microstructural observations confirmed that pearlite was not formed in either tensile or impact specimens (Figures 5.18 and 5.19).

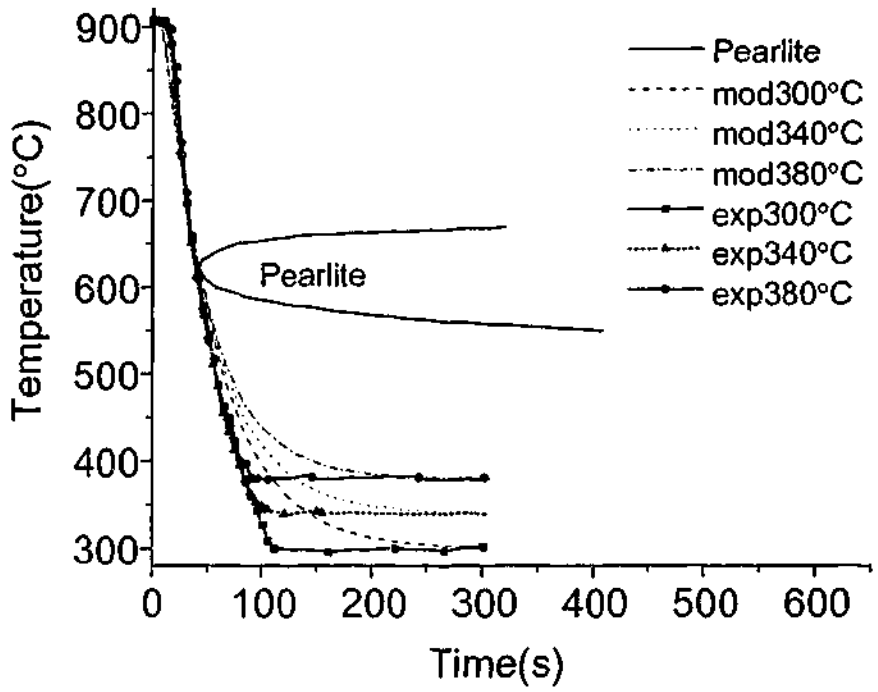

Figure 5.16 Comparison of the experimental and simulated cooling curves from austenitising to austempering temperature corresponding to test bar 2 tensile test specimens.

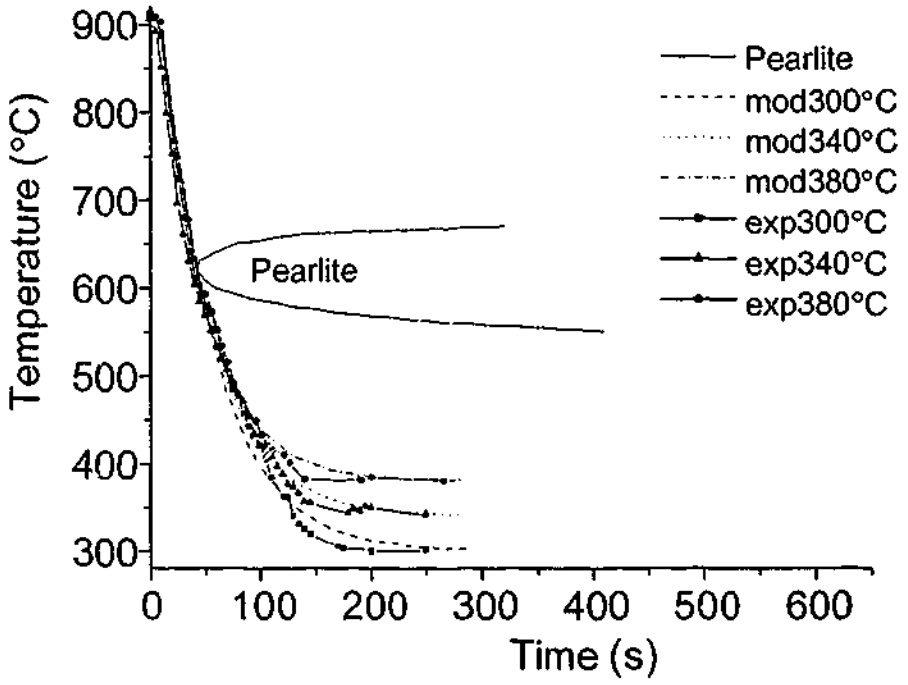

Figure 5.17 Comparison of the experimental and simulated cooling curves from austenitising to austempering temperature corresponding to test bar 2 impact test specimens.

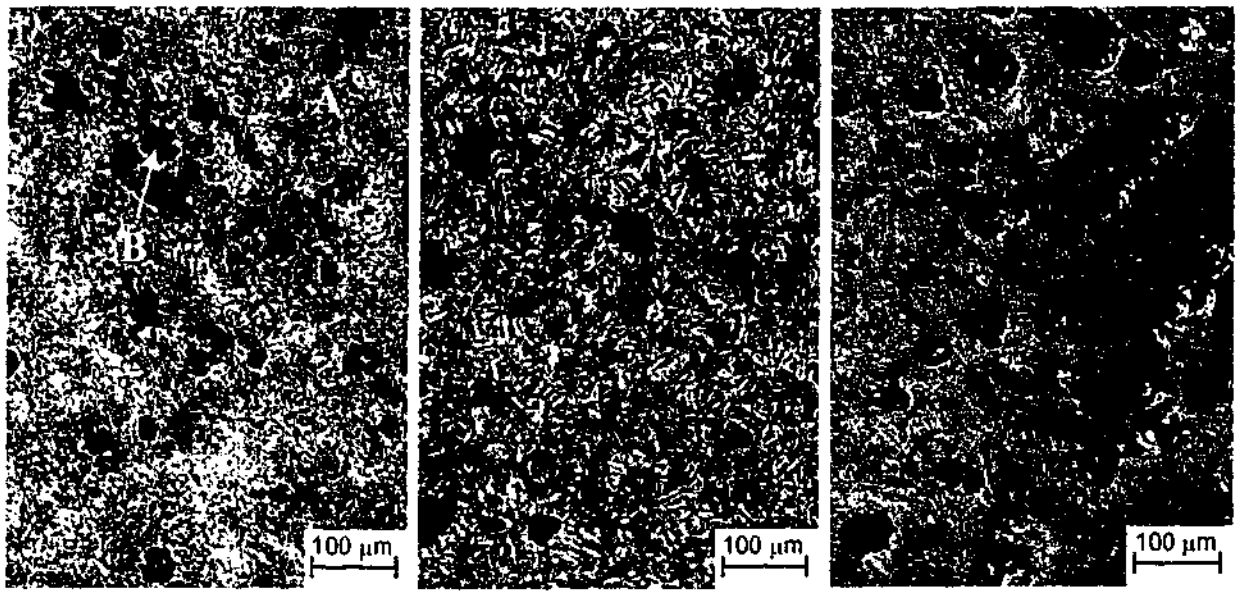

(a) (b) (c)

Figure 5.18 Micrograph of the tensile test specimens corresponding to test bar 2 at (a) 300°C, (b) 340°C and (c) 380°C austempering temperatures (Microstructural constituents: ausferrite (A) and graphite nodule(B)).

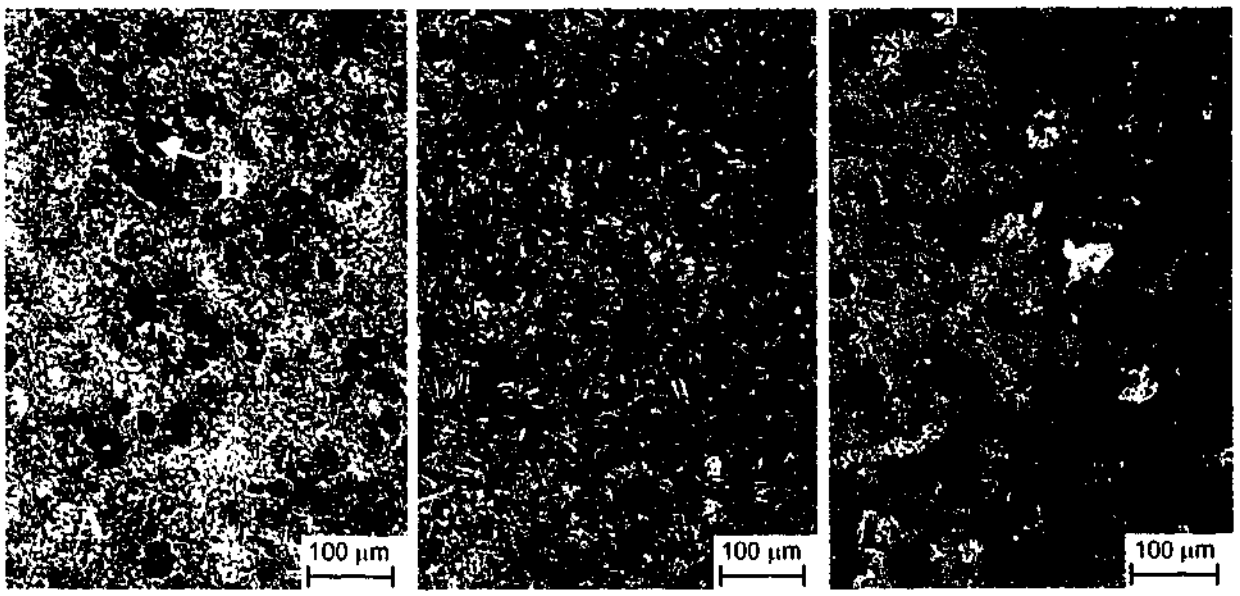

(a) (b) (c)

Figure 5.19 Micrograph of the impact test specimens corresponding to test bar 2 at (a) 300°C, (b) 340°C and (c) 380°C austempering temperatures (Microstructural constituents: ausferrite (A) and graphite nodules (B)).

The experimental cooling curves did not match the simulated quenching curves between 300-550°C (Figures 5.16 and 5.17) due to a limited control of the cooling rate of the specimens during quenching from austenitising to austempering temperature (Figure 3.3). However, departure of the experimental curves from the simulated curves took place at temperatures lower than that for the nose of pearlite curve (Figures 5.16 and 5.17), thus it did not affect pearlite formation in the matrix.

Ultimate tensile strength (UTS), yield strength, elongation and un-notched Charpy impact energy of test bar 2, corresponding to austempering temperatures of 300, 340 and 380°C, were compared with the lowest acceptable values for mechanical properties (defined by ASTM standard) (Figures 5.20 and 5.21).

The values for tensile strength, yield strength, impact energy and elongation were located beyond the minimum values of the ASTM for mechanical properties of ADI (Figures 5.20 and 5.21). This confirmed that the ASTM standard was satisfied at 300, 340 and 380°C austempering temperatures. Hardness values of test bar 2 specimens were located between the upper and lower boundaries of hardness defined by ASTM standard for 5 grades of ADI (Figure 5.22) and also satisfied the standard.

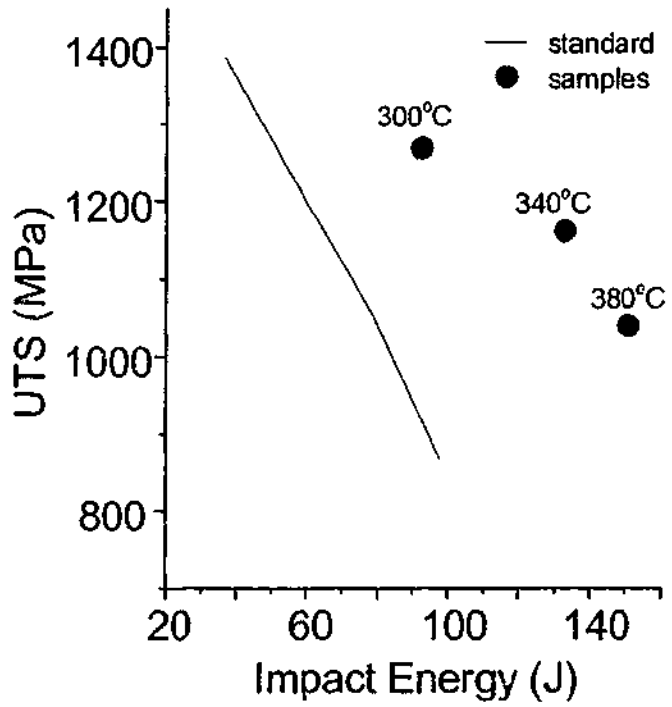

(a)

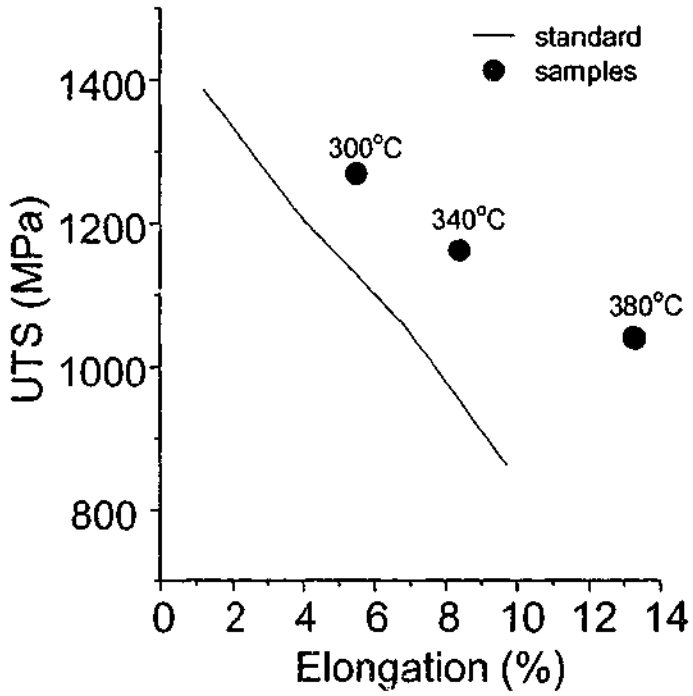

(b)

Figure 5.20 Ultimate tensile strength (UTS) versus impact energy (a) and UTS versus elongation (b) for all tested specimens of test bar 2.

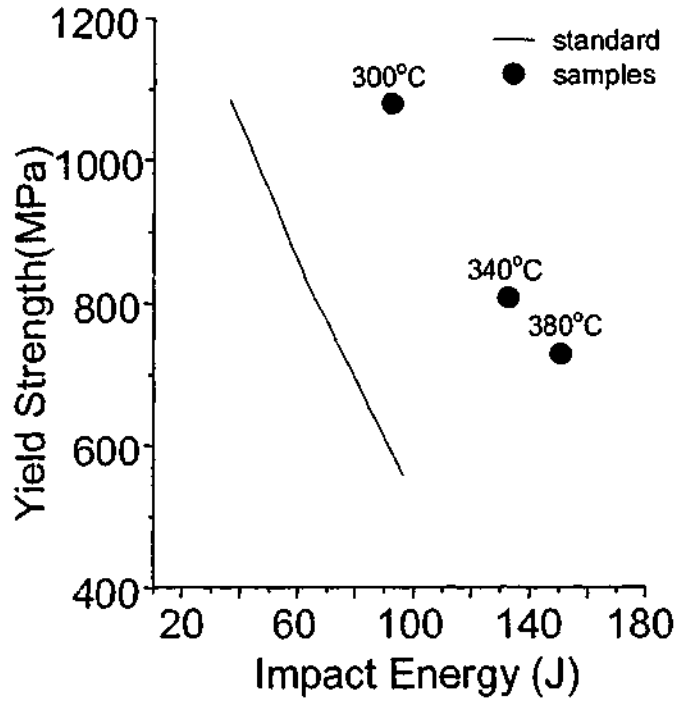

(a)

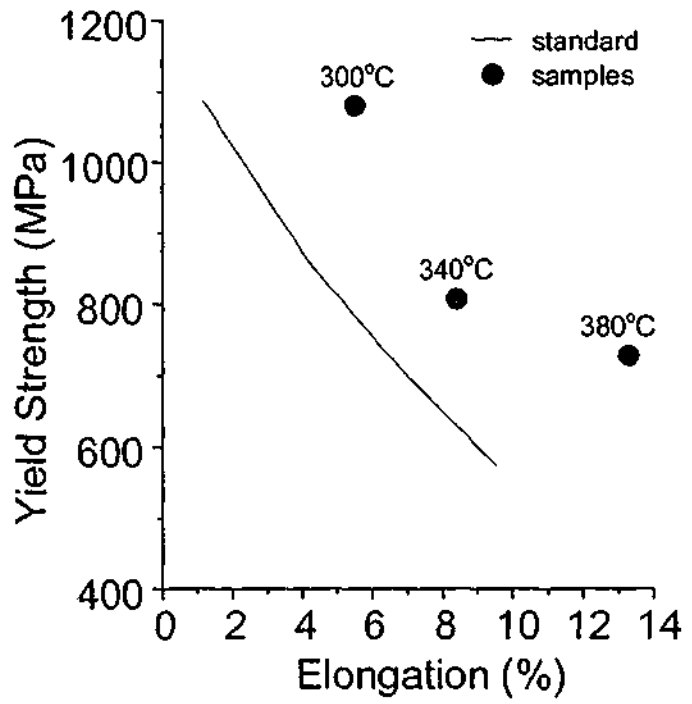

(b)

Figure 5.21 Yield strength versus impact energy (a) and yield strength versus elongation (b) for all tested specimens of test bar 2.

An increase in austempering temperature results in an increase in impact energy for test bar 2, from 93 J at 300°C to 133 J at 340°C and 155 J at 380°C (Figure 5.20a and 5.21a). In contrast, the ultimate tensile strength (UTS) of the test bar decreases with an increase in austempering temperature from 1271 MPa at 300°C to 1163 MPa at 340°C and 1040 MPa at 380°C (Figure 5.20a). Similarly, the yield strength of the test bar decreases with an increase in austempering temperature from 1080 MPa at 300°C to 808 MPa at 340°C to 723 MPa at 300°C (Figure 5.21a). Elongation increases from 5.5% at 300°C to 8.5% at 340 and 13.5% at 380°C (Figures 5.20b and 5.21b). The hardness of the test bar 2 improves from 305 BHN to 450 BHN with a decrease in austempering temperature from 380°C to 300°C (Figure 5.22).

At low austempering temperatures (300°C) the microstructure consists of a fine (needle-like) dispersion of (ausferritic) ferrite platelets and relatively small amount of HCA (Figures 5.23a and 5.24). The volume fraction of HCA (18%) is the lowest at 300°C compared to 340 and 380°C (Figure. 5.24).

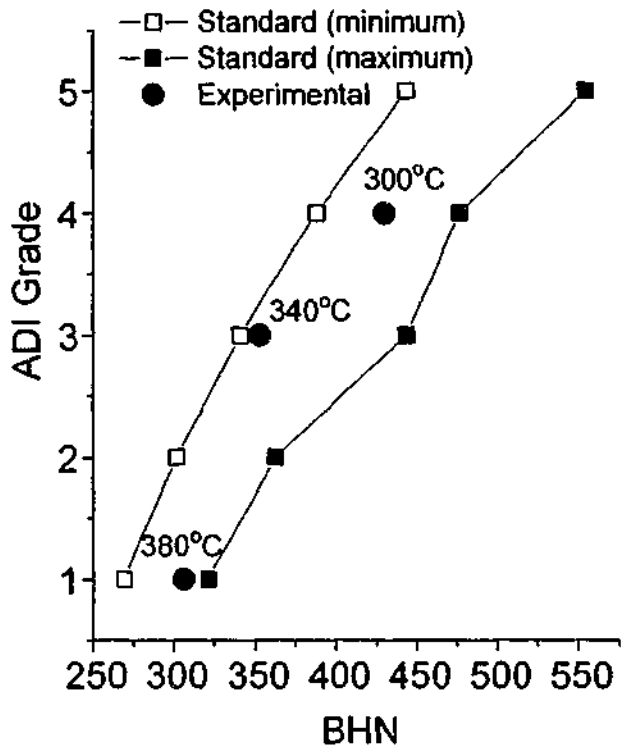

Figure 5.22 Comparison of the hardness of test bar 2 specimens with ASTM standard for ADI at austempering temperatures 300, 340 and 380°C.

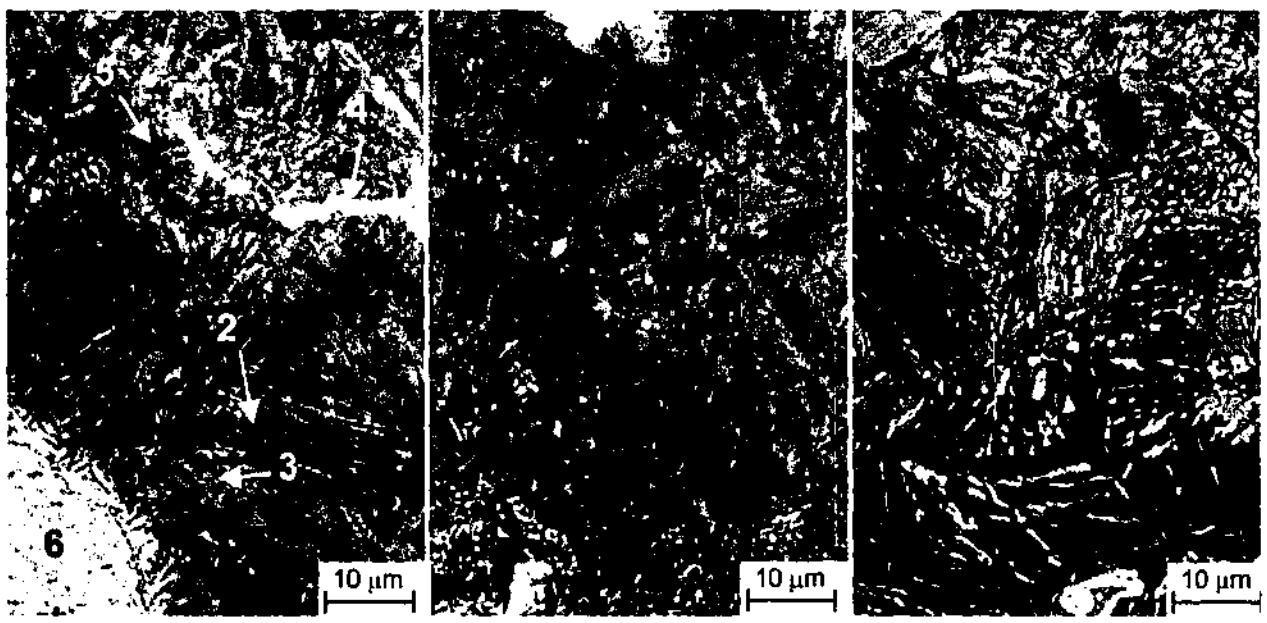

(a) (b) (c)

Figure 5.23 Microstructure of test bar 2 austempered at (a) 300°C, (b) 340°C and (c) 380°C corresponding to Figure 5.14 experimental points: 1- High Carbon Austenite (reacted austenite with 1.2-1.6%C), 2- High Carbon Austenite (reacted stable austenite with 1.8-2.2%C), 3- (Ausferritic) ferrite, 4- Eutectic carbide, 5- Martensite and 6- Graphite nodule.

Impact energy and elongation were the highest at 380°C among the other austempering temperatures (Figures 5.20 and 5.21). At 380°C, the microstructure consisted of feathery-like (ausferritic) ferrite with the highest volume fraction of the HCA (29.5%) among the other austempering temperatures (Figures 5.23c and 5.24). At 340°C the matrix of test bar 2 consisted of an intermediate microstructure of 300 and 380°C with 24% HCA (Figure 5.23b).

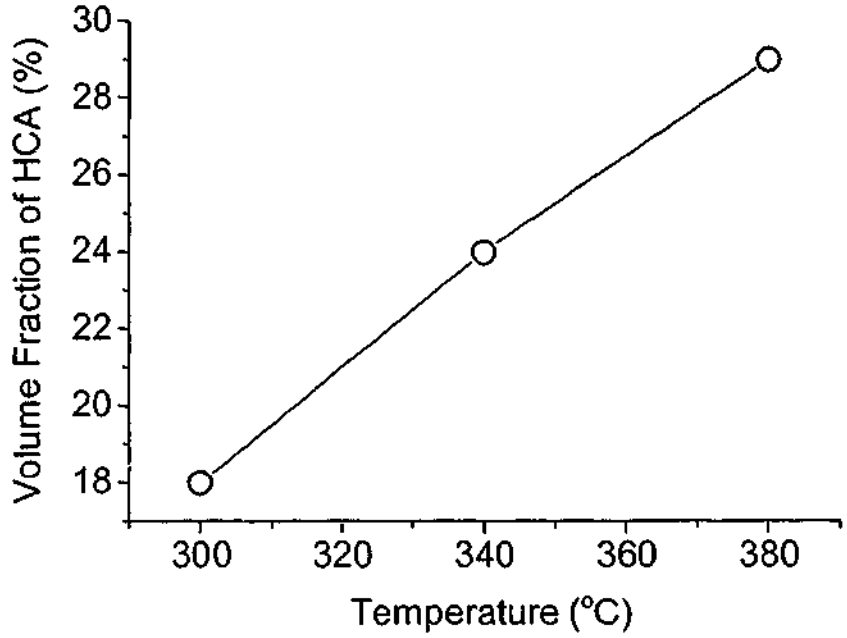

Figure 5.24 High carbon austenite (HCA) volume fraction at 300, 340 and 380°C associated with the specimens heat treated within the predicted processing-austemperability window of test bar 2.

5.4.2 Discussion

In this section two issues are addressed: (i) fulfillment of the minimum values for mechanical properties (defined by ASTM standard for ADI) within

the predicted processing-austemperability window of test bar 2; (ii) absence of pearlite in test bar 2 matrix after austempering process.

Results show that the time for isothermal transformation at 300, 340 and 380°C selected within the processing-austemperability window of test bar 2 produces an ADI with mechanical properties consistent with the ASTM A897M:1990 standard (Figures 5.20 and 5.21). This shows that a correct proportion of HCA and martensite is achieved in the test bar 2 matrix.

In this study microstructural constituents (such as martensite and HCA) are considered to be similar for the processing window and the processing-austemperability window. This is because for both windows the material is quenched rapidly from the austenitising to austempering temperature to prevent formation of pearlite. However, to validate the predicted values for austemperability reported in the processing-austemperability window diagram, a slower cooling rate is applied to the specimens to simulate the cooling rate corresponding to maximum section size of the material compared to the processing window diagram.

This slow cooling rate does not affect the volume fraction of HCA and martensite in the microstructure that identify the processing window and processing-austemperability window boundaries. The reason for this is that the transformation of austenite to ausferritic ferrite and HCA occurs during the

isothermal holding, and transformation of martensite takes place at temperatures lower than the austempering temperature.

The absence of pearlite in tensile and impact specimens (Figures 5.18 and 5.19) shows that the model estimates the austemperability of test bar 2 at 300, 340 and 380°C correctly. This observation proves that consideration of Si and C concentrations for estimation of the onset of pearlite formation and the calibrated heat transfer model lead to successful estimation of the austemperability for test bar 2.

A side-view of the Figure 5.14 shows that (within the processing-austemperability window) austemperability decreases from 24.5mm to 22 mm with an increase in austempering temperature from 285°C to 400°C (Figure 5.25). This is due to a decline in cooling rate at 400°C compared to 280°C, which leads to a delay in heat transfer and therefore, a decrease in austemperability.

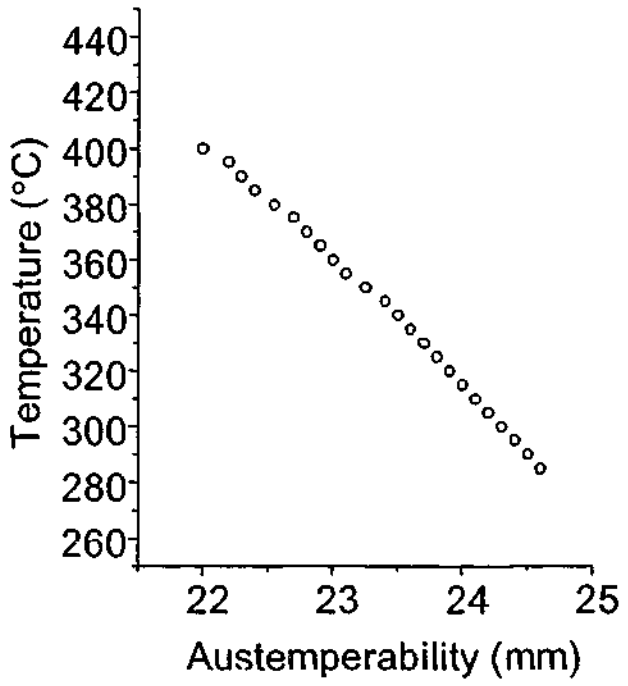

Figure 5.25 Austempering temperature versus austemperability view corresponding to the three-dimensional processing-austemperability window of test bar 2 (Figure 5.14).

CHAPTER 6

Discussion

6.1 Introduction

It was shown (Chapter 5) that the ASTM standard for the mechanical properties of ADI were successfully fulfilled by selection of the austempering time within the processing-austemperability window corresponding to test bar 2. The estimated boundaries for the processing-austemperability window of test bar 2 were computed from two separate models, (i) processing window and (ii) austemperability. However, both models have limits that are a result of insufficient fundamental information associated with the ADI microstructure, such as segregation. In the following, the rationales to overcome these limits are discussed.

6.2 The processing window

In order to estimate the processing window boundaries, two mathematical models corresponding to the kinetics of the austempering process are required. Firstly, a model for the isothermal transformation of austenite to ausferrite is required in order to simulate the time at which stage I reaction finishes (3% martensite presents) in the matrix of the ADI. Secondly, a model for estimation of the time at which stage II reaction starts (10% of the maximum amount of HCA transforms to ausferritic ferrite and carbide) in the matrix. However, no model has been developed that anticipates the times associated with the processing window boundaries and therefore, a model for bainite transformation and experimental data sourced from the literature were utilised to achieve our aim.

6.2.1 The lower boundary of the processing window

As explained in Chapters 4 and 5, Equation 4.1 was calibrated for estimation of the lower boundary of the processing window. This was due to the fact that direct application of Equation 4.1 leads to over-estimation of the time for isothermal transformation of austenite to (ausferritic) ferrite. For instance, the experimental results of Yazdani and Elliott (1999) for iron 1 (Figure 4.1) show that at a 285°C austempering temperature, the ausferritic reaction (stage I reaction) finishes at 1170 seconds. For the same temperature, Equation 4.1 predicts completion of the reaction at 10^{12} seconds (Figure 6.1).

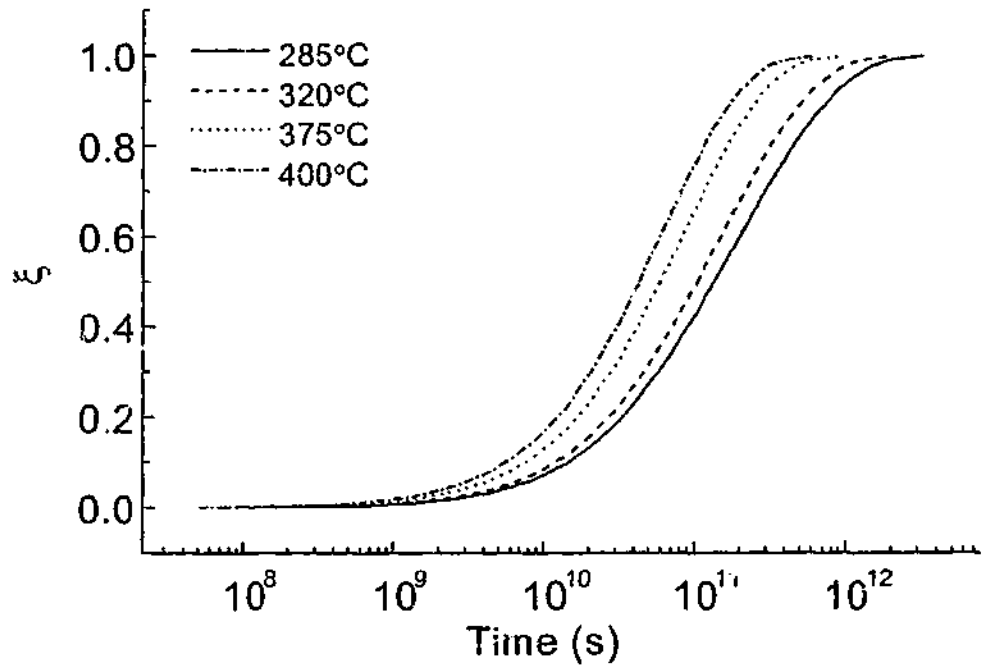

Figure 6.1 The ξ versus log (t) at different austempering temperatures corresponding to iron 1 (β is calculated from Equation 4.3)

It seems that the difference between the estimated and experimental time is largely a result of the segregated microstructure of the ADI. This may result in the isothermal reaction occurring at higher rates in the eutectic cells (where ferrite stabilising alloying elements such as Si are present in higher concentrations) compared to intercellular areas (which bears a high concentration of austenite stabilising alloying elements).

For instance, segregation of the ferrite stabilising alloying elements such as Si and Cu to the cellular area (Chapter 2) facilitates carbon partitioning from ferrite to the neighbouring austenite. This leads to an increase in the rate of isothermal transformation in the eutectic cells compared

to intercellular area, where austenite stabilising alloying elements such as Mn and Mo segregate.

As explained before, Equation 4.1 estimates the isothermal transformation time in high Si steels in which segregation either does not exist or is minimal compared to ADI. Therefore, the effect of segregation has to be accommodated in the model for estimation of the time for isothermal transformation.

Attempts have been made to predict segregation of the alloying elements in ADI (Liu and Elliott, 1998a, 1998b and 1999). However, no comprehensive model is yet available to predict the alloying composition profile in ADI microstructure: a model which takes nodule count and alloying elements of ductile iron and anticipates alloying elements gradient between graphite nodules in the matrix.

For this reason, the autocatalysis factor (β) that shows the effect of carbon partitioning in the Equation 4.1 was calibrated according to experimental data corresponding to irons 1, 2 and 3 sourced from the literature (Figure 4.1) (Elliott, 1997). Equation 4.1 has already been utilised in a model for prediction of the volume fraction of microstructural constituents of ADI (James & Thomson, 1998, 1999; Thomson et al., 2000). In this model the proportion of the ausferritic ferrite (bainitic ferrite), (retained) austenite and martensite are estimated according to the maximum volume fraction of

ausferritic ferrite that can be calculated for composition of the ductile iron using the lever rule.

Thomson et al. (2000) modified the autocatalysis factor β from a linear function to an exponential function, however, details on how they have achieved the fitting function of β have not been provided. This model does not estimate the processing window boundaries that are important to identify the optimum austempering time for ADI to achieve the ASTM standard.

For instance, at high austempering temperatures (i.e. 400°C) the time to reach the maximum volume fraction of ausferritic ferrite (end of the stage I reaction) may not be the optimum time for austempering. This is due to the fact that the stage II reaction may have already been well advanced in the eutectic cells at high austempering temperatures (processing window is closed) which is detrimental to the mechanical properties of the material.

The original β calculated from Equation 4.3 (proposed by Rees and Bhadeshia (1992) and refined by Chester and Bhadeshia (1997)), the modified β by Thomson et al. (2000) and the calibrated β (corresponding to this study) for irons 1, 2 and 3 are shown in Table 6.1. A comparison between the β values calculated from previous studies and this study shows that the original β possesses a smaller value with a difference in sign compared to the modified β and calibrated β in this study (Table 6.1).

In contrast to the original β and the modified β the value for the calibrated β declines with an increase in austempering temperature (Table 6.1). This is because of a decrease in driving force for ausferritic reaction at high austempering temperatures. However, the calibrated β value for iron 1 at 375°C is slightly smaller than that at 400°C (Table 2). This is perhaps because of a longer experimental time corresponding to lower boundary of iron 1 processing window at 375°C compared to 400°C (Figure 1). This difference between β values at 375 and 400°C corresponding to iron 1 needs further study.

The original and modified β corresponding to iron 2 have the lowest values among irons 1, 2 and 3 (Table 6.1). This is in contrast to calibrated β that possess the lowest (overall) values for iron 3 among the other irons. These differences between the original, the modified and the calibrated β create difficulties in the explanation of the β value by physical means and demands further study of the autocatalysis factor for ausferritic reaction.

Iron	$\bar{x}$	T_A (°C)	Original β*	Modified β **	Calibrated β ***
1	0.0381	285	-22.93	14.63	676.84
		320	-22.93	14.63	597.84
		375	-22.93	14.63	226.26
		400	-22.93	14.63	228.56
2	0.0389	285	-26.51	13.94	171.4
		320	-26.51	13.94	153.69
		375	-26.51	13.94	18.3
		400	-26.51	13.94	12.9
3	0.0386	285	-25.17	14.19	150.52
		320	-25.17	14.19	125.65
		375	-25.17	14.19	1.01
		400	-25.17	14.19	1.5×10^{-22}

* Reference (Chester & Bhadeshia, 1997)
** Reference (Thomson et al., 2000)
*** This study

Table 6.1 Comparison of the original β (calculated from the Equation 4.3), the calibrated β (computed from Equation 4.5) and the β function modified by James and Thomson (1998) corresponding to irons 1, 2 and 3.

However, segregation may contribute to these differences. For example, the original and modified equations for β are developed according to steels microstructure in which segregation of alloying elements is very limited and therefore the value for $\bar{x}$ does not change in steels matrix. In spite of this, it is well known that mole fraction of carbon in ADI matrix changes in eutectic

cells compared to intercellular areas due to segregation of alloying elements. This means that the values for $\bar{x}$ in Table 6.1 do not exactly represent the real value corresponding to mole fraction of carbon in irons 1, 2 and 3. Ideally, a profile of $\bar{x}$ (in eutectic cells and intercellular areas) may identify a more realistic value for mole fraction of carbon in the matrix. However, application of β as a "calibration" factor for estimation of the lower boundary of the processing window (using bainite transformation model) has shown to be successful in respect to experimental evaluations (of test bar 2) in this study.

Apart from minor deviations in the predicted lower boundary of the processing window the model is calibrated successfully for the start of the austempering window corresponding to irons 1 and 2 (Figures 4.6a and 4.6b). However, the estimated t_1 curve of iron 3 does not match the experimental data at 375 and 400°C (Figure 4.6c) due to the fact that the calibrated isothermal transformation model only computes the t_1 curve for the point at which maximum volume fraction of ausferritic ferrite is achieved (end of the stage I reaction).

Beyond this point the processing window is closed and further formation of (bainitic) ferrite is due to decomposition of the HCA (stage II reaction). This is confirmed by the calibrated β values corresponding to iron 3 at 375 and 400°C which possess the lowest values among other temperatures

(Figure 4.3). This means that the autocatalysis for ausferritic reaction either does not occur or is very limited due to a decrease in driving force for austenite to ausferrite transformation at high austempering temperature.

Departure of the calibrated t_1 curves from the experimental data leads to overestimation of the temperature at which the processing window is closed (Figures 4.9b and 4.9c). This is because of the mathematical limitations for back calculation of β function that is due a limited experimental data (12) available for computation of the β regression function. Among calibration data no experimental data was available corresponding to the point at which the processing window was closed (Figure 1). An increase in the number of calibration data may improve this limitation of the model.

In contrast to the experimental data points, the estimated time corresponding to the lower boundary of the processing windows for irons 1, 2 and 3 decreases with an increase in austempering temperature at temperatures above 375°C (Figure 4.6). This decrease prevents closure of the processing window corresponding to iron 3 (Figure 4.6c) and the discrepancy arises because of the polynomial nature of the fitting function, β (Equation 4.5). However, because the function estimates a continuous austempering time (for the austempering range of 285-400°C) in respect to discrete experimental data, an increase in the number of experimental points may improve fitting function,

β, and therefore the difference between the estimated and experimental austempering times at the lower boundary of the processing window.

The calibration function (Equation 4.5) associated with the autocatalysis factor estimates the austempering time, in respect to Equation 4.1, if the mole fraction of carbon ($\bar{x}$) is within the range 0.0381-0.0389 and the austempering temperature is within 285-400°C boundaries. The influence of the alloying elements and austenitising temperature is on austenite carbon content ($\bar{x}$) prior to isothermal transformation. The effect of austempering temperature is mostly on driving force for isothermal transformation and carbon (ejected from ferrite) diffusion in austenite during isothermal holding.

The prior austenite grain size is included in the model for isothermal transformation due to its effect on the time for isothermal transformation (Chester & Bhadeshia, 1997). The smaller the austenite grain size (in steels) the shorter the time for isothermal transformation. A large austenite grain boundary area (small grain size) provides more nucleation sites for ferrite to nucleate from the parent austenite and therefore, leads to a shorter isothermal transformation time (Bhadeshia, 1992). The alloying elements, austenitising temperature and time may change the austenite grain size and therefore, austempering time. However, the effect of prior austenite grain on the kinetic of the austempering process in ADI microstructure has not yet been studied.

For simplicity, in this study the austenite grain size is considered to be constant (65 μm) for an austenitising time of 2 hours. However, the model predicts a decrease in the isothermal transformation time corresponding to the lower boundary of the processing window of test bar 2 with a decrease in prior austenite grain size. For instance, the model anticipates a decrease in the time to finish the stage I reaction (t_1) for a 25 μm prior austenite grain size (<65 μm) of test bar 2 from 3276 to 1260 seconds at an austempering temperature of 340°C (Figure 6.2). This may lead to time and energy savings associated with the austempering process, and therefore it requires further study.

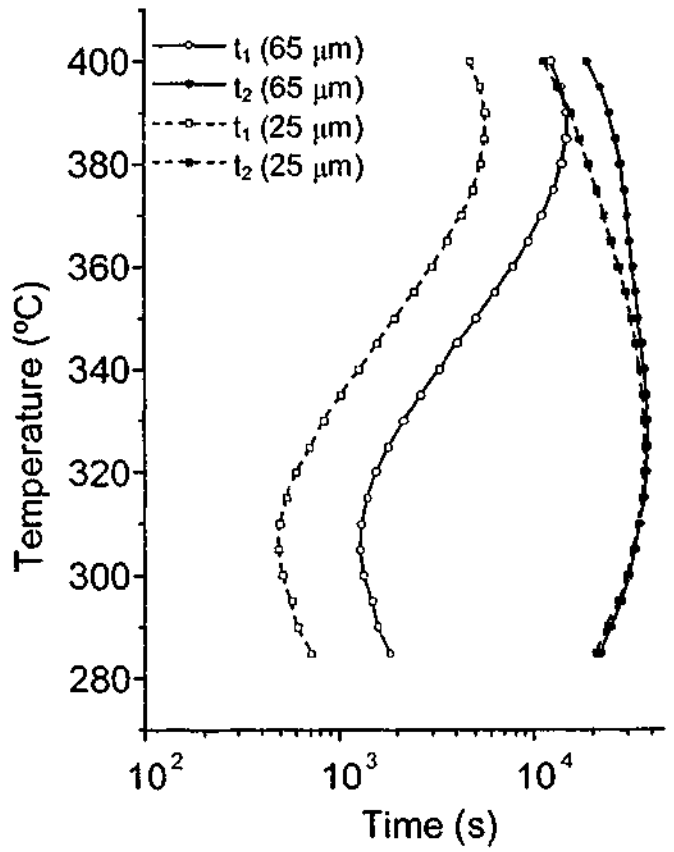

Figure 6.2 Comparison of the predicted processing windows for test bar 2 with 65μm and 25μm prior austenite grain size.

6.2.2 The upper boundary of the processing window

It was shown (Chapter 4) that a multiple linear regression function (Δt) calibrates the model for prediction of the upper boundary of the processing window. However, the calibration curves do not match the experimental points at which the processing window is closed ($t_1 > t_2$) (Figures 4.9b and 4.9c). This difference between the calibration data and the experimental data is due to a mathematical limitation of the model. The time interval Δt is calculated from a logarithm function (Equation 4.6) that always requires a positive value. This limitation is transmitted to the model for test bar 2 and is evident in the validation, as described below.

Firstly, departure of the calibrated t_2 curves from the experimental data at high austempering temperature leads to overestimation of the upper limit of the processing window (Figures 4.9b and 4.9c). This overestimation of the holding time leads to a further decomposition of the HCA to (ausferritic) ferrite and carbide and therefore, a lower than expected 90% normalised volume fraction of HCA.

This outcome is confirmed by experimental investigation in which the normalised volume fraction of HCA has less than expected values (90%) at all austempering temperatures (Figure 5.6). An increase in austempering temperature from 300 to 380°C leads to an increase in the difference between

the model and expected values for normalised volume fraction of austenite from 5 to 19% in test bar 2 matrix (Figure 5.6).

The most important effect of the overestimation of the predicted time for upper boundary of the processing window is associated with high austempering temperatures (370-400°C) in which closure of the processing window is overestimated. This causes ADI to fail to achieve the minimum requirements for ASTM A897M:1990 mechanical properties (Hamid Ali & Elliott, 1996a, 1996b). The impact of the closure of the processing window on mechanical properties of test bar 2 is not investigated in this study. This is due to the fact that for the chosen alloying elements and austenitising temperature, the predicted processing window of test bar 2 is open at high austempering temperatures (Figure 5.1).

Examination of the mechanical properties of test bar 2 within the predicted processing (processing-austemperability) window at 380°C (high) austempering temperature confirms that test bar 2 satisfies the ASTM standard and the processing window is open (Figures 5.20, 5.21 and 5.22). As explained in the previous chapter, the proportion of the microstructural constituents in the processing window and the processing-austemperability window are similar and therefore, mechanical properties of the material are considered to be identical.

Overall, the calibrated processing windows for irons 1, 2 and 3 show that the magnitude of the overestimation associated with closure of the processing window is reasonably low (10-15°C in Figures 4.9b and 4.9c). Therefore, overestimation of the model for prediction of the upper boundary and consequently closure of the processing window has a minimum impact on satisfaction of the ASTM standard for mechanical properties of ADI.

6.3 Austemperability

The approach for prediction of the austemperability of ADI is shown to be successful for test bar 2 of this study (Figures 5.18 and 5.19). However, incorporation of segregation of alloying elements and quench severity of the quenching media improve versatility of the model.

6.3.1 Segregation

In order to prevent overestimation of the austemperability, the pearlite curve of the TTT diagram was estimated according to the Si content of the iron (reported from the chemical analysis). Si is the most effective alloying element in pearlite formation and has the highest concentration around graphite nodules (Chapters 4 and 5). However, in reality other alloying elements such as Cu and Ni may be present to some extent in the vicinity of the graphite nodules and therefore, shifting the pearlite curve of the TTT diagram to a longer time (Figure 5.9). This means that possibly a larger

section size (radius) of the test bar can be austempered compared to that predicted in model.

Nodule count of the iron which has a direct effect on the segregation gradient of the alloying elements (Figure 2.8) leads to a change in the outcome of the computed austemperability. For example, a longer inter-nodule distance exacerbates the gradient of the Si concentration in the matrix with the highest concentration around graphite nodules (Figure 2.7). This leads to a change in the local chemical composition and therefore, onset of the time for pearlite formation in the matrix. Quantification of segregation and its relationship with nodule count needs further study.

6.3.2 Quench severity of the quenching media

Quench severity of the quenching media was not considered in this study due to the assumption that for a large section size ductile iron heat transfer is mostly controlled by internal resistance of the media (conduction) (Poirior & Geiger, 1994). This assumption was proven successful for test bar 2 of this study. However, implementation of convection which includes quench severity of the quenchant benefits the model for further accuracy and versatility, even for a thin section size material.

6.4 The processing-austemperability window

The ASTM standard for mechanical properties is fulfilled for the experimental points chosen on the three-dimensional processing-austemperability window of test bar 2 (Figures 5.20 and 5.21). Any point on the 3D diagram of the processing-austemperability window indicates that the limits for the volume fraction of martensite (3%), normalised volume fraction of the HCA (90%) and pearlite (0%) in the microstructure of ADI are met. This shows that the processing-austemperability window is more informative compared to the processing window in which the limit for pearlite formation is not provided.

Another advantage of the processing-austemperability window is that it may lead to development of a generic model in which a large amount of processing windows are predicted, representing a volume (Figure 6.3). Coordinates of any point within the processing-austemperability window represents an ADI of a particular composition, nodule count, austenitising time, austenitising temperature, austempering time and austempering temperature. Such a diagram may assist the heat treatment industry in choosing the proper austempering time and temperature for a particular batch of ductile iron products. This is important because it is difficult for foundries to produce identical batches of ductile iron, which leads to inconsistency in properties of ADI.

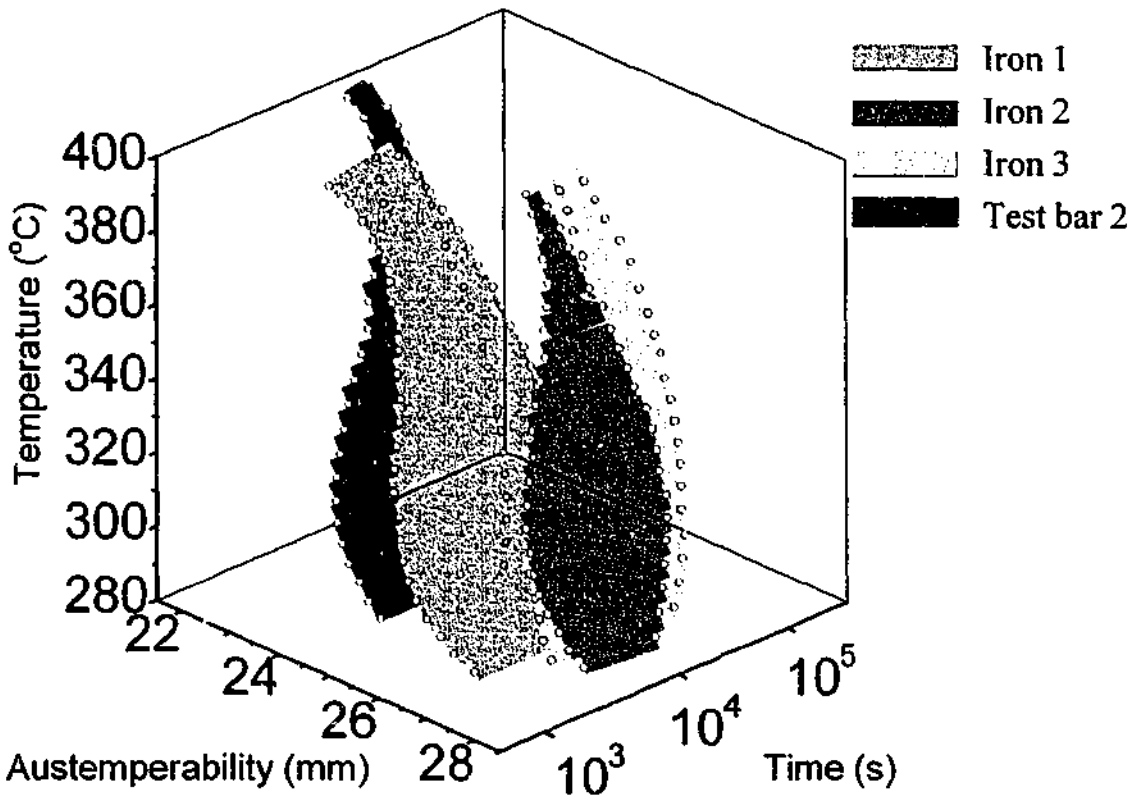

Figure 6.3 Variation of the processing-austemperability window with alloying elements and austenitising temperature (corresponding to iron 1, iron 2, iron 3 and test bar 2).

6.5 Summary

The rationales in respect to the processing window, austemperability and the processing-austemperability window models were discussed in this chapter. It was shown that calibration of a model for bainite transformation in high Si steels according to experimental data for irons of this study (which were sourced from the literature) and autocatalysis (calibration) factor β leads to estimation of the lower boundary of the processing window.

The upper boundary of the processing window was predicted successfully using a multiple linear regression function (Δt) and the

experimental data corresponding to irons 1, 2 and 3. It was demonstrated that prediction of the pearlite curve of the TTT diagram according to Si and corresponding carbon content of ductile iron leads to a correct estimation of the austemperability for test bar 2.

Notwithstanding the successful validation of the models for the processing window, austemperability and the processing-austemperability window, there are limitations associated with the initial and boundary conditions of the model. Inputs which are out of the nominated range for mole fraction of carbon (0.0381-0.0389) and austempering temperature (285-400°C) lead to errors associated with multiple linear regression (Montgomery & Runger, 1999).

Mole fraction of carbon (or carbon concentration in the austenite prior to quenching to austempering temperature) was estimated from the alloying elements composition and austenitising temperature in the model (Equation 4.2). Therefore, careful attention must be taken to choose an appropriate combination and composition of the alloying elements and austenitising temperature to achieve the $\bar{x}$ within the defined range of 0.0381-0.0389. Currently, the only way to predict the processing window over a wider range of alloy compositions and austenitising temperatures is to employ more calibration data.

Finally, the model for prediction of the processing-austempering window does not consider segregation of the alloying elements and the resultant effect on the time for isothermal transformation (stage I and stage II) reactions and onset of pearlite formation in the matrix of ADI.

Of these, segregation is perhaps the most difficult to accommodate and it is speculated that a significantly more complex model would be required to take the effect into account. It is however, re-iterated that the current approach of calibrating a model using existing experimental data has been shown to be adequate for practical purposes.

CHAPTER 7

Conclusions

The present work reveals the following conclusions for modelling of the processing window and austemperability of austempered ductile iron:

The lower boundaries of the processing window were estimated using a model for the isothermal transformation of austenite to carbide free bainite in high Si (>1.5%) steels and experimental data available in the literature. The difference between the beginning and the end of the austempering window (obtained from the literature data) was added to the predicted lower boundary of the processing window (t_1) to estimate the end of the austempering window.

The model successfully predicts the processing window boundaries for the validation alloy. However, the model exhibits about 20% error for the

lower and upper boundaries of the processing window corresponding to the validation alloy. These errors are due to mathematical limitations in the calculation of the fitting functions for calibration of the isothermal transformation model and estimation of the upper limit of the processing window.

The outcome of this study shows that the bainite model developed for high Si steels, with some modifications, is applicable for the estimation of the processing window boundaries.

The austemperability of the ADI is predicted according to the point at which the quenching curve touches the pearlite curve of the TTT diagram at the centre of the ductile iron cylindrical test bar. The quenching curve for a heavy section size ductile iron is simulated according to the experimental data and a model for simulation of heat transfer in a solid cylindrical ductile iron. The model predicts austemperability of the validation alloy successfully. However, incorporation of segregation and quench severity of the quenching media may improve the model outcome.

The simulated processing window and austemperability results are presented in a three-dimensional diagram. The model for estimation of the processing-austemperability window is evaluated according to mechanical properties of the validation alloy. The outcome of the experimental results satisfies the minimum requirements for the ASTM A897M:1990 standard, for

the isothermal transformation time chosen within the predicted processing-austemperability boundaries.

The results show that elongation and impact energy corresponding to the alloy of this study increase with increasing austempering temperature. In contrast, an increase in austempering temperature decreases the tensile strength and hardness of the material. These outcomes are consistent with findings in the literature.

The model could benefit the heat treatment industry by implementing time and energy savings associated with the austempering process.

Recommendations for Future Work

The following future works are recommended for improvement of the model for prediction of the processing-austemperability window.

As was frequently emphasised through this work, insufficient information on segregation of the alloying elements in the ADI matrix led us to use regression functions. A comprehensive model is needed to quantitatively predict alloying element gradients through the inter-graphite nodule distance. Such model is to take into account the nodule count of the iron that controls the inter-graphite nodule distance. Prediction of the segregation also results in a better estimation of the austemperability by providing alloying elements concentration in the vicinity of the graphite nodules, which is the place that pearlite starts to form.

A comprehensive model is necessary for prediction of the time associated with the stage II reaction in which HCA transforms to (bainitic) ferrite and carbide. This model also may lead to a better prediction of the time at which HCA saturates with carbon that is of importance for high ductility of ADI.

No model is yet available to predict the prior austenite grain size of ADI. A model for estimation of the prior austenite grain size may take into account the effect of austenitising time, austenitising temperature and alloying elements on the austenite grain growth. The information provided by such

model may lead to optimisation of the austenitising process by selection of the minimum austenitising time and temperature for ADI parts, as well as a shorter time for isothermal transformation.

The model for prediction of the austemperability may be improved by taking into account the pearlite curve of the CCT diagram instead of the current approach in which the pearlite curve of the TTT diagram is used. The predicted CCT diagram must take into account alloying elements concentration (segregation) profile around graphite nodules which may lead to a more realistic time and temperature in respect to onset of pearlite formation in ADI matrix. This may lead to a more realistic estimation of the austemperability for ADI. Finally, a heat transfer model that takes into account the quench severity of the quenching media improves the austemperability results.

REFERENCES

Ahlstrand, V., (1997) "*Austempered ductile iron: Possible usage for parts in the truck industry*", Heavy duty vehicle braking and steering SAE (Society of Automotive Engineering) special publication, 1307, 13-18.

Aranzabal, J., Gutierrez, I., Rodriguez-Ibabe, J.M. and Urcola, J.J., (1997) "*Influence of the amount and morphology of retained austenite on the mechanical properties of an austempered ductile iron*", Met. Mat. Trans. A, Vol. 28A, 1143-1156.

Bahmani, M. and Elliott, R., (1994) "*Effects of pearlite formation on mechanical properties of austempered ductile iron*", Mater. Sci. Technol., 10, 1068-1072.

Bahmani, M., Elliott, R. and Varahram, N., (1997) "*Austempered ductile iron: a competitive alternative for forged induction-hardened steel crankshafts*", Int. J. Cast Metals Res., 9, 249-257.

Bayati, H. and Elliott, R., (1995) "*Influence of austenitising temperature on mechanical properties of high manganese alloyed ductile iron*", Mater. Sci. Technol., 11, 908-913.

Bayati, H. and Elliott, R., (1997) "*Role of austenite in promoting ductility in an austempered ductile iron*", Mater. Sci. Technol., 13, 319-326.

Bayati, H. and Elliott, R., (1999) "*The concept of an austempered heat treatment processing window*", Int. J. cast metals res., 11, 413-417.

Bayati, H. and Elliott, R., (2000) "*Effect of microstructural features on the austempering heat treatment processing window*", Materials Science Forum, Vols 329-330, 73-78.

Bayati, H., Elliott, R. and Lomier, G.W., (1995) "*Stepped heat treatment for austempering of high manganese alloyed ductile iron*", Mater. Sci. Technol., 11, 1007-1013.

Bhadeshia, H.K.D.H. and Edmonds, D.V., (1980) "*The mechanism of bainite formation in steels*", Acta Metallurgica, 28, 1265-1273.

Bhadeshia, H.K.D.H., (1982) "*Bainite: Overall transformation kinetics*", Journal De Physique C4, 443-448.

Bhadeshia, H.K.D.H., (1992) "Bainite in steels", Cambridge University Press, UK.

References

Blackmore, P.A. and Harding, R.A., (1984) "*The Effect of Metallurgical Process Variables on the Properties of Austempered Ductile Irons*", J. Heat Treating, Vol. 3, No.4, 310-325.

Callister, W.D., (1991) "Materials Science and Engineering an Introduction", John Wiley & Sons, USA.

Campos-Cambranis, R.E., Narvaez Hernandez, L., Cisneros-Guerrero, M.M. and Perez-Lopez, M.J., (1998) "*Effect of initial microstructure on the activation energy of second stage during austempering of ductile iron*", Scripta Materialia, Vol. 38, No. 8, 1281-1287.

Chatterley, T.C. and Murrell, P, (1998) "*ADI crankshafts – An appraisal of their production potential*", Advancements in fatigue research and applications SAE (Society of Automotive Engineering) special publications", 1341, 17-39.

Chester, N.A. and Bhadeshia, H.K.D.H., (1997) "*Mathematical modelling of bainite transformation kinetics*", J. Phys. IV France7, C5, 41-46.

Cullity, B.D., (1978) "Elements of X-ray diffraction", Addison-Wesley Co.

Darwish, N. and Elliott, R., (1993) "*Austempering of low manganese ductile irons Part 1 Processing Window*", Mater. Sci. Technol., 9, 572-585.

Davis, J.R., (1996) "Cast Irons", ASM specialty handbook edited by J.R. Davis, ASM international, Metals Park, OH.

Dorazil, E., Munsterova, E., Karpisek Z. and Barta B., (1989) "*Examination of the hardenability of ductile cast iron in austempering*", Kovo Materialy, 27, 1, 53-67.

Dorazil, E., Munsterova, E., Karpisek Z. and Stransky, L., (1986) "*Prokalitelnost tvarne litiny pri izotermickem zuslechtovani*", Slevarenstvi (translated from Czech language), 2-7.

Ductile Iron Society, (1999), [online]. Available: http://www.ductile.org/didata/Section4/4intro.htm (Accessed: 20 June 2001).

Elliott, R., (1997) "*The role of research in promoting austempered ductile iron*", Heat Treatment of Metals, 3, 55-59.

Hamid Ali, A.S. and Elliott, R., (1996a) "*Austempering of an Mn-Mo-Cu alloyed iron Part2-Structure-mechanical property relationships*", Mater. Sci. Technol., 12, 780-787.

Hamid Ali, A.S. and Elliott, R., (1996b) "Austempering of an Mn-Mo-Cu alloyed ductile iron Part1 - Austempering kinetics and processing window", Mater. Sci. Technol., 12, 679-690.

Hamid Ali, A.S. and Elliott, R., (1997) "*Influence of austenitising temperature on austempering of an Mn-Mo-Cu alloyed ductile iron Part2 - Mechanical properties*", Mater. Sci. Technol., 13, 24-30.

Hayrynen, K., (1995) "*ADI: Another avenue for ductile iron foundries*", Modern Casting, 36.

Hehemann, R.F., Kinsman, K.R. and Aaronson, H.I., (1972) "*A debate on the bainite reaction*", Metallurgical Transactions, 3, 1077-1094.

Honeycombe, R.W.K. and Bhadeshia, H.K.D.H., (1995) "Steels microstructure and properties", Edward Arnold Co., 338 Euston Road, London NW1 3BH, UK.

James, J. S. and Thomson, R. C., (1998) "*Microstructural modelling of austempered ductile iron*", in Proceedings of Cast Conference Bournemouth, British Institute of Foundrymen, 47-60

James, J. S. and Thomson, R. C., (1999) "*Microstructural Modelling of Austempered Ductile Iron*", in Proceedings of PTM 99, Kyoto, Japan, 1473-1476

Kazerooni, R., Nazarboland, A. and Elliott, R., (1997) "*Use of austenitising temperature in control of austempering of an Mn-Mo-Cu alloyed ductile iron*", Mater. Sci. Technol., 13, 1007-1015.

Keough, J., (1995) "*An ADI Market Primer*", Foundry Management and Technology, 123, 10, 28-31.

Kovacs, B.V., (1987) "*A simple technique to identify various phases in austempered ductile iron*", Modern Casting, 34-35.

Kovacs, B.V., (1994) "*On the terminology and structure of ADI*", AFS Trans., 102, 417-420.

Lee, Y. H. and Voigt, R.C., (1989) "*The hardenability of ductile irons*", AFS Trans., 97, 915-938.

Liu, J. and Elliott, R., (1998a) "*The influence of cast structure on the austempering of ductile iron part1: Modelling of the influence of nodule count on microstructure*", Int. J. Cast Metals Res., 10, 301-305.

Liu, J. and Elliott, R., (1998b) "*Numerical model for microsegregation in ductile iron*", Mater. Sci. Technol., 14, 1127-1131.

Liu, J. and Elliott, R., (1999) "The influence of cast structure on the austempering of ductile iron part2: Assessment of model calculations of microsegregation", Int. J. Cast Metals Res., 12, 75-82.

Materials Algorithm Project Program Library, (1999a), [online]. Available: http://www.msm.cam.ac.uk/map/steel/programs/mucg73-b.html (Accessed:15 December 1999).

Materials Algorithm Project Program Library, (1999b), [online]. Available: http://www.msm.cam.ac.uk/map/steel/functions/newf2-b.html (Accessed: 15 December 1999).

Materials Algorithm Project Program Library, (1999c), [online]. Available: http://www.msm.cam.ac.uk/map/steel/functions/mv-b.html (Accessed: 15 December 1999).

Montgomery, D.C. and Runger, G.C., (1999) "*Applied statistics and probability for engineers*", John Wiley and Sons Inc. 483-520.

Moore, D.J., Rouns, T.N. and Rundman, K.B., (1985) "*Structure and Mechanical Properties of Austempered Ductile Iron*", AFS Trans., 93, 705-718.

Nallicheri, N.V., Clark, J.P. and Field, F.R., (1991) "*Material alternative for the automotive crankshaft; A competitive assessment based on manufacturing economics*", SAE Technical paper series (910139), 1-10.

Nazarboland, A. and Elliott, R., (1997a) "*The relationship between austempering parameters, microstructure and mechanical properties in a Mn-Mo-Cu alloyed ductile iron*", Int. J. Cast Metals Res., 9, 295-308.

Nazarboland, A. and Elliott, R., (1997b) "*The effect of intrinsic casting defects on the mechanical properties of austempered, alloyed ductile iron*", Int. J. Cast Metals Res., 10, 87-97.

Poirior, D.R. and Geiger, G.H., (1994) "Transport phenomena in materials processing", TMS, Warrendale, Pennsylvania 15085, USA, 281-300

Rees, G.I. and Bhadeshia, H. K. D. H. (1992) "*Bainite transformation kinetics Part 1 Modified model*", Mater. Sci. Technol., 8, 985-993.

Rouns T.N. and Rundman, K.B., (1987) "*Constitution of austempered ductile iron and kinetics of austempering*", AFS Trans., 95, 851-874.

Takahashi, M and Bhadeshia, H. K. D. H., (1991) "*A model for the microstructure of some advanced bainitic steels*", Materials Transactions, JIM, 32, 8, 689-696.

Thomson, R.C., James, J.S. and Putman, D.C., (2000) "*Modelling Microstructural Evolution and Mechanical Properties in Austempered Ductile Iron* ", Mater. Sci. Technol., 16, 1412-1419.

Tottle, C.R., (1984) "*An encyclopedia of metaliurgy and materials*", Macdonald and Evans Ltd., Estover, Plymouth PL6 7PZ, UK.

Trudel, A. and Gagne, M., (1997) "*Effect of composition and heat treatment parameters on the characteristics of austempered ductile iron*", Vol. 36, No. 5, 289-298.

Voigt, R.C. and Loper, C.R., (1984) "*Austempered ductile iron-process control and quality assurance*", J. Heat Treating, 3, 4, 291-309.

Voigt, R.C., Lee, Y.H and Tu, C.H., (1991) "*Use of hardenability data to determine alloy requirements for austempered ductile iron*", in Proceeding of the 1991 World ADI Conference, March 12-14, Chicago, IL, 479-515.

Yamakawa, S., Kobayashi, M., Numajiri, S. and Nakashima, K., (1997) "*Development of austempered ductile iron timing gears*", Truck and Bus Transmissions SAE special publications, 1309, 17-22.

Yan, M. and Zhu, W. Z., (1996) "*Morphology of bainitic platelets of austempered ductile iron and their effects on mechanical properties*", Journal of Materials Science Letters, Vol. 15, 1044-1047.

Yazdani, S. and Elliott, R., (1999) "*Influence of molybdenum on austempering behaviour of ductile iron Part 2- Influence of austenitising temperature on austempering kinetics, mechanical properties, and hardenability of ductile iron containing 0.13% Mo*", Mater. Sci. Technol., 15, 541-546.

References

Yescas, M.A., Bhadeshia, H.K.D.H. and MacKay, D.J. (2001) "*Estimation of the amount of retained austenite in austempered ductile irons using neural network*", Mater. Sci. Eng., A311, 162-17

Appendix I

Air flow data

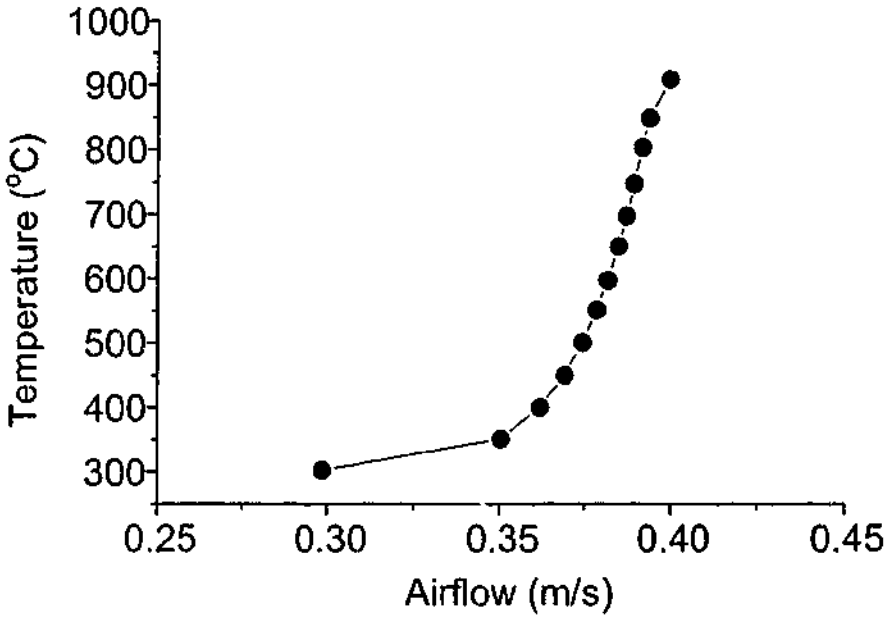

(a)

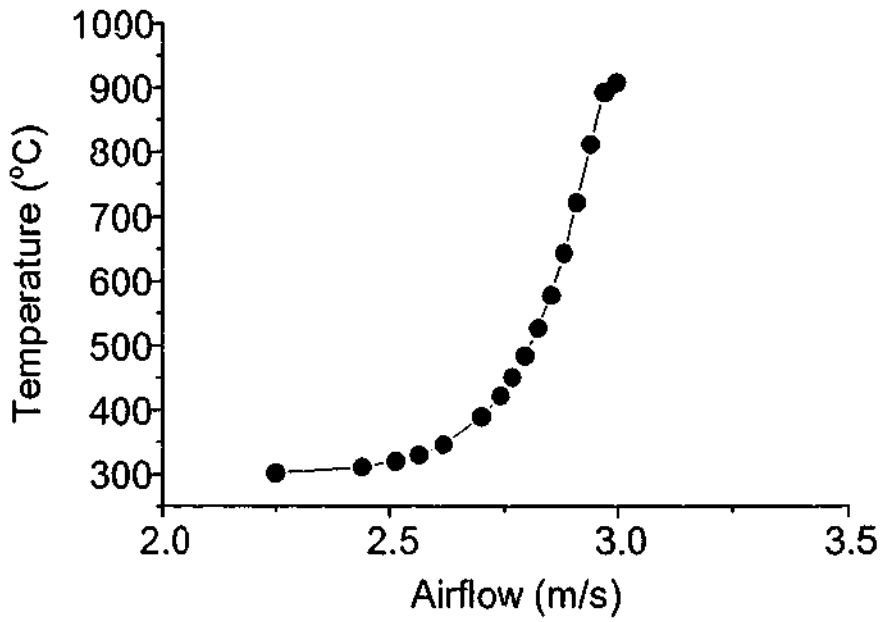

(b)

Figure I.1 Variation of the airflow with austempering temperature for (a) tensile and (b) impact specimens of test bar 2 at 300°C.

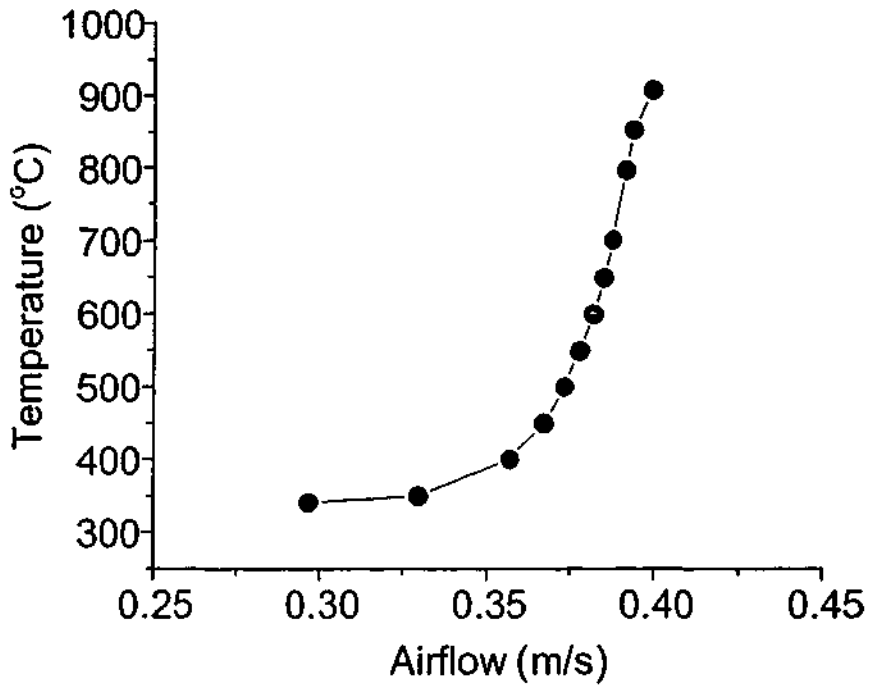

(a)

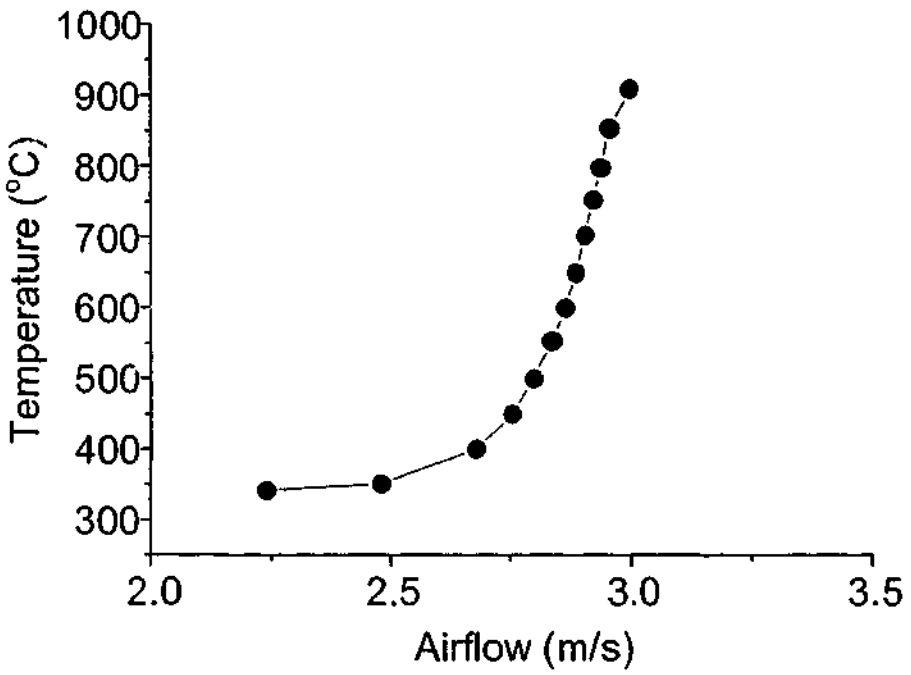

(b)

Figure I.2 Variation of the airflow with austempering temperature for (a) tensile and (b) impact specimens of test bar 2 at 340°C.

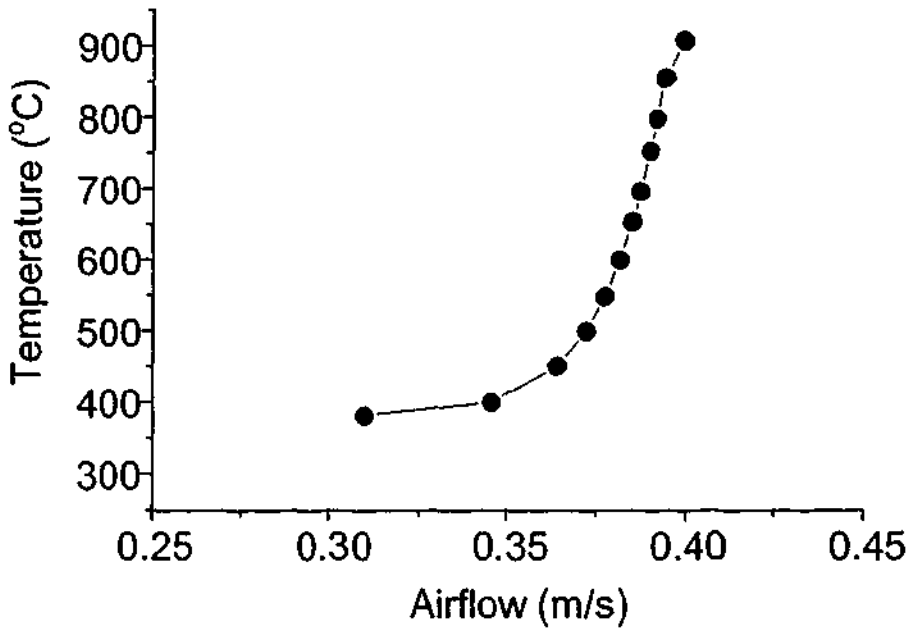

(a)

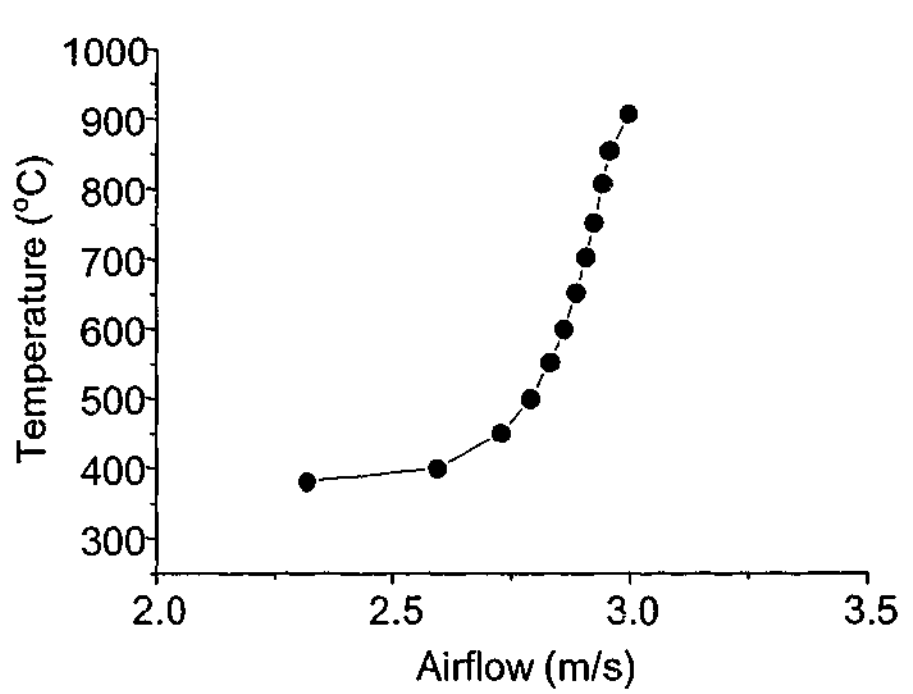

(b)

Figure I.3 Variation of the airflow with austempering temperature for (a) tensile and (b) impact specimens of test bar 2 at 380°C.

Appendix II

Data corresponding to test bar 2

Concentration of the alloying elements (wt%)

C=0.868	Si=2.46	Mn=0.36	Ni=0	Mo=0.18	Cr=0
V=0	Co=0	Cu=0.25	Al=0	W=0	

Mole fraction of the alloying elements

C=0.0382	Si=0.0464	Mn=0.0035	Ni=0	Mo=0.001	Cr=0
V=0	Co=0	Cu=0.0021	Al=0	W=0	

T_A (°C)	ΔG°_m	X_{TO}	θ	X_α	G_N
285	-2314	0.0653	0.7779	0.8049	-1504.29
290	-2283	0.0645	0.7761	0.7988	-1486.11
295	-2247	0.0637	0.7742	0.7926	-1467.93
300	-2212	0.0629	0.7722	0.7863	-1449.75
305	-2175	0.062	0.7701	0.7797	-1431.57
310	-2136	0.061	0.7678	0.7722	-1413.39
315	-2095	0.06	0.7654	0.7629	-1395.21
320	-2053	0.0589	0.7629	0.7525	-1377.03
325	-2007	0.0577	0.7601	0.7422	-1358.85
330	-1966	0.0565	0.7573	0.7308	-1340.67
335	-1936	0.0557	0.7549	0.7182	-1322.49
340	-1896	0.0549	0.7525	0.7041	-1304.31
345	-1862	0.0542	0.75	0.6893	-1286.13
350	-1830	0.0533	0.7475	0.6719	-1267.95
355	-1801	0.0527	0.7449	0.6499	-1249.77
360	-1762	0.0518	0.7422	0.6229	-1231.59
365	-1728	0.0511	0.7394	0.5908	-1213.41
370	-1698	0.0502	0.7366	0.5531	-1195.23
375	-1672	0.0496	0.7337	0.511	-1177.05
380	-1630	0.0487	0.7308	0.4678	-1158.87
385	-1596	0.0481	0.7278	0.4135	-1140.69
390	-1564	0.0472	0.7246	0.333	-1122.51
395	-1532	0.0466	0.7215	0.2412	-1104.33
400	-1502	0.0459	0.7182	0.1905	-1086.15

Thermodynamic data corresponding to test bar 2 for 285-400°C austempering temperatures, computed from Materials Algorithm Project Program Library (1999a, 1999b, 1999c) programs. Carbon concentration in the matrix is estimated from the Equation (4.2)

Appendix III

Computer program

A computer disk is attached to this thesis that executes the program for estimation of the processing-austemperability window. In this section the details are provided to run the program (PAW.EXE) in DOS environment.

The following steps are to be followed for execution of the PAW.EXE program:

In the windows main menu select Start, Program and MS-DOS Prompt
Type A:
Type PAW + Enter key on the keyboard (the program executes)
Type the austenitising temperature in °C + Enter key
Type the alloy content of the ductile iron according to chemical analysis for Si, Mn, Mo, Cu and Ni respectively. Click the Enter key after entering each number.

The results will appear on the screen. The program writes the results on a data file called PAW.DAT on the floppy disk provided. The data file can be opened using Microsoft Excel or any other program that reads a text file such as Note Pad.

The program PAW.EXE is only for review of this thesis. Reproduction and copy of the program is strongly prohibited due to intellectual property agreements with Monash University and Metal Treatment Services Ltd. The outcome of the PAW.EXE program for test bar 2 of this study is shown in the

following table (data were extracted from the data file PAW.DAT which was created automatically during the execution of the program).

********INPUTS*******

Austenitising Temperature (°C):905.0

Si= 2.460 Mn= .360 Mo= .180 Cu= .250 Ni= .000

*******RESULTS******

Carbon concentration in the matrix (%): 0.86787

Xbar (min:0.0381-max:0.0389): 0.03820

Temp.(°C)	T1(s)	T2(s)	R_{cmax}(mm)
285.00	1838.	21981.	25.
290.00	1585.	24868.	25.
295.00	1474.	27822.	24.
300.00	1327.	30532.	24.
305.00	1271.	32997.	24.
310.00	1292.	35087.	24.
315.00	1386.	36701.	24.
320.00	1555.	37778.	24.
325.00	1815.	38303.	24.
330.00	2172.	38285.	24.
335.00	2637.	37773.	24.
340.00	3277.	36901.	24.
345.00	4089.	35754.	23.
350.00	5104.	34464.	23.
355.00	6325.	33141.	23.
360.00	7814.	31954.	23.
365.00	9439.	30868.	23.
370.00	11087.	29854.	23.
375.00	12700.	28924.	23.
380.00	13957.	27809.	23.
385.00	14693.	26379.	22.
390.00	14692.	24439.	22.
395.00	13879.	21920.	22.
400.00	12280.	18845.	22.

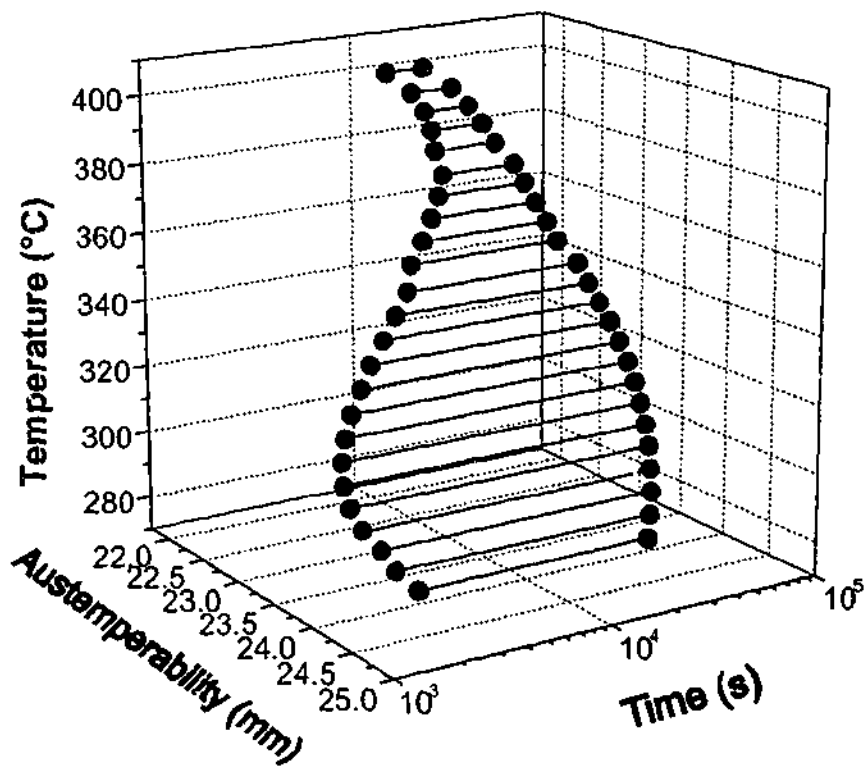

Figure III.1 A three-dimensional presentation of the predicted data corresponding to test bar 2 (processing-austemperability window for test bar 2).

Appendix IV

List of publications

S.H. Zahiri, E.V. Pereloma and C.H.J. Davies, (2002) "*A model for prediction of the processing window for austempered ductile iron*", Mater. Sci. Technol. (Accepted).

S.H. Zahiri, E.V. Pereloma and C.H.J. Davies, (2001) "*Application of a bainite transformation model to the estimation of processing window boundaries for a Mn-Mo-Cu austempered ductile iron*", Mater. Sci. Technol., 17, 1563-1568.

S.H. Zahiri, E.V. Pereloma and C.H.J. Davies, (2001) "*Examination of a model for prediction of the processing window for a Mn, Cu and Mo austempered ductile iron*", In proceedings: Engineering Materials 2001 conference, Melbourne, Australia, 171-176.

S.H. Zahiri, E.V. Pereloma and C.H.J. Davies, (2001) "*Examination of a model for prediction of the processing window and austemperability for austempered ductile iron*", In proceedings: Australian Ductile Iron Producers Association, 33 year anniversary publication, Perth, Australia, 5-15.

S.H. Zahiri, E.V. Pereloma and C.H.J. Davies, (2000) "*Application of a bainitic model for prediction of the processing window for austempered ductile iron*", in proceedings: The 20th ASM Heat Treating Society Conference, Missouri, USA, 121-128.

S.H. Zahiri, E.V. Pereloma and C.H.J. Davies, (1999) "*Evolution of microstructure and mechanical properties in a heavy section size Mn-Mo-Cu austempered ductile iron*", In proceedings: Materials Research Forum, 1999 Materials Processing, Monash University, Australia, 41-46.